R-09-23

Groundwater flow modelling of the excavation and operational phases – Laxemar

Urban Svensson, Computer-aided Fluid Engineering AB

Ingvar Rhén, SWECO Environment AB

December 2010

Svensk Kärnbränslehantering AB
Swedish Nuclear Fuel
and Waste Management Co

Box 250, SE-101 24 Stockholm
Phone +46 8 459 84 00

ISSN 1402-3091
SKB R-09-23

Groundwater flow modelling of the excavation and operational phases – Laxemar

Urban Svensson, Computer-aided Fluid Engineering AB

Ingvar Rhén, SWECO Environment AB

December 2010

Keywords: SKBdoc 1267486, Hydrogeology, Groundwater, Modelling, Excavation, Operation, Grouting, Laxemar.

Abstract

As a part of the license application for a final repository for spent nuclear fuel at Forsmark, the Swedish Nuclear Fuel and Waste Management Company (SKB) has undertaken a series of groundwater flow modelling studies. These represent time periods with different hydraulic conditions and the simulations carried out contribute to the overall evaluation of the repository design and long-term radiological safety. The modelling study reported here presents calculated inflow rates, drawdown of the groundwater table and upconing of deep saline water for different levels of grouting efficiency during the excavation and operational phases of a final repository at Laxemar. The inflow calculations were accompanied by a sensitivity study, which among other matters handled the impact of different deposition hole rejection criteria. The report also presents tentative modelling results for the duration of the saturation phase, which starts once the used parts of the repository are being backfilled.

Sammanfattning

I Svensk Kärnbränslehanterings (SKB) ansökan om ett slutförvar för använt kärnbränsle i Forsmark ingår olika grundvattenmodelleringsstudier. Studierna hanterar perioder med olika hydrauliska förhållanden och beräkningsresultaten från simuleringarna bidrar till bedömningsunderlaget inom design och långsiktig säkerhet. Föreliggande rapport presenterar resultaten från en modellering av bygg- och driftskedena av ett slutförvar i Laxemar. Rapporten redovisar beräknade inflöden till olika anläggningsdelar, beräknad avsänkning och beräknad uppträngning av salthaltigt, djupt grundvatten. Beräkningarna har utförts för olika täthetsnivåer av injektering. Inflödesberäkningarna har kompletterats med en känslighetsstudie i syfte att studera inverkan av olika typer av osäkerheter och antaganden, till exempel betydelsen av olika kriterier för diskriminering av kapselhål. Rapporten redovisar även en preliminär beräkning av varaktigheten av mättnadsskedet som påbörjas i och med att deponeringstunnlarna fylls igen.

Contents

1 Introduction

1.1 Background

The Swedish Nuclear Fuel and Waste Management Company (SKB) has conducted site investigations at two different locations, the Forsmark and Laxemar-Simpevarp areas (Figure 1-1), with the objective of siting a final repository for spent nuclear fuel according to the KBS-3 concept. As a part of the application for a final repository for spent nuclear fuel at Forsmark, information from a series of groundwater flow modelling studies is evaluated to serve as a basis for an assessment of the repository design and long-term radiological safety premises. The present report is one of a series of three groundwater flow modelling studies, which together handle different periods of the entire lifetime of a final repository at Laxemar.

- Groundwater flow modelling of the excavation and operational phases – Laxemar (this report).
- Groundwater flow modelling of periods with temperate climate conditions – Laxemar /Joyce et al. 2010/.
- Groundwater flow modelling of periods with periglacial and glacial climate conditions – Laxemar /Vidstrand et al. 2010/.

A corresponding series of studies exists for the investigated area at Forsmark. The results presented in the work reported here support the site-selection, which also is reported as part of the application for Forsmark.

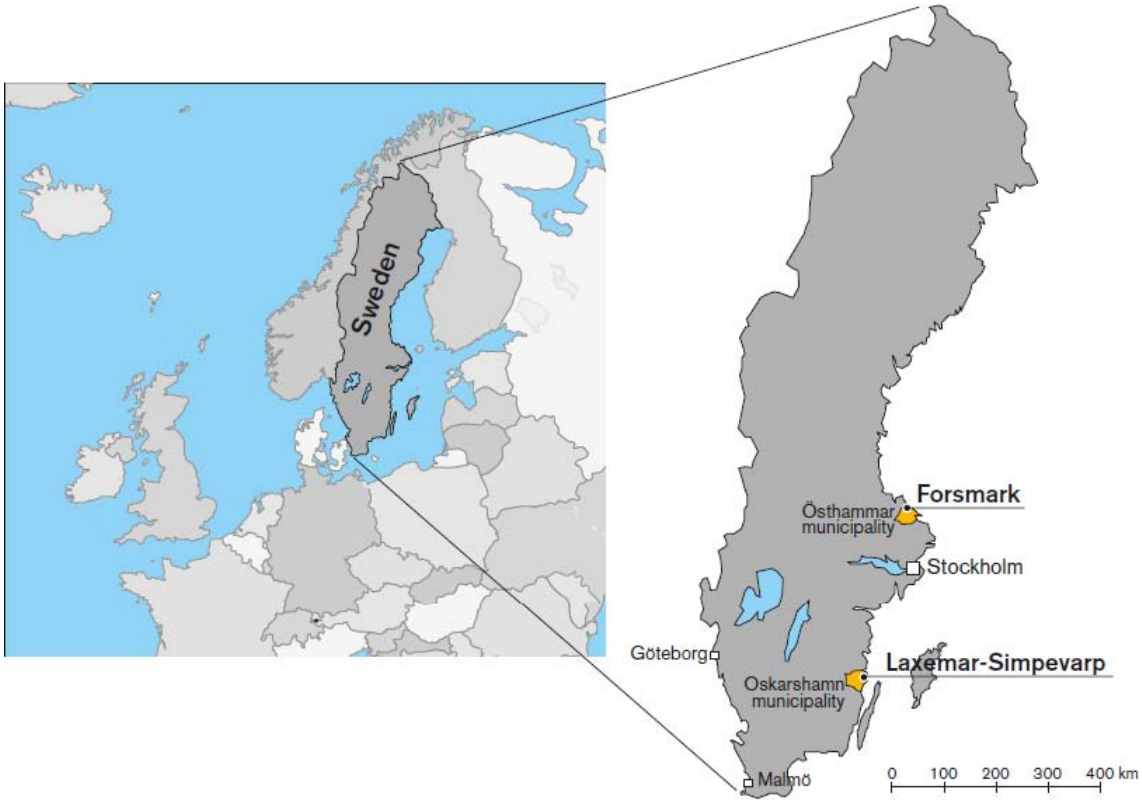

Figure 1-1. *Map of Sweden showing the location of the Forsmark and Laxemar-Simpevarp sites, located in the municipalities of Östhammar and Oskarshamn, respectively. (Source: Figure 1-1 in /SKB 2008/.)*

1.2 Scope and objectives

The main objective of the modelling work reported here is to inform about the hydrogeological effects caused by an open final repository for spent nuclear fuel at Laxemar. In particular, the work has studied:

- the magnitude and spatial distribution of the inflow to the open repository,
- the magnitude and spatial distribution of the drawdown of the groundwater table,
- the chemical composition, i.e. salinity, and spatial distribution of the groundwater in proximity of the open repository,
- the role of grouting for the inflow, drawdown and upconing phenomena, and
- the saturation period after the open repository has been closed (backfilled).

The mathematical modelling reported here considers five operation stages, A–E, which were run in sequence, where the first stage, stage A, lasted for 5 years, stage B lasted for 15 years, stage C lasted for 10 years, stage D lasted for 10 years and stage E lasted for 15 years. Hence, the total operation time was 55 years. The role of grouting was looked at by modelling six levels of grouting efficiency (to be defined below), I–VI. Finally, some sensitivity tests were run and, among other things, the effect of different criteria for the rejection of deposition holes was evaluated.

The modelling work used version 3.3 of the DarcyTools computational code. It is noted that the current documentation of DarcyTools concerns version 3.4 /Svensson et al. 2010/, but that the differences are insignificant for the applications reported here. Both versions allow the user to apply an unstructured computational grid. An unstructured grid is necessary in order to resolve the complex geometry of a final repository, which consists of a ramp, a few shafts, transportation and main tunnels, and many deposition tunnels and about eight thousand (8,031) deposition holes, see Figure 1-2. The studied repository is located at about –505 m elevation. The repository layout is adapted to the deterministically modelled deformation zones /SKB 2009a/.

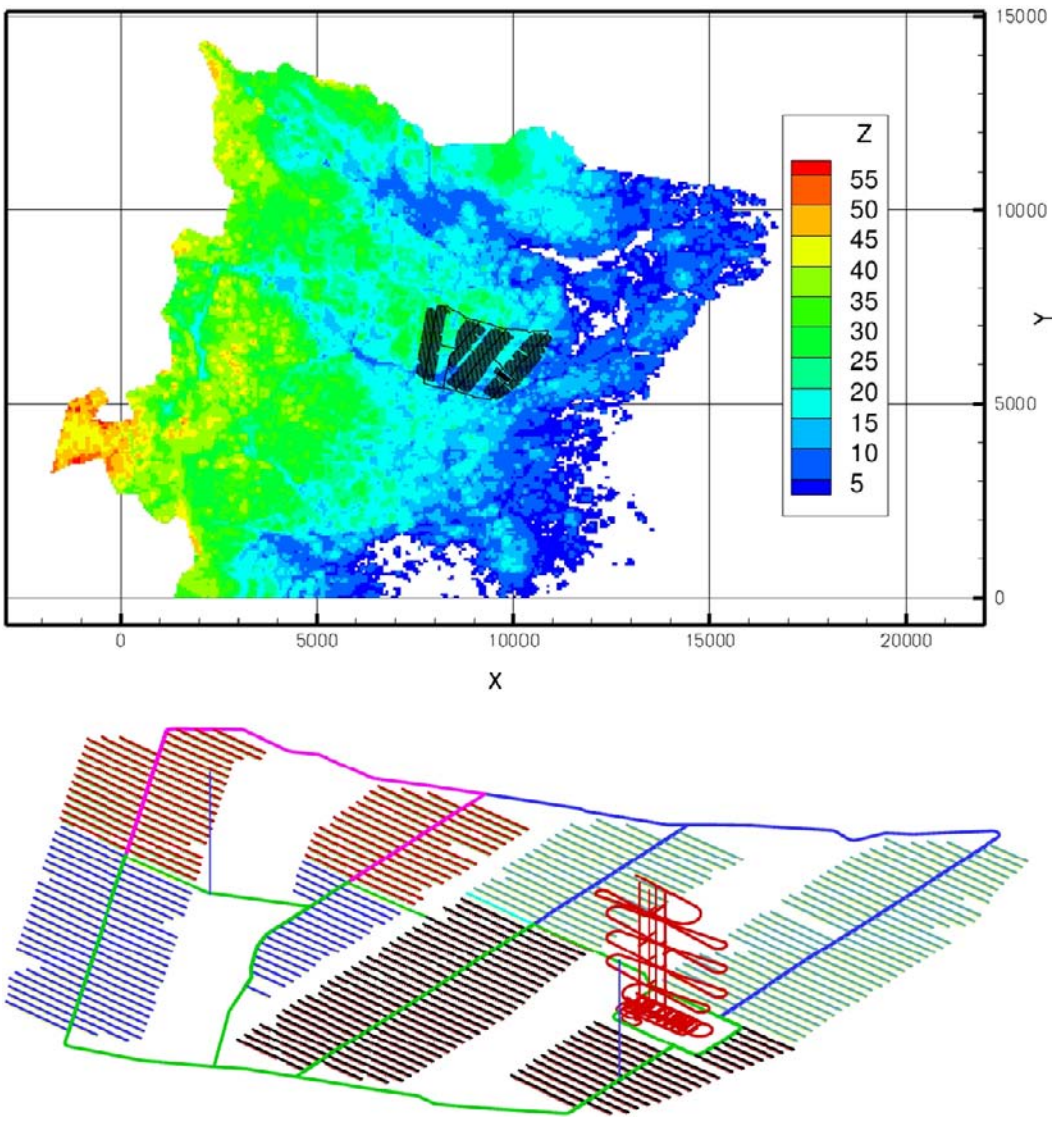

Figure 1-2. *Layout of the repository. Horizontal plane of layout (top). Definition of different parts of the repository (bottom). Colours in the bottom figure indicate different stages in the development of the repository. However, some Main & Transport tunnels are common for different stages and the five stages (A–E) are for this reason shown one by one below.*

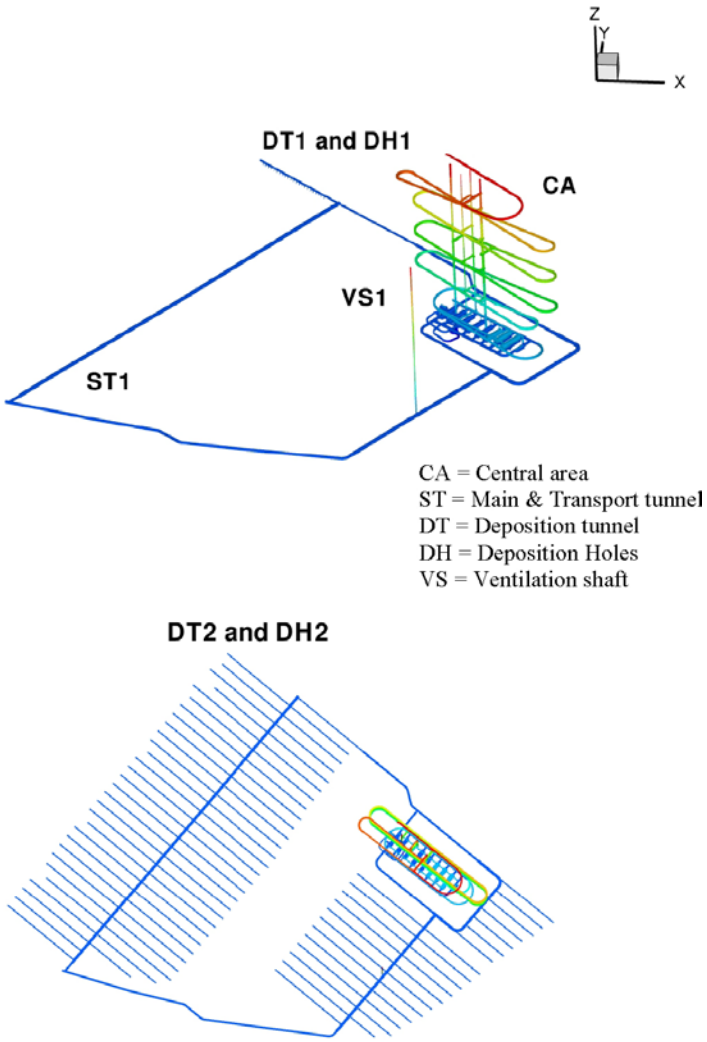

Figure 1-2, continued. *Stages A (top) and B. In this and next figure the central area is coloured with elevation, for clarity.*

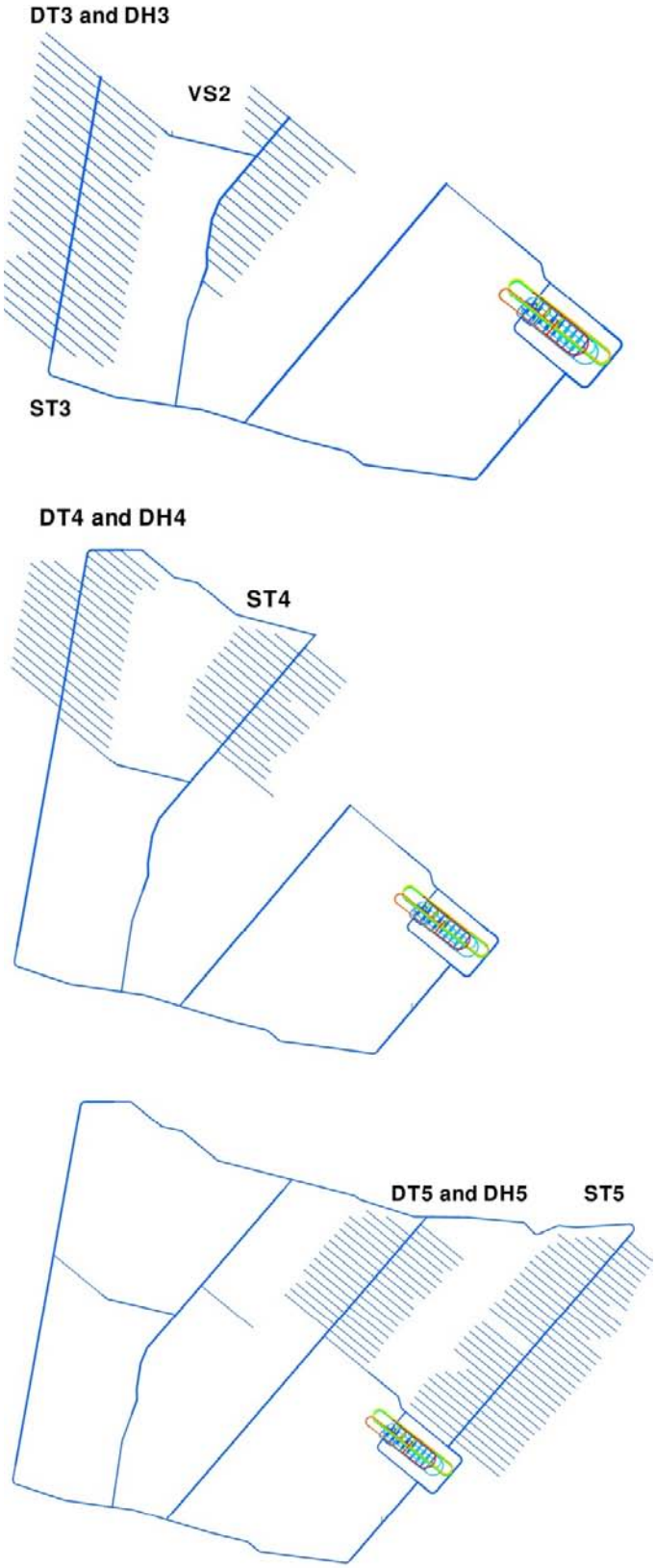

Figure 1-2, continued. *Stages C (top), D (middle) and E (bottom).*

1.3 Limitations

The transport of heat and the transport of radio nuclides from the repository to the ground level were not studied in the work reported here. In addition, all simulations were carried out at quasi steady-state flow conditions implying that storativity effects were considered unimportant for the physics involved during the excavation and operational phases of a final repository in fractured crystalline rock. (The term "quasi steady-state" only implies that the storativity effects were considered unimportant; the actual simulations were carried out as a transient process. The importance of the storativity was evaluated by sensitivity studies.)

1.4 Setting

The Laxemar-Simpevarp area is located on the Swedish east coast near Oskarshamn and c. 350 km south of Stockholm.

The Laxemar-Simpevarp regional model area is dominated by a geological unit referred to as the Transscandinavian Igneous Belt (TIB). The bedrock is dominated by well preserved c. 1.8 Ga intrusive rocks varying in composition between granite-syenitoid-dioritoid-gabbroid. Although a non-uniformly distributed faint to weak foliation, is present, the most prominent ductile structures at Laxemar are discrete, low-temperature, brittle-ductile to ductile shear zones of mesoscopic to regional character, which are related to the waning stages of the Svecokarelian Orogeny. Subsequently, the rock mass has been subjected to repeated phases of brittle deformation, under varying regional stress regimes, involving reactivation along earlier formed structures. There are indications that the ductile anisotropy, including both larger ductile shear zones as well as the weak to faint foliation, minor shear zones and mylonites, has had an influence on the later brittle deformation. With a few exceptions, the deterministically modelled deformation zones at Laxemar are characterised by brittle deformation although virtually all the zones have their origin in an earlier ductile regime. The brittle history of the Laxemar-Simpevarp area is complex and involves a series of reactivation events that do not allow the construction of a consistent model covering their development /Wahlgren et al. 2008/. /Söderbäck 2008/ provides a detailed description of the geological evolution of the Fennoscandian Shield in south-eastern Sweden from c. 1.91 Ga and to the Quaternary period.

The investigated area is close to the coast, cf. Figure 1-3. The topography is fairly flat (regional topographic gradient in the order of 4%; the topography corresponds to the Sub-Cambrian Peneplain /Fredén 2002/) but with relatively distinct valleys, cf. Figure 1-4 and Figure 1-5. The investigation area is located within a crystalline basement, mostly covered by a rather thin till in the elevated areas and with glaciofluvial sediments in the larger valleys. The site-average annual precipitation and specific discharge are estimated to be on the order of 600 mm and 160–170 mm, respectively /Werner et al. 2008, Larsson-McCann et al. 2002/ and the area is covered with a fairly large number of small streams indicating small local drainage basins within the regional model area, cf. Figure 1-3. The Äspö Hard Rock laboratory is an underground research facility that is located below the Äspö Island, cf. Figure 1-3, and the facility affects the groundwater flow locally in the area. The Simpevarp peninsula hosts the Clab interim facility and the nuclear power plants O1, O2 and O3. At Clab inflows are observed to the rock caverns near the surface and the shallow shafts surrounding the foundations of the power plants, but it has a very local effect on the groundwater flow. The hydrogeology of the area is described in more detail in /Rhén and Hartley 2009/.

The regional and local model areas employed for model version SDM-Site Laxemar are shown in Figure 1-6. The *Laxemar-Simpevarp regional (scale) model area/volume* (Later in the report referenced as *Regional model area/volume*) for SDM-Site Laxemar is the same as the one used in model version Laxemar 1.2. *Laxemar local (scale) model area/volume* (Later in the report referenced as *Local model area/volume*) for model version SDM-Site Laxemar and *Focused area/volume* for the *complete site investigations* is the central, southern and western parts of the local model area, cf. Figure 1-6.

Here the model area shown with a thick blue line is used (in legend denoted "Connect Flow regional model area").

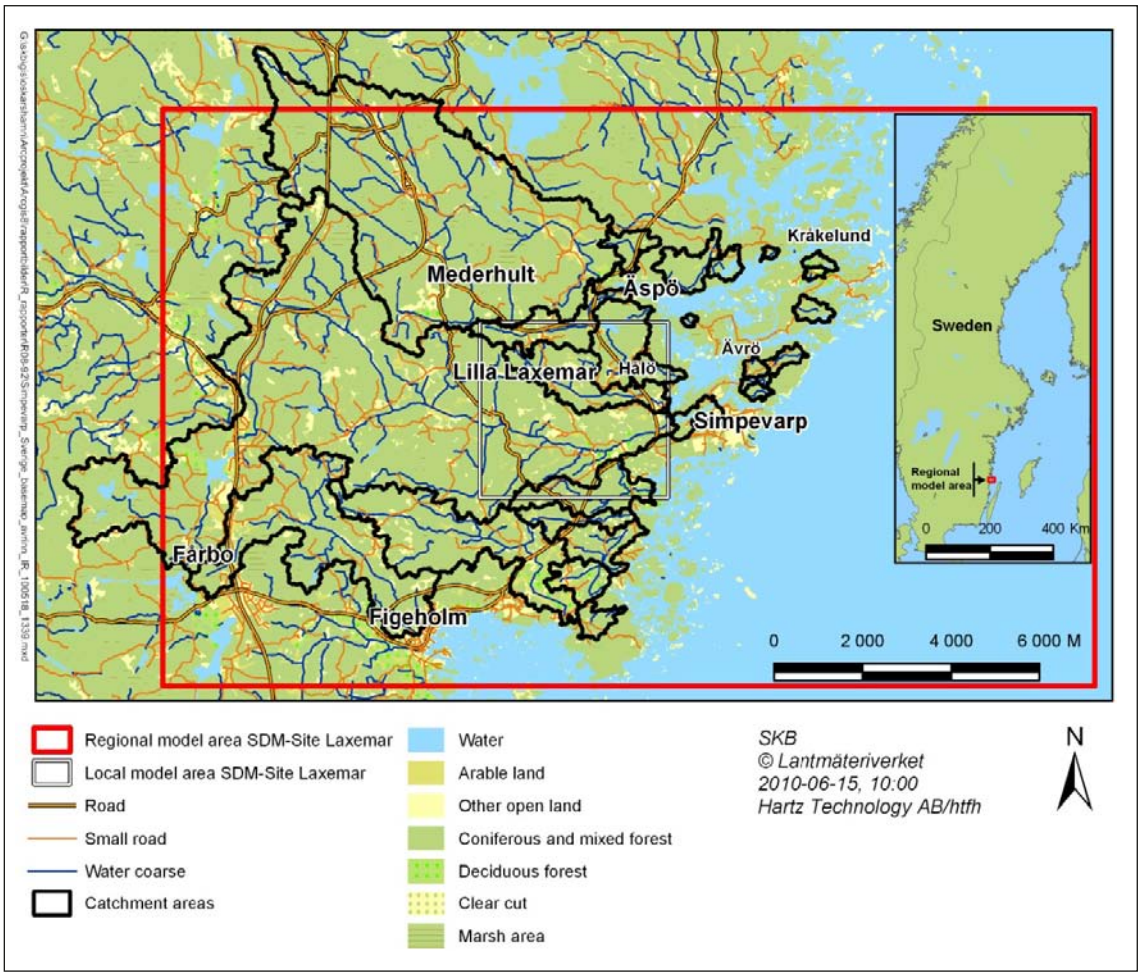

Figure 1-3. *Overview map of the Laxemar-Simpevarp regional model area with the SDM-Site Laxemar local model area indicated. The large number of small streams indicates small local drainage basins within the regional model area. /Rhén and Hartley 2009/.*

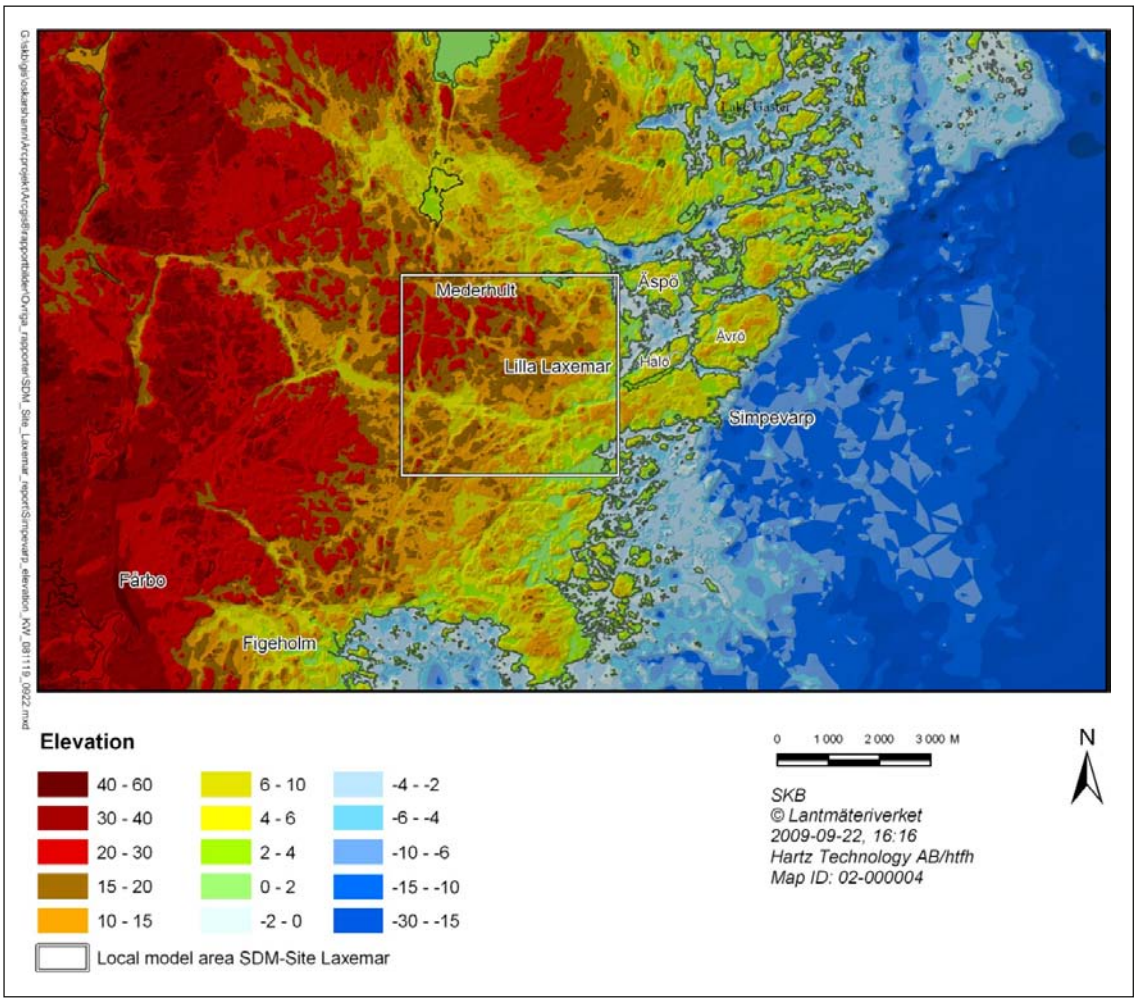

Figure 1-4. *Overview map illustrating the elevation of the ground-surface topography (m.a.s.l.) in an area corresponding to the Laxemar-Simpevarp regional model area, including the bathymetry of lakes and the sea. /Rhén and Hartley 2009/.*

Figure 1-5. *Air photographs showing the flat topography, low gradient near shore situation in the Laxemar-Simpevarp area with shallow bays, a) view from the southeast, Clab facility in the foreground, b) view from the west, drill site KLX05/KLX12A in the centre of the photograph. Both photographs show the outline of the focused area in Laxemar in red, cf. Figure 1-6. /Rhén and Hartley 2009/.*

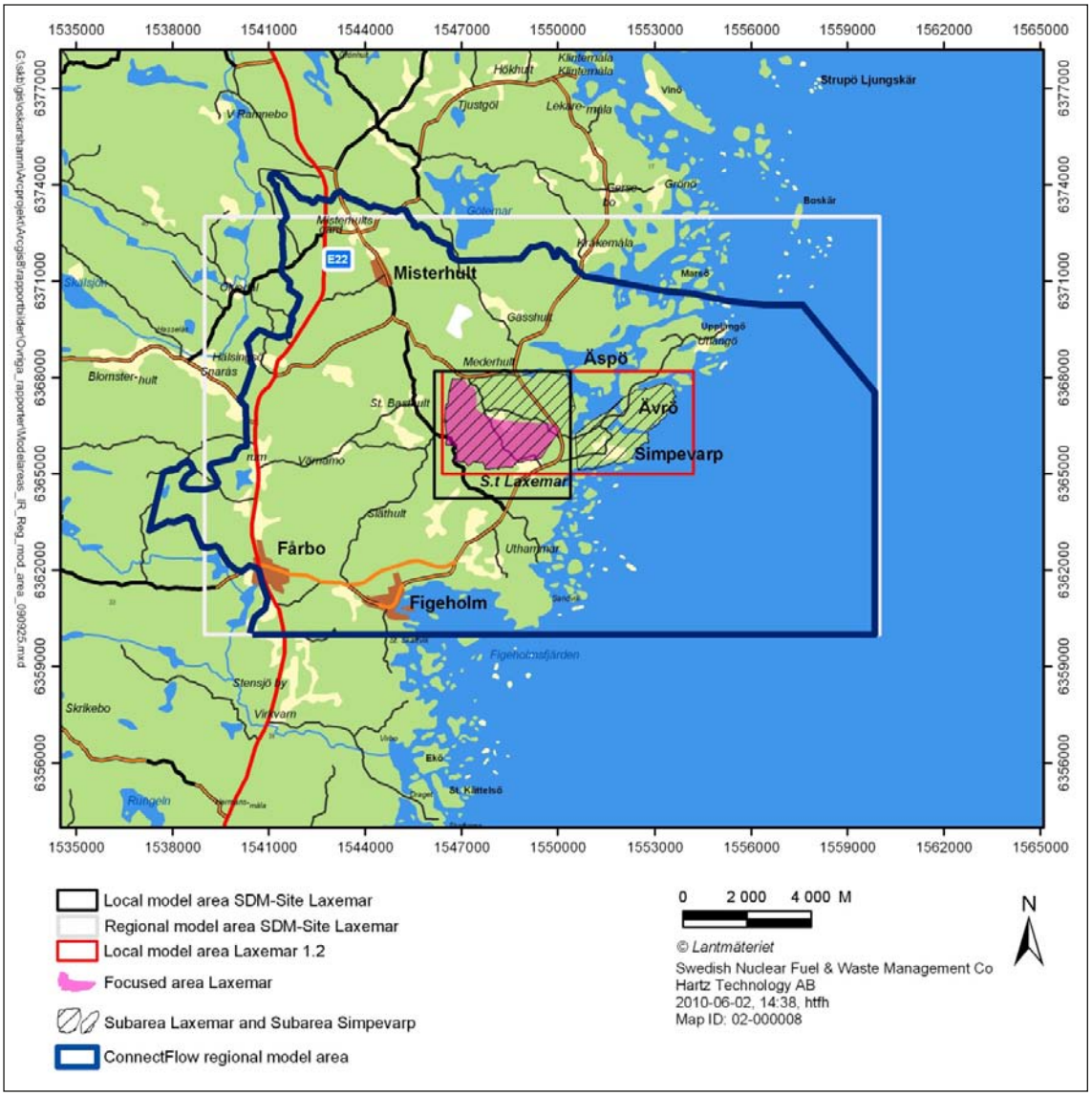

Figure 1-6. *Regional and local model areas used for model version SDM-Site Laxemar. The area coverage of the regional model is the same as that employed in previous model versions, whereas the local model area is significantly reduced compared to that employed in model version Laxemar 1.2. Laxemar subarea and Simpevarp subarea defined the investigation areas during the initial stage of the site investigations. The choice of boundaries used for the SDM-Site regional groundwater flow simulations (Using ConnectFlow) based on surface water catchments is also shown. /Rhén and Hartley 2009/.*

1.5 This report

In order to better understand the bedrock hydrogeology at the Laxemar site, we briefly present in Chapter 2 the hydrogeological model of the Laxemar site as reported within SDM-Site /Rhén et al. 2009/. Chapter 3 presents the primary concepts and methodology of the DarcyTools computational code used in the groundwater flow modelling reported here.

The conditions that are specific to the flow modelling of the excavation and operational phases of a final repository at Laxemar are summarised in Chapter 4. Chapter 4 also presents the model variants handled as a means to address various uncertainties. Chapter 5 presents the results of the flow simulations, and Chapter 6 contains a summary of the work carried out and the conclusions drawn.

1.5.1 Terminology

As explained in the work by /Joyce et al. 2010/, two hydrogeological discrete fracture network (Hydro-DFN) models are defined at Laxemar; the Hydrogeological base case and the Elaborated Hydro-DFN.

- The first model, the Hydrogeological base case, builds upon the Hydro-DFN model derived within SDM-Site /Rhén and Hartley 2009/. Besides providing a general description of the bedrock hydrogeology at Laxemar, Chapter 2 also presents the model parameters of the Hydrogeological base case.
- The second model, the Elaborated Hydro-DFN, is a refinement of the Hydrogeological base case derived within SR-Site. The model parameters of the Elaborated Hydro-DFN are specified in /Joyce et al. 2010/.

The reason for the Elaborated Hydro-DFN can be summarised as follows. During SDM-Site, the flow modelling of the paleohydrogeological evolution at the Laxemar site showed that the derived Hydro-DFN for SDM-Site (i.e. the Hydrogeological base case) is slightly too transmissive. Reducing the permeabilities below –150 m by a factor of three improved the match to measured values. This calibration resulted in the Elaborated Hydro-DFN, see /Joyce et al. 2010/ for details.

Both models, the Hydrogeological base case and the Elaborated Hydro-DFN, are studied by /Joyce et al. 2010/ and /Vidstrand et al. 2010/ as well as in the work reported here. Following the terminology used in /Joyce et al. 2010/, the Hydrogeological base case should be called Base case in the work reported here since it refers to the Hydrogeological base case studied by /Joyce et al. 2010/. Consequently, the Elaborated Hydro-DFN should be regarded as a model variant.

However, it is important to note that the Elaborated Hydro-DFN is used for the main part of the work reported as it is the model referenced in the site selection /SKB 2010/. In conclusion, the model setup and conditions described in Chapter 4 refer to the Elaborated Hydro-DFN and the model variants discussed in Chapter 4 are variants to the Elaborated Hydro-DFN. The Hydrogeological base case model is only used for the sake of comparison of the two models (Appendix E).

The report contains six Appendices A–F with the objective to describe and document some key assumptions of the implementations in DarcyTools, or for the sake of traceability, consistency and quality assurance.

- The position of the groundwater table was modelled with a free surface algorithm that can handle both natural conditions and the drawdown due to the inflow to an open repository. The algorithm is described in Appendix A.
- The impact of grouting on the calculated inflow rates, drawdown of the groundwater table and upconing of deep saline water was studied by altering the hydraulic conductivity of the computational grid cells in contact with the modelled repository. Appendix B describes how the grouting routine was applied.
- Appendix C is an excerpt of /Svensson 2010/. It briefly presents the hydration process and the approximate method used here to estimate the time scale of the saturation of the backfilling material.
- Scoping calculations of inflow to an open repository are given in Appendix D.
- Appendix E presents results from simulations conducted based on the Hydrogeological base case model. Comparisons are made with the Elaborated Hydro-DFN model.
- For the sake of traceability, consistency and overall quality assurance, Appendix F lists all files with input data, which were imported and used to parameterise the flow models reported here.

2 Hydrogeological model of the Laxemar site

2.1 Supporting documents

The SDM-Site Laxemar hydrogeological reporting in /Rhén and Hartley 2009/ provides a detailed summary of the work described in /Rhén et al. 2008/ and in /Rhén et al. 2009/, i.e. the field investigations, the data analyses, the conceptual model development and the numerical modelling of groundwater flow and solute transport. The complete SDM-Site Laxemar site-descriptive modelling work is reported in /SKB 2009a/ and the overall confidence assessment associated with the modelling work is detailed in /SKB 2009b/.

Table 2-1 shows the cumulative number of boreholes providing hydraulic information about the bedrock in the Laxemar-Simpevarp area. The number of boreholes is shown in relation to the two investigation stages; Initial Site Investigations and Complete Site Investigations (ISI and CSI), the five model versions (Version 0, Simpevarp 1.1, Simpevarp 1.2 and Laxemar 1.2, and model version SDM-Site Laxemar) carried out during the period 2002–2008. Model version Laxemar 1.2 represents the culmination of the ISI. The current hydrogeological modelling based on data freeze Laxemar 2.3 constitutes the principal contribution to SDM-Site Laxemar, corresponding to the CSI from a hydrogeological point of view. Investigations in c. 4,000 m of deep cored boreholes (KLX01-04) provided old and new (from the ISI) hydraulic data within the Laxemar local model area for model version Laxemar 1.2. After Laxemar Stage 2.3 (CSI) hydraulic data from 16 additional deep cored boreholes within the Laxemar local model area with an approximate total length of 12,800 m were available (KLX05, KLX06, KLX07A, KLX08, KLX09, KLX10, KLX11A, KLX12A, KLX13A, KLX15A, KLX16A, KLX17A, KLX18A, KLX19A, KLX20A, KLX21B).

Table 2-1 also shows references to the major background reports in relation to each model version/stage /Follin et al. 2004, 2005, 2006, Hartley et al. 2004, 2005, 2006, 2007, Holmén 2008, Rhén et al. 1997, 2006a, b, c, 2008, 2009, SKB 2002, 2004, 2005, 2006a, b/.

Table 2-1. The cumulative new (drilled during site investigation) number of boreholes providing hydraulic information about the bedrock in the Laxemar-Simpevarp area at the end of the five model versions carried out during the period 2002 through 2008. Kxx = core-drilled boreholes, Hxx = percussion-drilled boreholes (KLX and HLX: core-drilled boreholes or percussion-drilled boreholes within the Laxemar local model area). The reports listed in italics describe the hydraulic data collected and/or the hydrogeological modelling undertaken. The reports with underlined reference numbers summarise the development of the hydrogeological modelling along with the developments achieved within the other disciplines. /Rhén and Hartley 2009/.

	Initial site investigation (ISI)			Complete site investigation (CSI)	
Desk top exercise	**Training exercise**	**Preliminary SDM**	**Preliminary SDM**	**Feedback and strategy**	**Model verification and uncertainty assessment**
Version 0	**Version 1.1**	**Simpevarp Version 1.2**	**Laxemar Version 1.2**	**Laxemar Stage 2.1**	**Laxemar Stage 2.3 (Version SDM-Site)**
0 Kxx	0 Kxx [1)]	4 Kxx [2)]	9 Kxx [3)]	11 KLX (25%) [4)]	44 KLX (100%) [5)]
0 Hxx	0 Hxx	3 Hxx	14 Hxx	9 HLX (26%) [4)]	34 HLX (100%)
			3 KLX (7%) [3)]		
			9 HLX(26%)		
R-02-35	R-04-25	R-05-08	R-06-10	R-06-110	TR-09-01
TR-97-06	*TR-97-06*	*R-06-20*	*R-06-21*	*R-07-57*	*R-08-78*
	R-04-63	*R-05-11*	*R-06-22*	*R-08-60*	*R-08-91*
	R-04-65	*R-05-12*	*R-06-23*		*R-08-92*
			R-06-24		

[1)] Some old data from KLX01 and KLX02 were used besides earlier interpretations from the area.

[2)] Old data from KLX01, KLX02, KAV01, KAV02 and KAV03 also used besides the indicated three KSH holes and KAV01 with some new data.

[3)] KLX02–04. KLX02 included as some new tests were performed in that borehole. A few data from KLX05 and KLX06 were also available but these boreholes are not included here as the large amount of data became available later. Kxx also includes three KSH holes, KAV01, KAV04A, and KAV04B. Old data from KLX01 also used but not included in the numbers in the table.

[4)] KLX02–12 included but data not complete for all these boreholes at this stage. Old data from KLX01 also used. New HLX boreholes were not considered.

[5)] 19 core holes longer than 300 m and 25 shorter than 300 m. KLX01 and KLX27A not included.

2.2 Systems approach in SDM-Site

In order to meet the objectives for model version SDM-Site Laxemar /Rhén and Hartley 2009/ (SDM: Site Descriptive Model), the groundwater system is divided into different hydraulic domains. Figure 2-1 illustrates schematically SKB's systems approach as employed in the hydrogeological SDM (Site Descriptive Model) for Laxemar. The groundwater system consists of three basic hydraulic domain types, namely HSD, HCD and HRD, where:

- HSD (Hydraulic Soil Domain) represents the Quaternary deposits,
- HCD (Hydraulic Conductor Domain) represents deformation zones,
- HRD (Hydraulic Rock mass Domain) represents the fractured bedrock between the deformation zones.

The systems approach constitutes the basis for the conceptual modelling, the site investigations and the numerical simulations carried out in support of the hydrogeological SDM /Rhén et al. 2003/.

Besides the three hydraulic domains shown in Figure 2-1, the groundwater flow (saturated flow) and solute transport modelling consists of three additional elements:

- A solute (salt) transport model for the modelling of advective transport and matrix diffusion.
- Initial conditions for groundwater flow and hydrochemistry.
- Boundary conditions for groundwater flow and hydrochemistry.

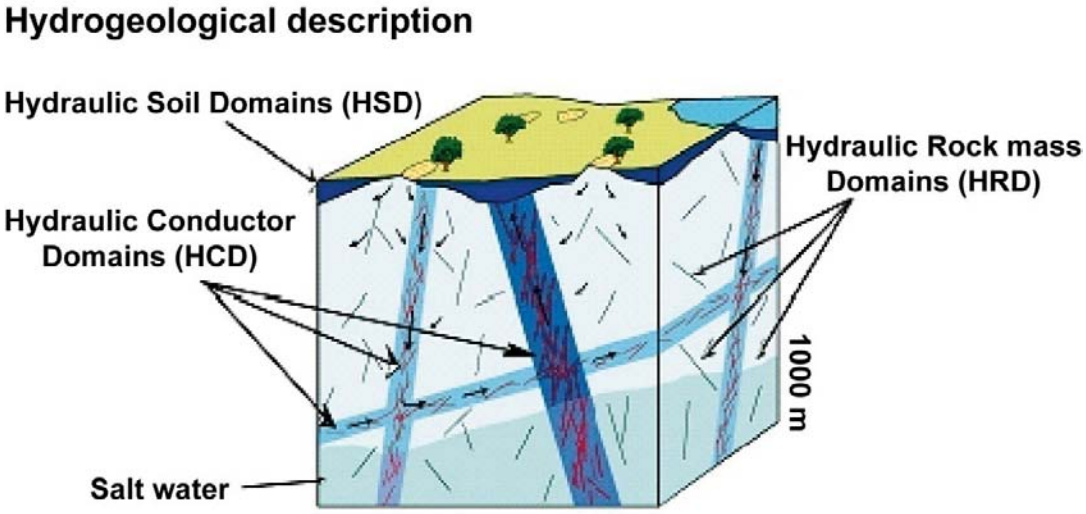

Figure 2-1. *Cartoon showing the division of the crystalline bedrock and the overburden (Quaternary deposits) into hydraulic domains. Within each domain, the hydraulic properties are represented by equivalent values, or by spatially distributed statistical distributions /Rhén et al. 2003/.*

2.3 Summary of the bedrock hydrogeological model

2.3.1 General

Single-hole hydraulic tests, interference tests, groundwater levels and hydrochemical data are the basis for the hydrogeological characterisation, together with the geological model. Investigations have essentially been made down to c. 1,000 m depth but there is also one borehole (KLX02) that has provided data down to c. 1,600 m depth. The PFL-f (f stands for fracture or feature, PFL is abbreviation for *Posiva Flow Log*) method is essential for the hydrogeological model. The PFL-f method constitutes a geophysical logging device developed to detect continuously flowing features in sparsely fractured crystalline bedrock by means of difference flow logging, using a 1 m test section that is moved stepwise 0.1 m. The PFL method essentially provides an estimate of the specific capacity (Q/s) [L^2T^{-1}], where s represents the drawdown and Q the flow rate. Transient injection tests with PSS (*Pipe String System*) have been performed using 3 different test scales: 5, 20 and 100 m with 5 m tests only being performed in the elevation interval –300 m to –700 m, covering the foreseen repository depth, cf. /Rhén and Hartley 2009/ for details.

The Laxemar-Simpevarp regional model area is in general characterised by an undulating bedrock surface with a thin cover of Quaternary deposits, mainly till on the top of the hills and thicker Quaternary deposits in the valleys made up of till overlain by postglacial deposits. The crystalline bedrock is intersected by a number of deformation zones, denoted Hydraulic Conductor Domains (HCD) in the hydrogeological model, which are mainly steeply dipping, with less fractured bedrock between these zones. The bedrock in between the HCDs is in the hydrogeological model called Hydraulic Rock mass Domains (HRD). Hydraulically, the deformation zones are generally more conductive than the bedrock in between. The general tendency within the Laxemar-Simpevarp regional model volume is that the hydraulic conductivity decreases with depth in both HCDs and HRDs. The Quaternary deposits, called Hydraulic Soil Domains (HSD) in the hydrogeological model are generally more conductive than the bedrock. Figure 2-2 shows a generalised vertical section illustrating the overall hydrological and hydrogeological conceptual model of the Laxemar-Simpevarp area. The hydrogeological characteristics of the HCDs, HRDs and HSDs are further described in sections 2.3.2 through 2.3.4 and 2.4; details are found in /Rhén et al. 2008/.

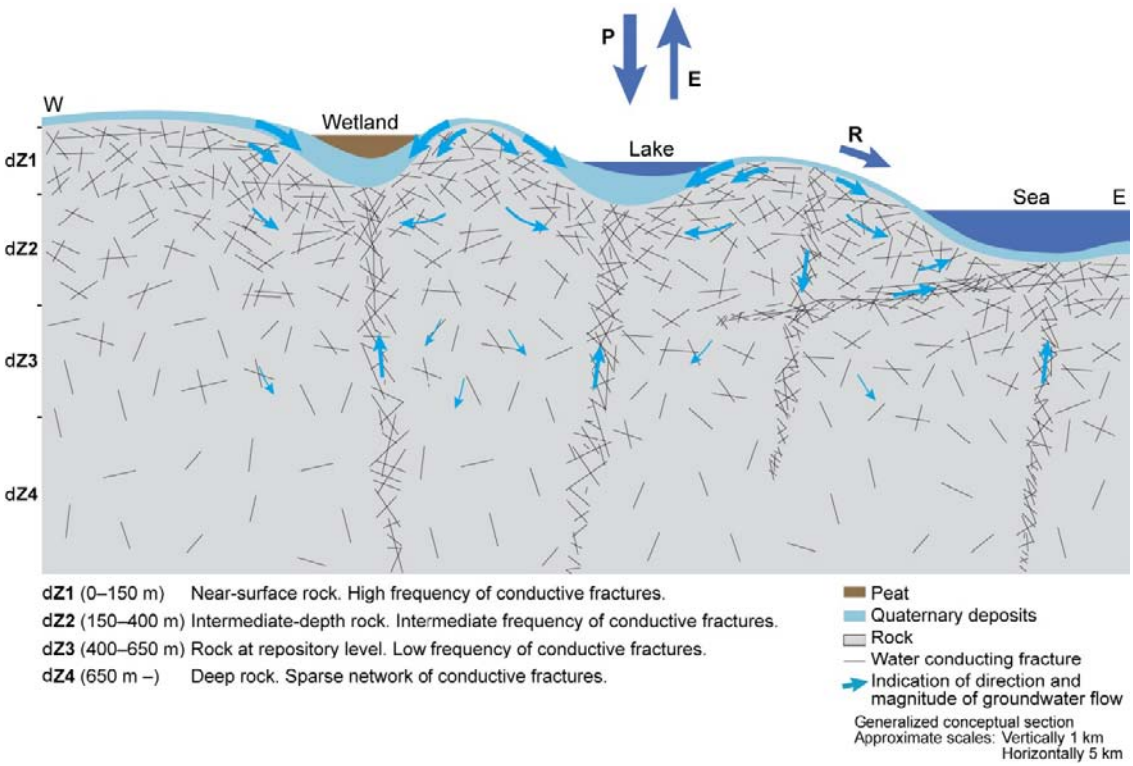

Figure 2-2. *Generalised section illustrating the conceptual model of hydrology and hydrogeology in Laxemar. Note the different horizontal (5 km) and vertical (1 km) scales. Furthermore, the thickness of the Quaternary deposits is exaggerated in the figure. /Rhén and Hartley 2009/.*

2.3.2 Hydraulic characteristics of hydraulic conductor domains (HCD)

The deformation zone model, as implemented in the SDM-Site regional flow domain, is shown in Figure 2-3.

The key interpreted characteristics are:

- A clear trend of decreasing transmissivity with depth.
- A positive correlation between interpreted deformation zone "size" and transmissivity. Size here corresponds to interpreted trace length on the surface.
- Indications that the transmissivity of HCDs is dependent on the orientation of deformation zones. E–W zones appear more conductive than zones of other orientations.
- Significant lateral variability with an estimated standard deviation of $\log_{10}(T)$ of 1.4. The standard deviation of $\log_{10}(T)$ of the entire sample of HCD transmissivities is 1.4 and standard deviation of $\log_{10}(T)$ of transmissivities within individual zones is in the range 0.5 to 2. Sample sizes within individual zones were between 2 to 14.

The data and the general models suggested for the initial assignment of hydraulic properties to HCDs in the groundwater flow modelling are presented in Figure 2-4 cf. a detailed account in /Rhén et al. 2008/. The variability in transmissivity is large but considering mean values for depth zones employed in the HRD modelling, see Figure 2-4, the transmissivity decreases with depth, cf. /Rhén et al. 2008/. There is also a tendency that the transmissivity is positively correlated to the interpreted lineament length of the HCD and also that HCDs with E–W orientations are slightly more transmissive than HCDs of other orientations, cf. /Rhén et al. 2008/.

However, some of the HCDs are intersected by several boreholes at a range of depths and it was judged that there was enough data for assessment of zone-specific trend functions for seven of the HCDs, cf. /Rhén et al. 2008/.

An exponential trend model is used for the depth trend of the transmissivity:

$$T(z) = 10^{(a+B\cdot z)} \qquad (2\text{-}1)$$

z: Elevation in m (m.a.s.l.) (z defined positive up). The coefficients *a* and *B* in the exponential trend model are based on a linear regression of log10(T) data from surface down to lower most depth zone. See /Rhén et al. 2008/ for details.

Several interference tests have shown that dolerite dykes may act as hydraulic barriers, at least locally. The best example relates to the steep N-S oriented HCD ZSMNS001C just west of the focused area, associated with a core of dolerite, cf. /Rhén and Hartley 2009/. Both interference tests and monitoring data show fairly large differences in hydraulic head on either side of two other HCDs associated with dolerite dykes, ZSMNS059A and the KLX19_DZ5-8_dolerite, are also acting as hydraulic barriers, but probably to a lesser degree where the dykes become thinner. Mapping of the cored boreholes and outcropping deformation zones has shown that fault gouge is present in some deformation zones. This implies that these HCDs can exert some hydraulic barrier effect, most likely highly localised.

The distribution of the mean transmissivity in the HCD for the *base case*[1] is shown in Figure 2-5. For stochastic realisations with lateral heterogeneity within SDM-Site, these values are used as the mean sampled value for a log-normal distribution with specified standard deviation, but truncated at ± 2 standard deviations. Equivalent plots for one example realisation of the HCD with spatial variability, standard deviation in $\log_{10}(T) = 1.4$, is shown in Figure 2-6. In both cases, the heterogeneous transmissivity field is conditioned to measured values at the intercept with borehole intervals where measurements are available. Thus, the local contact between the formation and the borehole will be as measured and not dependent on the realisation of the spatial distribution of the transmissivities, which is important when measurements are compared to simulated entities.

[1] *"Base case"* in /Rhén and Hartley 2009/ accounting for the SDM-Site Laxemar modelling corresponds to "*Deterministic base model simulation"* in the SDM-Site Forsmark modelling /Follin 2008/.

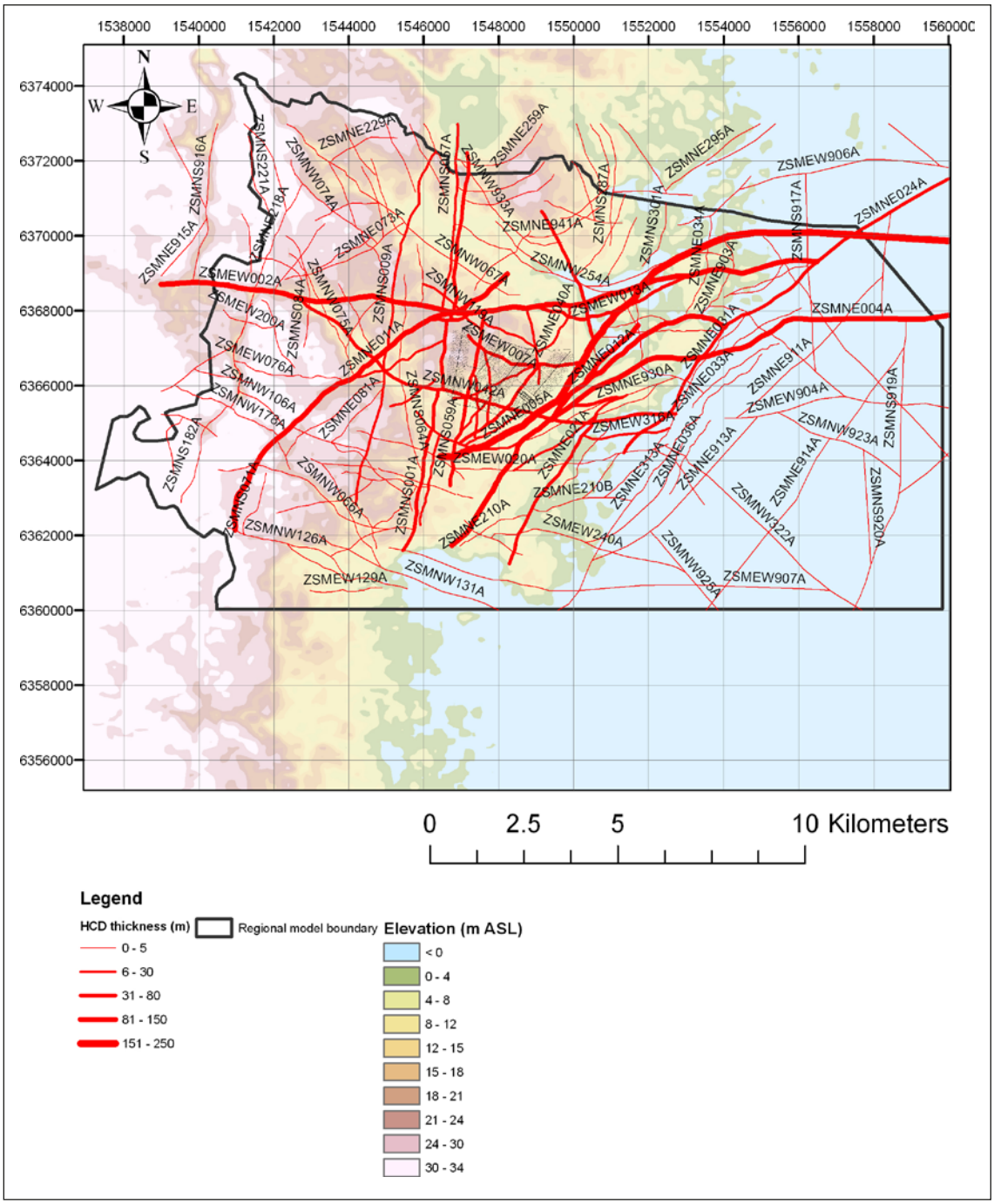

Figure 2-3. *Deformation zones included in the SDM-Laxemar deterministic deformation zone model. Colouring of zones is according to judged thickness.*

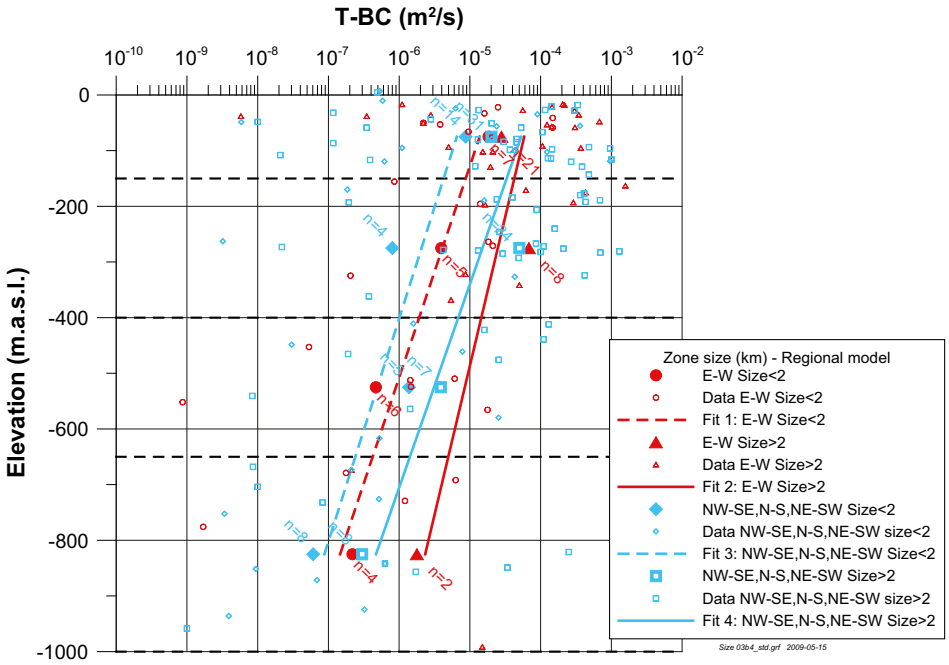

Figure 2-4. *Deformation zone transmissivity (T) related to deformation zone orientations in the horizontal plane and size, versus elevation for the regional model. Mean of $log_{10}(T)$, plotted as well as the number of observations (n). Regression line based on Mean of log10(T) /Rhén and Hartley 2009/.*

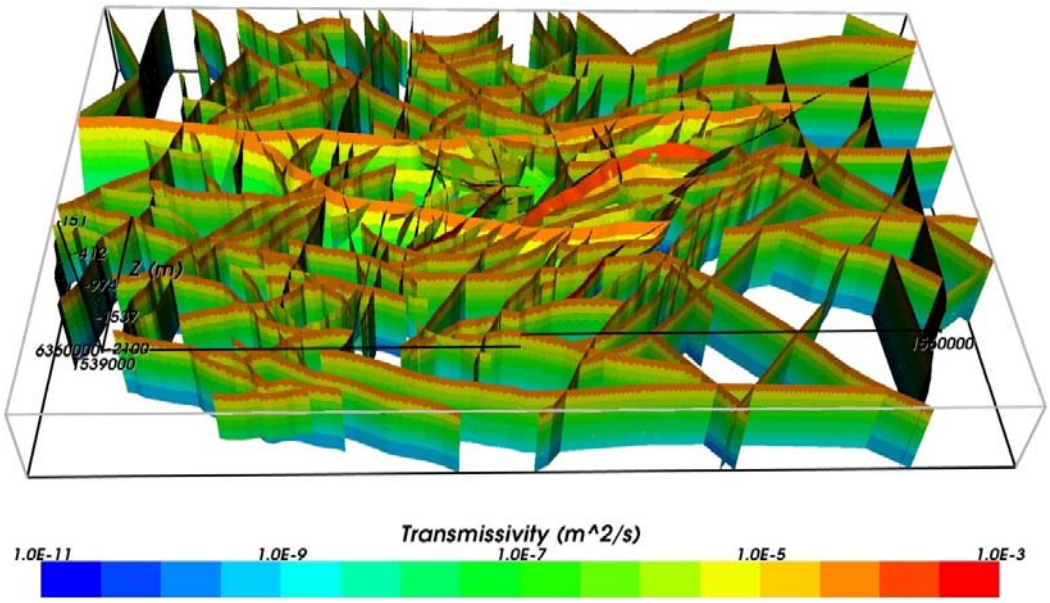

Figure 2-5. *All HCDs and their inferred depth dependent transmissivity for the deterministic base case model. Oblique view looking from the south. /Rhén and Hartley 2009/.*

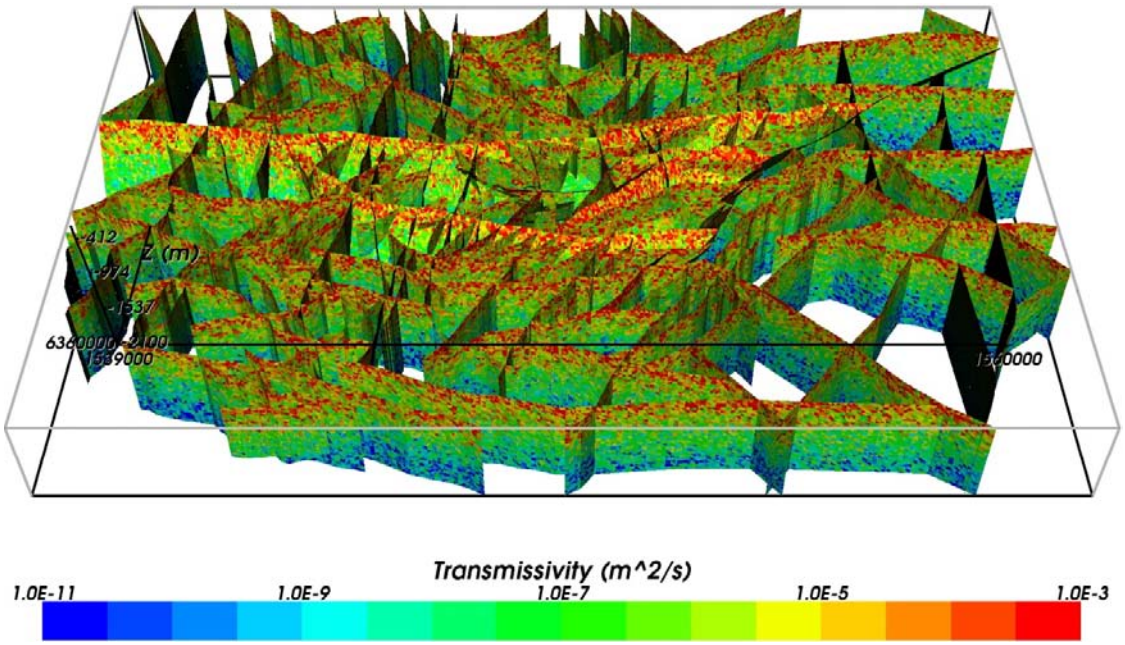

Figure 2-6. *All HCDs and their inferred depth dependent transmissivity for a case with spatial variability and a standard deviation in Log(T) of 1.4. Oblique view looking from the south. /Rhén and Hartley 2009/.*

2.3.3 Hydraulic characteristics of hydraulic rock mass domains (HRD)

The hydraulic rock mass domain model, as implemented in the SDM-Site regional flow domain, is shown in Figure 2-7 though Figure 2-10. According to /Rhén et al. 2008/, four separate hydraulic rock mass domains (HRD) should be modelled in the local model area; HRD_C, HRD_EW007, HRD_N and HRD_W, that are based on the fracture domains, cf. Figure 2-9, Figure 2-10 and /Wahlgren et al. 2008/.

The key interpreted characteristics are:

- The flowing features (fractures and minor deformation zones) can be grouped in four orientation sets; steep ENE, WNW, N-S and a sub-horizontal set.
- The intensity of flowing features is generally highest for the WNW set (aligned with the principal horizontal stress) with the sub-horizontal set also being important in the upper bedrock.
- A clear decreasing intensity of flowing features with depth but generally with a similar transmissivity distribution of the flowing features for the specific depth interval studied (as measured by difference flow logging; PFL-f).
- As a consequence, a resulting clear trend of decreasing hydraulic conductivity with depth, (injection tests, test scale 100 m) may be observed.
- The hydraulic conductivity is c. 10 times lower in HRDs than that of the HCDs (injection tests, test scale 100 m).

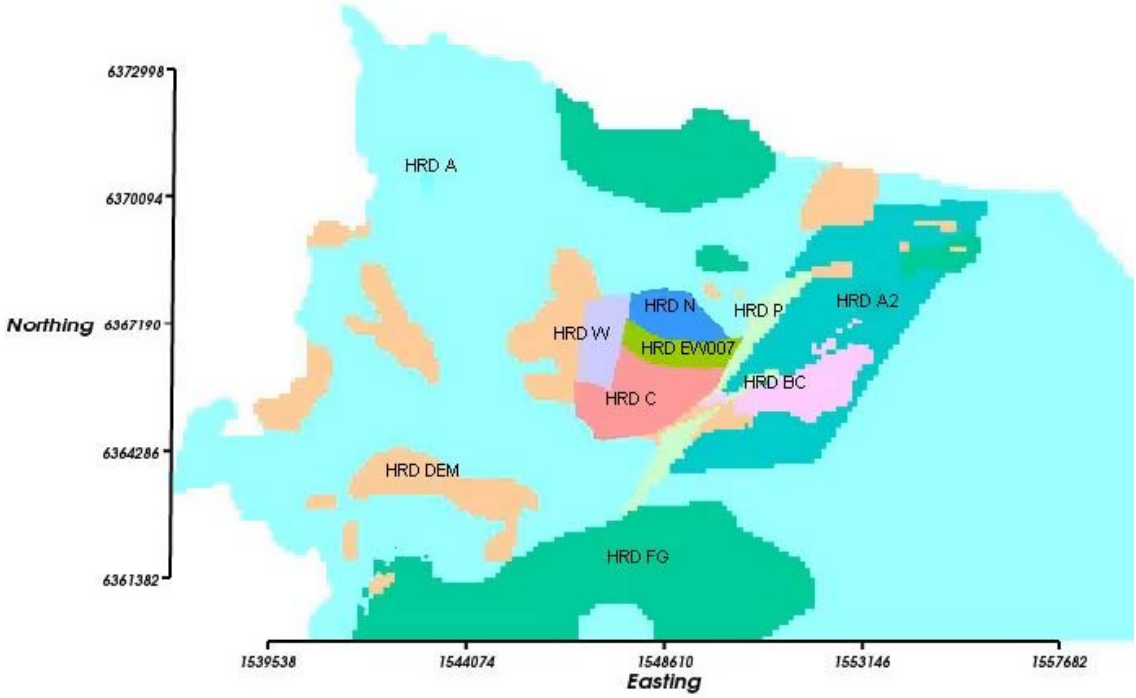

Figure 2-7. *Hydraulic rock mass domains on the top surface of the bedrock in the regional flow domain. /Rhén and Hartley 2009/.*

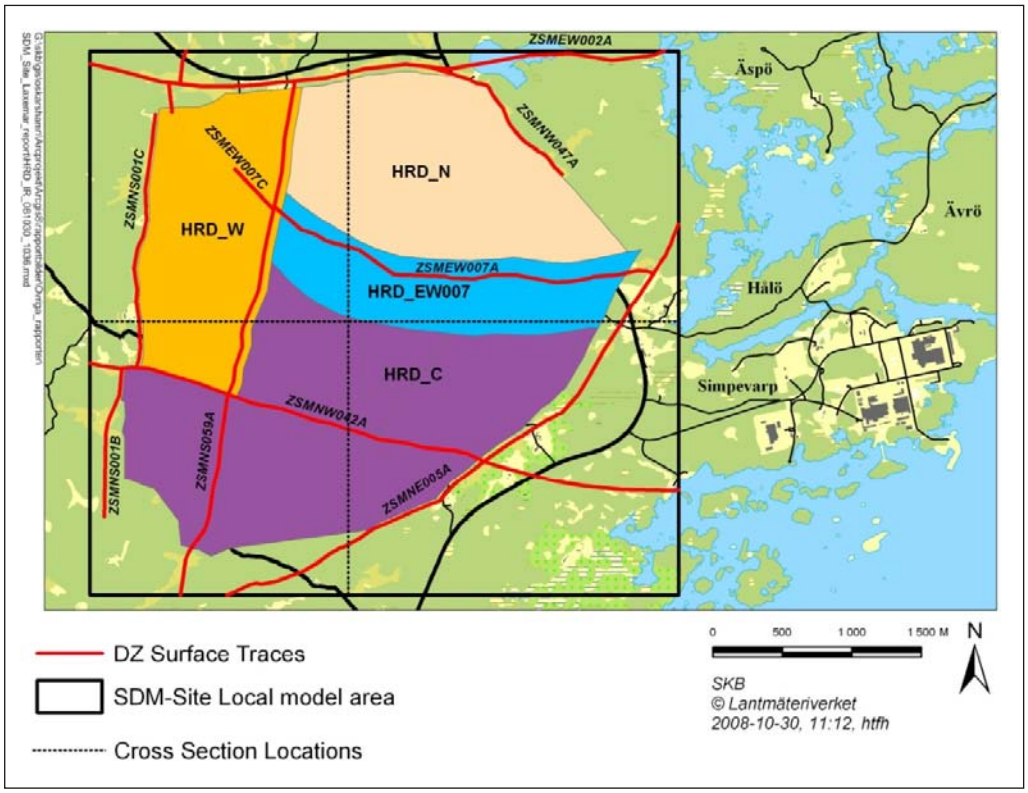

Figure 2-8. *Illustration of the SDM-Site Laxemar Hydraulic Rock Mass Domain Model. Horizontal view. DZ: Deformation zone. /Rhén and Hartley 2009/.*

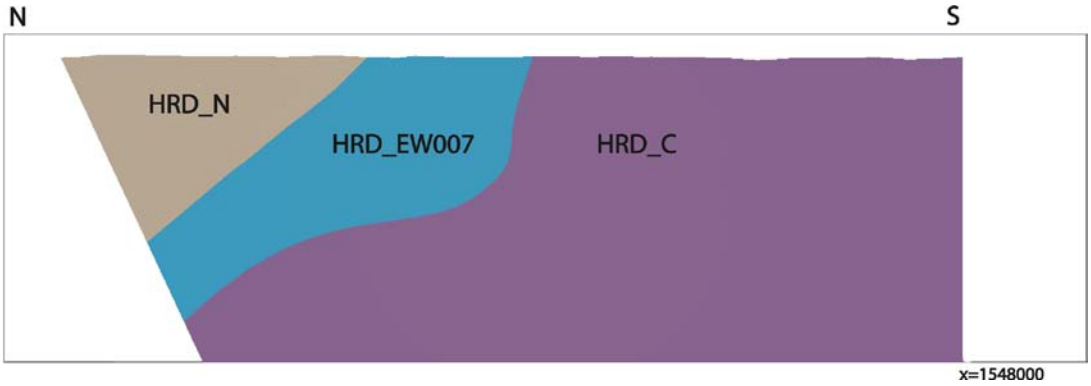

Figure 2-9. *Illustration of the SDM-Site Laxemar Hydraulic Rock Mass Domain Model. Vertical section from north (left) to south-at Easting's X = 154,800 m, /Rhén and Hartley 2009/.*

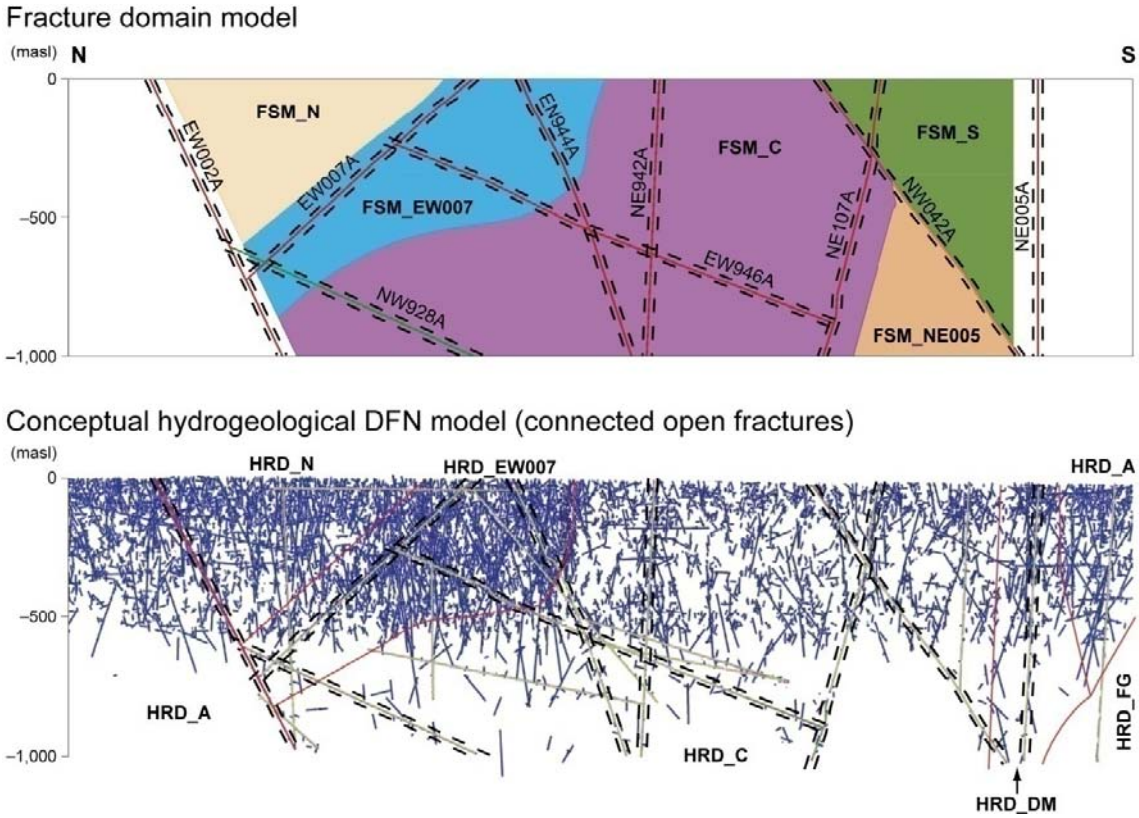

Figure 2-10. *Comparison of conceptual models for fracture domains, hydraulic DFN and associated hydraulic rock mass domains along the N-S section cf. Figure 2-8. The length of the section is ~ 4,300 m. /SKB 2009a/.*

The rock mass in the regional flow domain, outside the defined four HRDs mentioned above, is based on the material property assignments made in model version Laxemar 1.2 /SKB 2006b, Rhén et al. 2006c/ (summarised in /Rhén et al. 2009/) and assessments of similarities between regional HRDs and the newly developed HRDs inside the Laxemar local model volume; HRD_C, HRD_EW007, HRD_N and HRD_W, cf. Table 2-2.

Table 2-2. Proposed hydraulic property assignment of the regional-scale hydraulic rock mass domains to be used in SDM regional groundwater flow modelling /Rhén et al. 2008/.

Regional hydraulic rock mass domain	Suggested hydraulic properties based on hydrogeological DFN
HRD_A	HRD_N
HRD_A2	HRD_N, but rock below –650 m.a.s.l. is the same as –400 m.a.s.l. to –650 m.a.s.l.
HRD_D-E-M	HRD_C
HRD_B-C	HRD_C
HRD_F-G	HRD_N, but 10 times higher T
HRD_P	HRD_N

2.3.4 Hydraulic characteristics of the focused volume

The focused volume, cf. Figure 1-6 comprises, HRD_C, HRD_W and the southern part of HRD_EW007, cf. Figures 1-6 and 2-8. HRD_EW007 is more conductive compared to HRD_C and HRD_W. An example of data used for the calibration of the hydrogeological DFN model is shown in Figure 2-11. The base case for SDM-Site Laxemar assumes a semi-correlated transmissivity model, cf. Table 2-3. The general characteristics of the HRDs illustrated in Figure 2-2 are summarised in Table 2-4 and in Table 2-5 an example of hydrogeological DFN parameters is shown.

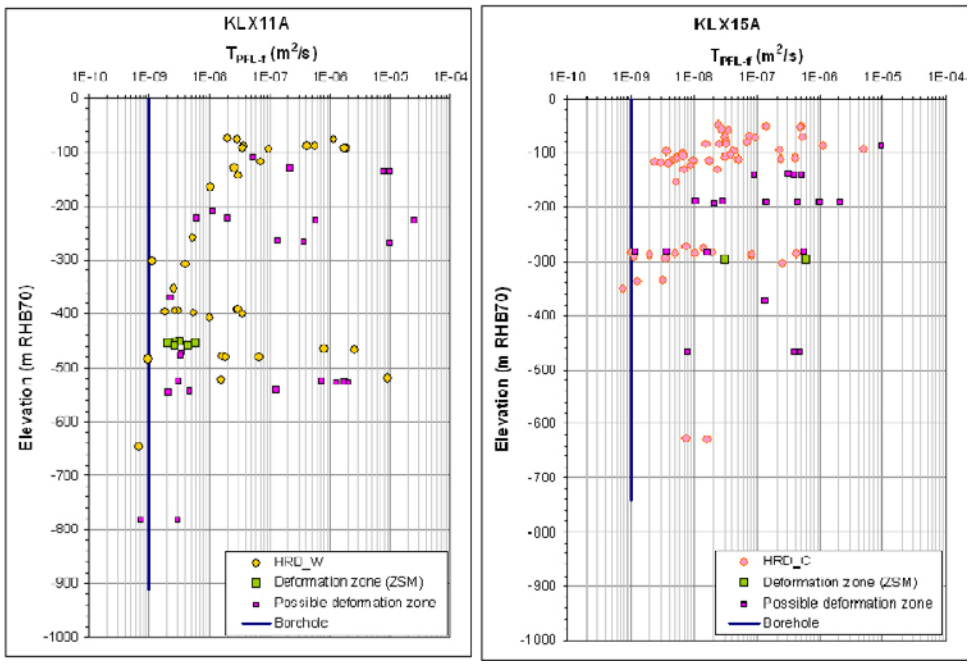

Figure 2-11. *Measured transmissivities (based on PFL-f) in fractures, located in deformation zones (squares) and in hydraulic rock mass domains (circles), in boreholes in the focused volume exemplified with two boreholes; KLX11A (HRD_W) and KLX15A (HRD_C) /SKB 2009a/.*

Table 2-3. Transmissivity parameters used for all sets when matching measured PFL-f flow distributions. (Log base 10) /Rhén et al. 2008/.

Type	Description	Relationship	Parameters
Correlated	Power-law relationship	$\log(T) = \log(a\, r^{b})$	a , b
Semi-correlated	Log-normal distribution about a power-law correlated mean	$\log(T) = \log(a\, r^{b}) + \sigma_{log(T)}$ N[0.1]	a , b, $\sigma_{log(T)}$
Uncorrelated	Log-normal distribution about a specified mean	$\log(T) = \mu_{log(T)} + \sigma_{log(T)}$ N[0.1]	$\mu_{log(T)}$, $\sigma_{log(T)}$

Table 2-4. Schematic summary of groundwater flow and solute transport characteristics under the current temperate climate conditions. Based on /Rhén et al. 2009/.

Depth zone	General characteristics
dZ1: > –150 m	Near-surface rock, characterised by a high intensity of conductive fractures. Sub-horizontal and steeply dipping fractures striking WNW dominate.
	Advection dominated – high groundwater flow rates with sub horizontal fracturing giving $K_h > K_v$ in many areas. Flushed by post-glacial meteoric water. High fracture intensity implies matrix blocks 1–2 m in size, which gives equilibrium in salinity between fracture and matrix by diffusion on timescales of ~1,000 years.
dZ2: –150 m to –400 m	Intermediate-depth rock, characterised by an intermediate intensity of conductive fractures. Steeply dipping fractures striking WNW dominate except in HRD_W where no set is clearly dominant and in HRD_N and HRD_C the sub horizontal set is also important beside the WNW set.
	Some advection, but rock matrix diffusion (RMD) retards post-glacial meteoric penetration. Fracture intensity is generally much lower, reducing groundwater flux and increasing matrix blocks to typically ~5 m in size, such that porewater chemistry lags behind that of the fracture water by 1,000s of years.
dZ3: –400 m to –650 m	Rock at repository level, characterised by a low intensity of conductive fractures. Steeply dipping fractures striking WNW dominate except for HRD_W where no set is clearly dominant.
	Low advection. RMD important because advective flow rates are small. Fracture intensity lower still, with typical matrix blocks ~10 m in size, such that porewater chemistry lags behind that of fracture water ~10,000 years.
dZ4: < –650 m	Deep rock, characterised by a sparse network of conductive fractures. Steeply dipping fractures striking WNW dominate except for HRD_W where no set is clearly dominant (however rather few data occur within dZ4).
	Very low advection. RMD dominates. Fracture intensity very low, with typical matrix blocks ~100 m in size, such that porewater chemistry lags behind that of fracture water ~100,000 years.

Table 2-5. Description of the calibrated hydrogeological DFN input parameters for HRD_C with fixed r_0 = 0.038 m and intensity of open fractures based OPO (Open and Partly Open fractures). /Rhén et al. 2008/.

Depth zone (m.a.s.l.)	Set	Orientation set pole: (trend, plunge), conc. (°,°,–)	Fracture radius model power-law (k_r, r_0)	Intensity P_{32} (m^2/m^3) of open fractures	Transmissivity model T (m^2/s) See Table 2-3.
–150 to 0	ENE	(155.1,3.4), 9.6	(2.6, 0.038)	0.52	SC: ($6\cdot10^{-8}$, 0.5, 0.4) UC: ($2\cdot10^{-7}$, 0.6) C: ($2\cdot10^{-8}$, 0.9)
	WNW	(204,1.6), 12	(2.5, 0.038)	0.95	SC: ($2\cdot10^{-7}$, 0.6, 0.7) UC: ($1\cdot10^{-5}$, 0.9) C: ($5\cdot10^{-8}$, 1.1)
	N-S	(270.2,8.4), 7.8	(2.7, 0.038)	0.54	SC: ($2\cdot10^{-7}$, 0.6, 0.5) UC: ($1\cdot10^{-7}$, 0.7) C: ($6\cdot10^{-8}$, 1.2)
	Sub-H	(46.3,84.7), 12	(2.7, 0.038)	1.20	SC: ($1.5\cdot10^{-7}$, 0.7, 0.7) UC: ($3\cdot10^{-7}$, 0.8) C: ($6\cdot10^{-8}$, 1.0)
–400 to –150	ENE	(155.1,3.4), 9.6	(2.85, 0.038)	0.47	SC: ($1\cdot10^{-6}$, 0.7, 0.7) UC: ($2\cdot10^{-7}$, 0.7) C: ($5\cdot10^{-8}$, 1.4)
	WNW	(204,1.6), 12	(2.45, 0.038)	0.55	SC: ($8\cdot10^{-8}$, 0.3, 0.1) UC: ($3\cdot10^{-7}$, 0.6) C: ($2\cdot10^{-9}$, 1.3)
	N-S	(270.2,8.4), 7.8	(2.85, 0.038)	0.63	SC: ($1\cdot10^{-7}$, 0.7, 0.7) UC: ($2\cdot10^{-7}$, 0.4) C: ($3\cdot10^{-8}$, 1.0)
	Sub-H	(46.3,84.7), 12	(2.85, 0.038)	0.71	SC: ($1.5\cdot10^{-7}$, 0.8, 0.9) UC: ($8\cdot10^{-7}$, 1.4) C: ($3\cdot10^{8}$, 1.1)
–650 to –400	ENE	(155.1,3.4), 9.6	(2.8, 0.038)	0.38	SC: ($5\cdot10^{-7}$, 0.5, 0.5) UC: ($2\cdot10^{-6}$, 0.8) C: ($3\cdot10^{-8}$, 0.7)
	WNW	(204,1.6), 12	(2.5, 0.038)	0.74	SC: ($2\cdot10^{-8}$, 0.6, 0.4) UC: ($1\cdot10^{-7}$, 0.9) C: ($3\cdot10^{-9}$, 0.9)
	N-S	(270.2,8.4), 7.8	(2.9, 0.038)	0.47	SC: ($1\cdot10^{-8}$, 0.4, 0.4) UC: ($8\cdot10^{-8}$, 0.4) C: ($1\cdot10^{-8}$, 0.5)
	Sub-H	(46.3,84.7), 12	(2.9, 0.038)	0.58	SC: ($3\cdot10^{-7}$, 0.6, 0.6) UC: ($2\cdot10^{-6}$, 0.9) C: ($1.5\cdot10^{-7}$, 0.9)
–1,000 to –650	ENE	(155.1,3.4), 9.6	(2.9, 0.038)	0.46	SC: ($5\cdot10^{-9}$, 0.6, 0.4) UC: ($1\cdot10^{-8}$, 0.4) C: ($5\cdot10^{-9}$, 0.6)
	WNW	(204,1.6), 12	(2.8, 0.038)	0.73	SC: ($5\cdot10^{-8}$, 0.6, 0.4) UC: ($5\cdot10^{-7}$, 0.4) C: ($5\cdot10^{-8}$, 0.6)
	N-S	(270.2,8.4), 7.8	(2.95, 0.038)	0.25	SC: ($5\cdot10^{-9}$, 0.6, 0.4) UC: ($1\cdot10^{-8}$, 0.4) C: ($5\cdot10^{-9}$, 0.6)
	Sub-H	(46.3,84.7), 12	(2.95, 0.038)	0.35	SC: ($1\cdot10^{-7}$, 0.6, 0.4) UC: ($2\cdot10^{-7}$, 0.4) C: ($1\cdot10^{-7}$, 0.6)

2.4 Summary of the Quaternary deposits hydrogeological model (HSD)

The stratigraphical distribution of Quaternary deposits in the investigated area is rather uniform. Till is the oldest Quaternary deposit in the area, and is consequently resting directly upon the bedrock surface. The till in the valleys is often overlain by glacial clay, which in many valleys is overlain by a thin layer of sand followed by clay gyttja and peat.

The model developed by /Nyman et al. 2008/ contains six layers of Quaternary deposits, denoted Z1–Z6; Z1 represents the upper layer of the Quaternary deposits. These layers, illustrated in the cross section in Figure 2-12, are defined and described briefly in /Rhén et al. 2009/ and in /Nyman et al. 2008, Sohlenius and Hedenström 2008/.

Figure 2-13 shows the modelled distribution of total overburden depth in the Laxemar-Simpevarp regional model area. Figure 2-14 illustrates the variable depth of the Quaternary deposits along a vertical north-south section across the E-W regional deformation zone in the northern part of the local model domain; the Mederhult zone (ZSMEW002A).

This detailed Quaternary deposit model was simplified in the SDM-Site regional groundwater flow modelling representing it by four element layers vertically, each of a constant 1 m thickness, with the horizontal extent of the hydrogeological grid element (40–120 m), to represent the HSD. The same hydraulic conductivity tensor was specified for each element in a vertical stack of 4 grid elements, but varied horizontally from element-to-element, and was anisotropic with regard to horizontal and vertical components in order to represent the effective hydraulic properties of the Quaternary deposit layers. The effective hydraulic conductivity tensor for the soil package was calculated according to the actual modelled thickness of the layers of the Quaternary deposits and the hydraulic conductivities of the soil types at that location. HSD properties used in the SDM-Site base case model are described in Table 2-6 and illustrated in Figure 2-15. See /Rhén et al. 2009/ for details of the implementation.

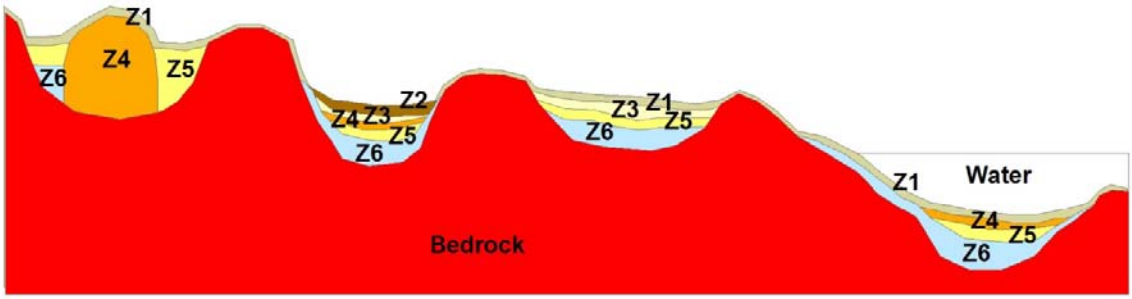

Figure 2-12. *The stratigraphical model which was used for modelling stratigraphy and total depth of Quaternary deposits in the Laxemar-Simpevarp regional model area. /Sohlenius and Hedenström 2008/.*
Layer Z1–6:
Layer Z1 represents a thin surface(-affected) layer.
Layer Z2 represents (fen or bog) peat.
Layer Z3 represents postglacial clay, clay gyttja/gyttja clay, gyttja or recent fluvial sediments.
Layer Z4 represents postglacial sand/gravel, glaciofluvial sediments or artificial fill.
Layer Z5 represents glacial clay.
Layer Z6 represents (glacial) till.

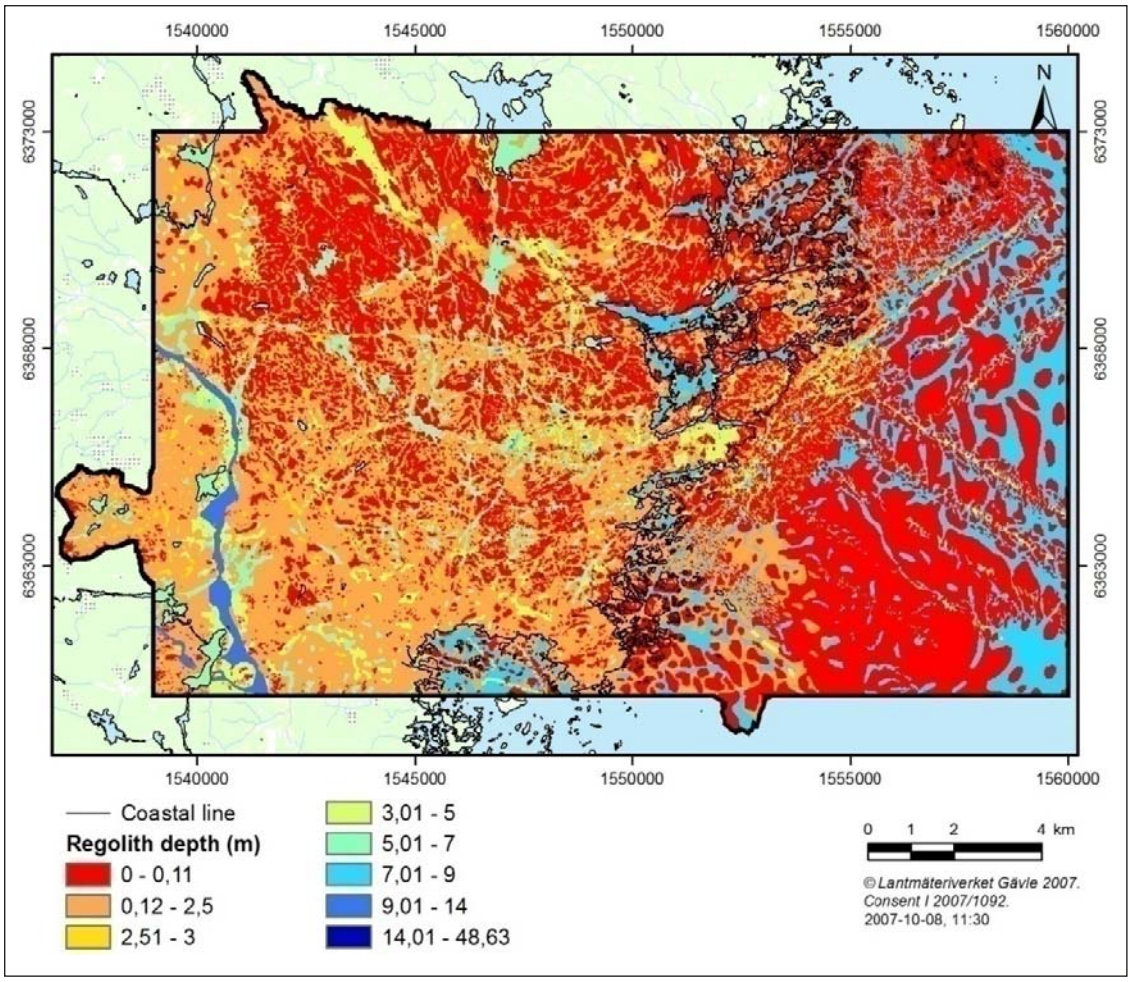

Figure 2-13. *The modelled distribution of total depths of the Quaternary deposits in the Laxemar-Simpevarp area. /Sohlenius and Hedenström 2008/.*

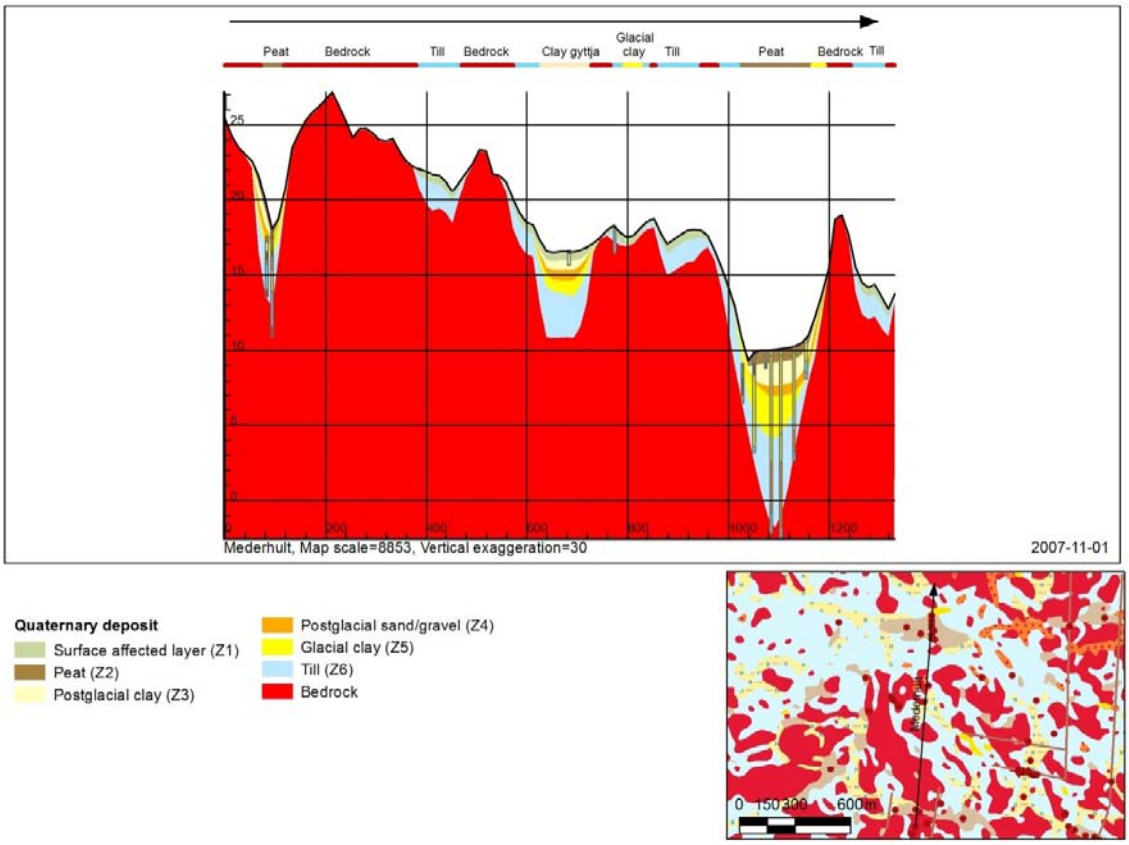

Figure 2-14. *The profile shows the total depth and stratigraphy of the Quaternary deposits in a north-south profile close to Mederhult. The valley in the right part of the profile (between 1,000 and 1,200 on the horizontal scale) is one of the largest lineaments in the model area (ZSMEW002A , cf. /Rhén et al. 2009, Figure 3-1/), /Sohlenius and Hedenström 2008/.*

Table 2-6. Prescription for hydrogeological properties of Hydraulic soil property domains used in the hydrogeological modelling (based on /Werner et al. 2008/). The relation to the model and description of the Quaternary Deposits (QD type and layer) /Nyman et al. 2008, Sohlenius and Hedenström 2008, Werner et al. 2008/ is given in the second column. The modifications relative to the initial HSD assignments are highlighted in bold font, with the main change being to introduce anisotropy. Porosity is derived from specific yield /Werner et al. 2008/. /Rhén and Hartley 2009/.

Hydraulic soil property domain	QD type and layer applied to	*K* (m/s)	Porosity
Surface affected layer	Soil > 5 m thick: QD type: 1, 2, 5, 6, 7, 9, 13, 16, 17, 18, 20, 22, 24, 25, 26, 27 Layer Z1 Domain 2–24 Layer Z6	$\boldsymbol{K_h = 8 \cdot 10^{-4}}$ $\boldsymbol{K_h/K_v = 10:1}$ Original: $4 \cdot 10^{-4}$	0.15
Peat	QD type: 11, 12 Layer Z2	$K_h = 3 \cdot 10^{-6}$ $\boldsymbol{K_h/K_v = 10:1}$	0.24
Glacial clay	QD type: 6, 8, 9, 10, 12 Layer Z3	$K_h = 1 \cdot 10^{-7}$ $\boldsymbol{K_h/K_v = 10:1}$	0.03
Postglacial sand/gravel	QD type: 6, 7, 8, 9, 10, 12 13, 14, 15, 16, 20, 23, 24, 25, 26 Layer Z4	$K_h = 5 \cdot 10^{-3}$ $\boldsymbol{K_h/K_v = 10:1}$	0.25
Glacial clay	QD type: 6, 8, 9, 10, 12, 13, 14, 15, 16, 17, 18, 19, 20, 21, 22, 23, 24 Layer Z5	$K_h = 1 \cdot 10^{-8}$ $\boldsymbol{K_h/K_v = 2:1}$	0.03
Till	Soil < 5 m thick: QD type: 1, 2, 5, 6, 7, 9, 13, 16, 17, 18, 20, 22, 24, 25, 26, 27 Layer Z1 Domain 2–24 Layer Z6	$K_h = 4 \cdot 10^{-5}$ $\boldsymbol{K_h/K_v = 10:1}$	0.05
Surface affected peat	QD type: 3, 8, 21, 23 Layer Z1	$K_h = 3 \cdot 10^{-6}$ $\boldsymbol{K_h/K_v = 10:1}$	0.24
Surface affected shingle	QD type: 4 Layer Z1	$K_h = 1 \cdot 10^{-2}$ $\boldsymbol{K_h/K_v = 10:1}$	0.25
Surface affected sand	QD type: 10, 15 Layer Z1	$K_h = 1 \cdot 10^{-2}$ $\boldsymbol{K_h/K_v = 10:1}$	0.25
Gyttja	QD type: 7 Layer Z3	$K_h = 1 \cdot 10^{-8}$ $\boldsymbol{K_h/K_v = 2:1}$	0.03
Postglacial fine sand	QD type: 17 Layer Z4	$K_h = 5 \cdot 10^{-4}$ $\boldsymbol{K_h/K_v = 10:1}$	0.25
Postglacial sand	Domain 18, 19 Layer Z4	$K_h = 1 \cdot 10^{-3}$ $\boldsymbol{K_{hh}/K_v = 10:1}$	0.25
Postglacial gravel	QD type: 21, 22 Layer Z4	$K_h = 1 \cdot 10^{-2}$ $\boldsymbol{K_h/K_v = 10:1}$	0.25
Artificial fill	QD type: 27 Layer Z4	$K_h = 4 \cdot 10^{-5}$ $\boldsymbol{K_h/K_v = 10:1}$	0.05

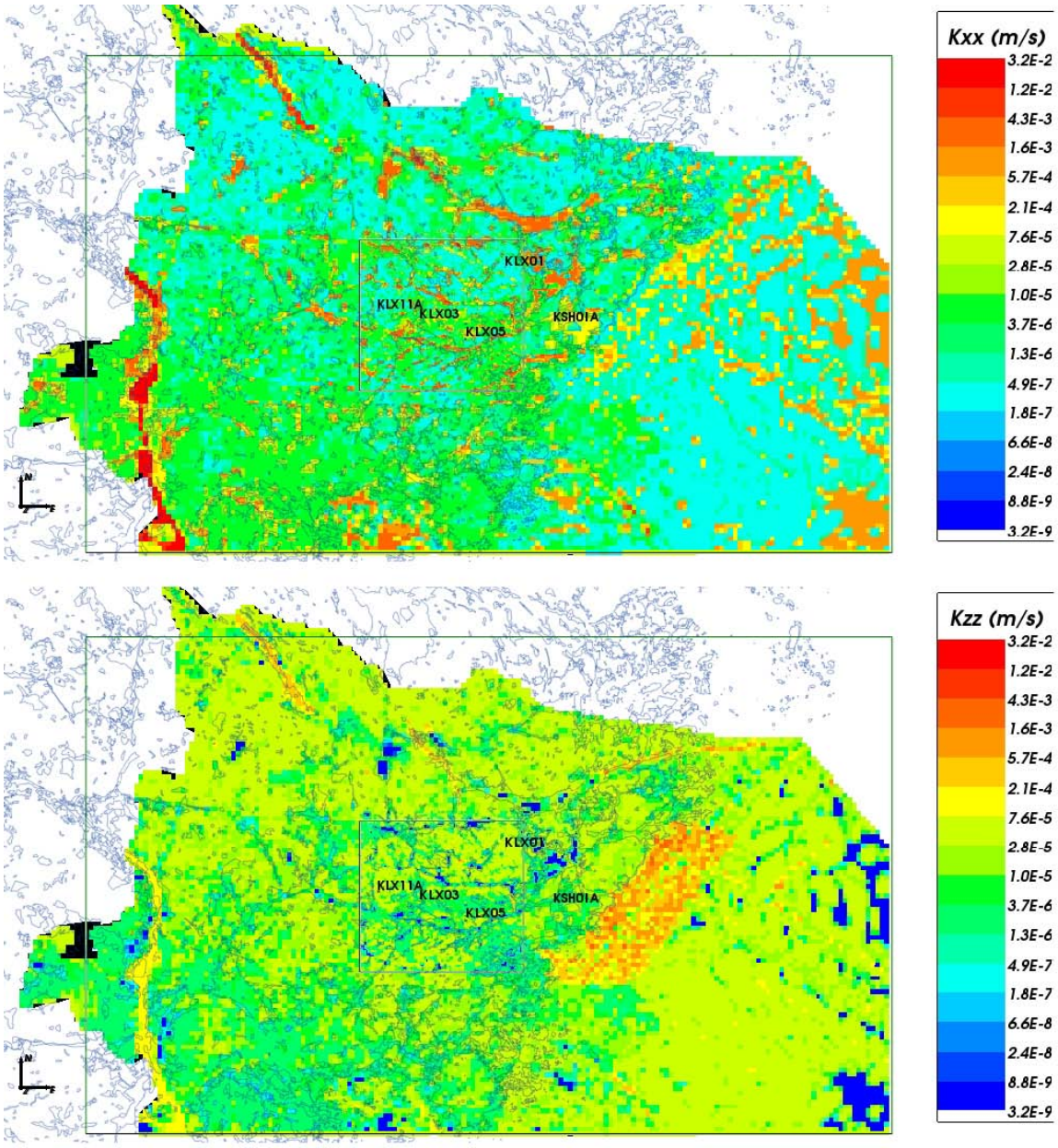

Figure 2-15. *Resulting effective hydraulic conductivity for HSD top layer based on layer thicknesses and hydraulic properties of the Quaternary deposits. Top: E–W horizontal component; Bottom: vertical component. /Rhén and Hartley 2009/.*

2.5 Groundwater flow simulations and confirmatory testing

The SDM-Site regional scale groundwater flow and solute transport simulation tests of palaeohydrogeological evolution, natural head measurements and hydraulic interference test data have confirmed that hydrogeological properties, as given by the SDM-Site hydrogeological DFN model base case /Rhén et al. 2008/ (based on all open and partly open fractures and semi-correlated transmissivity model), together with the HCD parameterisation provide an appropriate description of the hydrogeological situation in the bedrock. Only relatively minor modifications were considered necessary to obtain an acceptable match between the regional groundwater flow model results and field data, cf. /Rhén et al. 2009/ for details.

3 Concepts and methodology

3.1 Governing equations

Coupled groundwater flow and salt transport in fractured rocks that give rise to variations in salinity and hence fluid density are modelled in DarcyTools according to the following formulation of the mass conservation equation:

$$\frac{\partial \rho\phi}{\partial t} + \frac{\partial}{\partial x}(\rho u) + \frac{\partial}{\partial y}(\rho v) + \frac{\partial}{\partial z}(\rho w) = Q \tag{3-1}$$

where ρ is fluid density [ML^{-3}], ϕ is the kinematic porosity [–], t is time [T], (u, v, w) are the directional components of the volumetric (Darcy) flux [LT^{-1}] at the location (x, y, z) [L,L,L] in a Cartesian coordinate system, and Q is a source/sink term per unit volume of fluid mass [$ML^{-3}T^{-1}$]. The mass conservation equation is turned into a pressure equation by invoking the assumptions behind Darcy's law:

$$\begin{aligned} \rho u &= -\frac{K_x}{g}\frac{\partial P}{\partial x} \\ \rho v &= -\frac{K_y}{g}\frac{\partial P}{\partial y} \\ \rho w &= -\frac{K_z}{g}\frac{\partial P}{\partial z} - K_z(\rho - \rho_0) \end{aligned} \tag{3-2}$$

where K_x, K_y and K_z are the orthogonal components of the hydraulic conductivity tensor parallel to the Cartesian coordinate system [LT^{-1}], g is the acceleration due to gravity [LT^{-2}], ρ_0 is a reference fluid density [ML^{-3}], and P is the dynamic (residual) fluid pressure [$ML^{-1}T^{-2}$] at the location (x, y, z):

$$P = p + \rho_0 g\, z \tag{3-3}$$

where p is the gauge pressure [$ML^{-1}T^{-2}$] and $\rho_0 g\, z$ is the hydrostatic pressure, P_0.

The hydraulic conductivity K is related to the permeability k [L^2] through the relation:

$$K = \frac{\rho\, g}{\mu} k \tag{3-4}$$

where μ is the fluid dynamic viscosity [$ML^{-1}T^{-1}$]. For variable-density flow at isothermal conditions, ρ and μ are given by the following state laws:

$$\rho = \rho_0\,[1+\alpha C] \tag{3-5}$$

$$\mu = \mu_0 \tag{3-6}$$

where α and μ_0 are constants and C represents the salinity (mass fraction) [–]:

$$C = TDS/\rho \tag{3-7}$$

The migration of salt is modelled in DarcyTools in terms of advection and dispersion processes in the mobile (fracture) pore system and as a diffusion process in the immobile (rock matrix) pore system. The advection-dispersion equation for the mobile pore system is modelled in DarcyTools according to the following equation:

$$\begin{aligned} \rho\phi\frac{\partial C}{\partial t} &+ \frac{\partial}{\partial x}\left(\rho u C - \rho\gamma D_x \frac{\partial C}{\partial x}\right) \\ &+ \frac{\partial}{\partial y}\left(\rho v C - \rho\gamma D_y \frac{\partial C}{\partial y}\right) \\ &+ \frac{\partial}{\partial z}\left(\rho w C - \rho\gamma D_z \frac{\partial C}{\partial z}\right) = QC + Q_C \end{aligned} \tag{3-8}$$

where D_x, D_y and D_z are the orthogonal components of the diffusion-dispersion tensor parallel to the Cartesian coordinate system [L^2T^{-1}], Q_c represents the diffusive exchange of salt per unit volume of fluid mass between the mobile and immobile pore volumes [$ML^{-3}T^{-1}$], and γ is a dimensionless coefficient that describes the dependency of the kinematic porosity of the mobile pore system on the dynamic pressure:

$$\phi = \phi_0 \gamma \tag{3-9}$$

$$\gamma = 1 + \frac{S_s}{\phi_0}\frac{(P - P_0)}{\rho g} \tag{3-10}$$

where S_s is the specific storage of the mobile pore system [L^{-1}].

3.2 Methodology

3.2.1 Finite volume method

DarcyTools uses a staggered computational grid, which means that scalar quantities such as pressure, flow porosity and salinity use a cell-centred mesh, whereas directional quantities such as hydraulic conductivity, hydrodynamic diffusivity, mass flux, and Darcy flux use a mesh centred at the cell walls. This grid arrangement was first introduced by /Harlow and Welch 1965/ and is described in textbooks, e.g. /Patankar 1980/. Each variable is assumed to be representative for a certain control volume, which is the volume for which the equations are formulated. DarcyTools uses the finite volume method to transform the differential equations into algebraic equations of the type:

$$a_P\Phi_P = a_W\Phi_W + a_E\Phi_E + a_S\Phi_S + a_N\Phi_N + a_B\Phi_B + a_T\Phi_T + S_\phi \tag{3-11}$$

where Φ denotes the variable in question, a_i are coefficients and S_ϕ source/sink terms. The equations are solved by the MIGAL multi-grid equation solver /Svensson et al. 2010/.

3.2.2 Continuum representation of hydraulic properties of discrete fractures

Principle

The principle used to represent hydraulic properties of discrete fractures as equivalent grid cell hydraulic properties in DarcyTools works as follows:

A fracture variable (P_f) contributes to the grid cell variable (P_c) by an amount which is equal to the intersecting volume of the fracture ($V_{f,i}$) times the value of the fracture variable. Contributions from all fractures that intersect the grid cell control volume are added and the sum is divided by the volume of the cell (V_c), i.e.:

$$P_c = \sum_f \left(V_{f,i}\, P_f\right) / V_c \tag{3-12}$$

The intersecting volume of the fracture ($V_{f,i}$) may be written as:

$$V_{f,i} = L_{f,i}\, W_{f,i}\, b_{f,i} \tag{3-13}$$

where $L_{f,i}$, $W_{f,i}$ and $b_{f,i}$ denote the physical dimensions (length, width and thickness) of the intersecting fracture in three orthogonal directions. For the sake of simplicity, it is assumed in the equations below that the fracture thickness $b_{f,i}$ is much thinner than the geometrical resolution Δ of the computational grid, i.e. the grid size.

Grid-cell hydraulic conductivity

DarcyTools assumes that fracture transmissivity (T_f) is a scalar quantity and that fracture hydraulic conductivity (K_f) may be written as:

$$K_f = T_f / b_f \tag{3-14}$$

where b_f is the fracture thickness. Thus, the contribution from an intersecting fracture to the hydraulic conductivity of the intersected grid cell may be written as:

$$K_{c,f} = (L_{f,i} W_{f,i} T_f) / V_c \tag{3-15}$$

Since DarcyTools uses a staggered computational grid, $K_{c,f}$ is a directional quantity.

Grid-cell kinematic porosity

DarcyTools assumes that the kinematic porosity of a fracture (ϕ_f) can be written as:

$$\phi_f = e_{T,f} / b_f \tag{3-16}$$

where $e_{T,f}$ is the fracture transport aperture. The fracture transport aperture was modelled based on Äspö Task Force 6c results /Dershowitz et al. 2003/, which assume a power-law function between the fracture aperture and the fracture transmissivity:

$$e_{T,f} = a\,(T_f)^b \tag{3-17}$$

The values of the parameters a and b used in this work are defined in /Dershowitz et al. 2003/, where $a = 0.46$ and $b = 0.5$.

Thus, the contribution from an intersecting fracture to the kinematic porosity of the intersected grid cell can be written as:

$$\phi_{c,f} = (L_{f,i} W_{f,i}\, e_{T,f} / V_c \tag{3-18}$$

3.2.3 Fracture transmissivity

The equations given in Section 3.2.2 reveal that fracture transmissivity is the key hydraulic quantity in DarcyTools, i.e. fracture transmissivity is used to define both grid cell hydraulic conductivity and grid cell kinematic porosity.

DarcyTools assumes that a power-law function prevails between fracture transmissivity and fracture size (L_f). The power-law function may be written as:

$$\log(T_f) = \log\left[a_T \left(\frac{L_f}{100} \right)^{b_T} \right] + d_T\, U[-0.5,0.5] \tag{3-19}$$

where a_T is the transmissivity value of a fracture with $L_f = 100$ m and b_T is the exponent of the power-law function. d_T is a factor that scales a uniformly distributed[2] random deviate U and is used when uncertainty in the power-law function is addressed.

For the sake of clarity it is noted that the relationship between the power-law parameters used in DarcyTools (a_T,b_T) and the corresponding power-law parameters (a,b) derived in SDM-Site and recommended for use in SR-Site Forsmark /Selroos and Follin 2010/ can be written as:

$$b_T = b \tag{3-20}$$

$$a_T = a \left(100 / \sqrt{\pi} \right)^{b_T} \tag{3-21}$$

[2] In SDM-Site Forsmark, the values of the random deviate were generated by means of a truncated normal distribution. This difference was considered arbitrary in the work reported here.

3.2.4 Particle tracking

The particle tracking routine, PARTRACK, has two modes of operation; the first is the classic way of moving the particle along the local velocity vector, whereas the second method uses the so called "flux-weighting" approach, and works as follows.

- A particle entering a scalar cell will, if no dispersion effects are activated, stay in the cell for a time that is equal to the free volume of the cell divided by the flow rate through the cell.
- When the particle is ready to leave the cell, it will leave through one of the cell walls that has an outgoing flow direction. The choice between cell walls with an outgoing flow is made with a likelihood that is proportional to the outflows. If several particles are traced, the cloud will thus split up in proportion to the flow rates. Complete mixing in a cell is assumed.

3.2.5 Diffusive exchange of salt

The diffusive exchange of salt between the immobile and mobile pore systems in DarcyTools is based on the one-dimensional multi-rate diffusion model suggested by /Haggerty and Gorelick 1995/. The concept of diffusion into immobile volumes ranges from short-term diffusion (fast exchange rate) into the stagnant pools of water nearby the flowing fractures, to the long-term diffusion (slow exchange rate) into the less permeable rock (matrix) elsewhere. A more detailed description of the concepts and methodology of the implementation of the multi-rate diffusion model in DarcyTools is found in /Svensson et al. 2010/.

4 Model specification

4.1 Additional concepts and methodology

The concepts and methodology shown in Chapter 3 can be used to satisfy the following two objectives of the work:

- predict the magnitude and spatial distribution of the inflow, and
- predict the magnitude and spatial distribution of the upconing of deep saline water.

In order to fulfil the remaining objectives of the work, i.e:

- predict the magnitude and spatial distribution of the drawdown of the groundwater table,
- predict the role of grouting for the inflow, drawdown and upconing phenomena, and
- predict the saturation period after the open repository has been closed (backfilled),

the following algorithms/routines were added:

- The position of the groundwater table was modelled with a free surface algorithm that can handle both natural conditions and the drawdown due to the inflow to an open repository (Appendix A).
- The impact of grouting on the calculated inflow rates, drawdown of the groundwater table and upconing of deep saline water was studied by altering the hydraulic conductivity of the computational grid cells in contact with the modelled repository (Appendix B). As an example, if the grouting criterion specifies a maximum conductivity of 10^{-8} m/s, all cell wall conductivities are reduced to this value if larger.
- The time scale of the saturation period was estimated by assuming that the hydration process of the unsaturated parts of the backfill can be modelled as single-phase (saturated) groundwater flow, where the specific storage of the backfill varies in space depending on the transients in the dynamic pressure (Appendix C).

4.2 Elaborated Hydro-DFN model

The requirements of the hydrogeological modelling conducted at Laxemar in this work may be summarised as follows:

- The model domain is the same as the model domain used in SDM-Site (Figure 4-1).
- The geometry and hydraulic properties of discrete geological features in the bedrock such as deformation zones (HCD) and fracture network realisations (HRD) are illustrated in Figure 4-2 and Figure 4-3 respectively. (The structural-hydraulic properties of the discrete fracture network (DFN) model represents the Elaborated Hydro-DFN, as briefly described in Section 1.5. For a full account, see /Joyce et al. 2010/. In Appendix E, a comparison between the two DFN models can be found.)
- The hydraulic properties of the uppermost 20 m of the model domain (including the minimum values of the hydraulic properties below 20 m depth) are shown in Table 4-1. The properties for the uppermost 20 m were found from a calibration study.
- The salinity and pressure during the simulation of the excavation and operational phases were fixed on the lateral sides of the model domain implying unaffected steady-state conditions a few kilometres away from the modelled repository.
- The salinity and pressure values used on the lateral boundaries were derived from a simulation of the shoreline displacement and the known changes of the salinity in the Baltic basin in the Laxemar area during Holocene time, i.e. between 8000 BC and 2000 AD (Figure 4-5). (The lateral surfaces of the model domain were modelled as impervious boundaries (no flow and no diffusion of salt) during Holocene time and the initial conditions at 8000 BC were in accordance with those used in the SDM work (Table 4-2).

- The terrestrial parts of the top surface of the model area were assigned a fixed maximum value of the mean net precipitation of 165 mm/year of fresh water in all simulations. Likewise, the bottom surface of the model domain was modelled as an impervious flow boundary with a fixed salinity in all simulations. The bottom surface was located at the same depth as in the SDM work, –2,100 m elevation.
- Present-day lakes, wetlands, main surface water (stream) runoff and groundwater chemistry were loosely used as "calibration targets" for the modelled evolution of the hydrological and hydro-chemical conditions during Holocene time (Figure 4-6). The simulated conditions at 2000 AD were used as reference for the identification of disturbances caused by the subsequent flow modelling of the excavation and operation phases.
- The location and geometry of a final repository at Laxemar was imported from /SKB 2007/ (Figure 1-2 and Figure 4-7).
- Five scenarios (operational stages A–E) of the repository development were studied, i.e. not all parts of the repository were in operation (depressurised) at the same time (Figure 1-2).
- Six levels of grouting efficiency, I–VI, were studied for each operation stage A–E (Table 4-3).
- For the modelling of the saturation process following the closure of the operational phase, the backfill material was assumed to have hydraulic properties similar to Friedland Clay /Börgesson et al. 2006/.
- Two thresholds of the inflow rate to any deposition hole were analysed as a means to quantify the effect of using hydraulic criteria for rejecting a deposition hole:
  Q1: Deposition hole inflow is greater than 0.1 L/min.
  Q2: Deposition hole inflow is greater than 1% of the total inflow to the deposition tunnel (including its deposition holes).

The two inflow rate criteria were analysed alone and in combination with two geometry-based fracture rejection criteria, referred to as FPC (full perimeter criterion) and EFPC (expanded FPC), see Figure 4-8 and Figure 4-9. In summary, the following four variants of deposition hole rejection criteria were analysed:

I. {Q1}

II. {Q2}

III. {Q1 ∪ Q2}

IV. {Q1 ∪ Q2} | exclusion of {FPC ∪ EFPC}

The prioritised variants of the scenario analyses carried out for SR-Site are number III and number IV. Variant III looks at the combination of criteria Q1 and Q2 and Variant IV looks at the combination of criteria Q1 and Q2 after all deposition hole positions that fail the combination of criteria FPC and EFPC have been excluded.

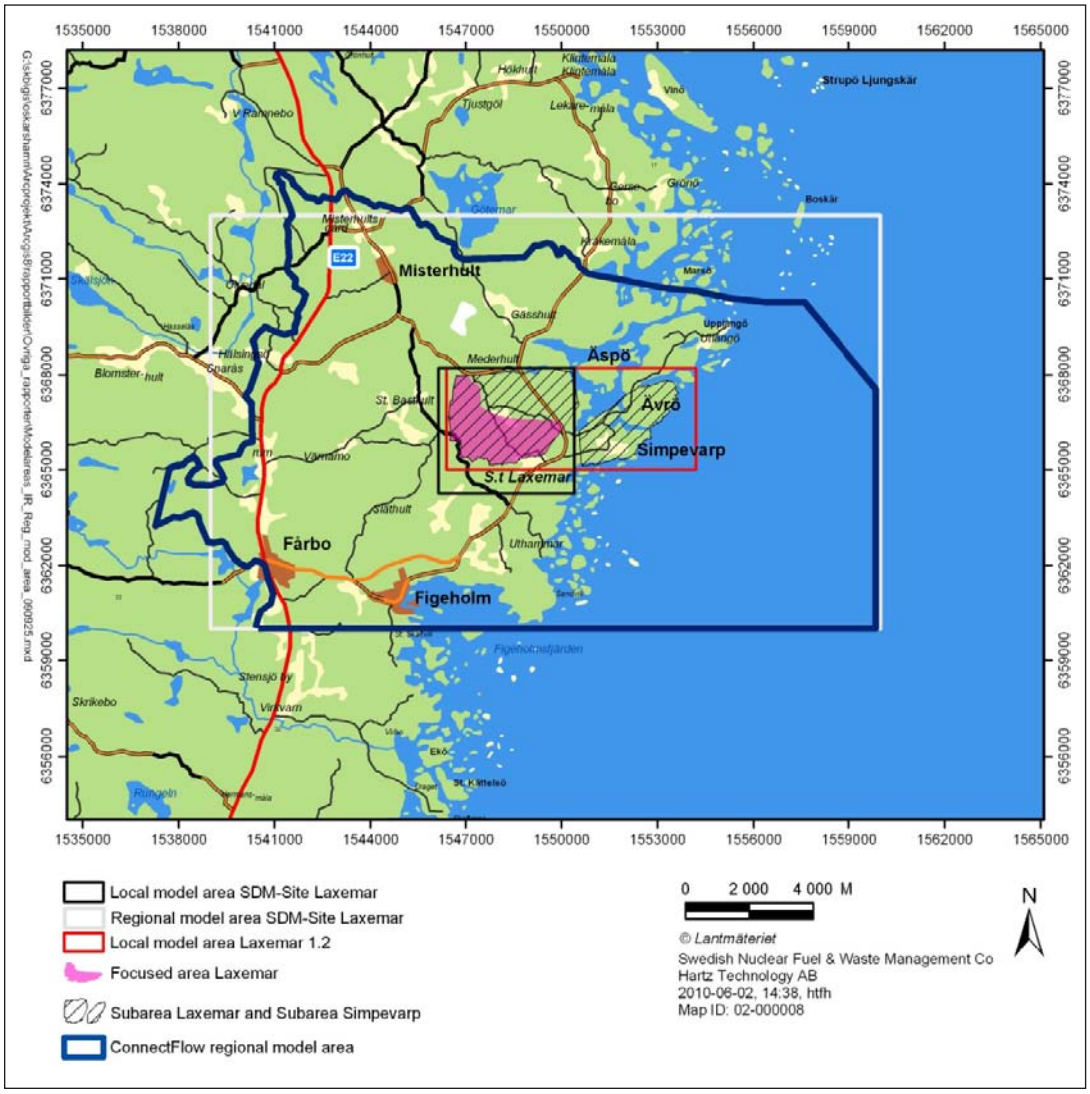

Figure 4-1. *Various model areas used for SDM-Site Laxemar. The regional model domain is shown by the blue line. This is also the limit of the model domain used in this study.*

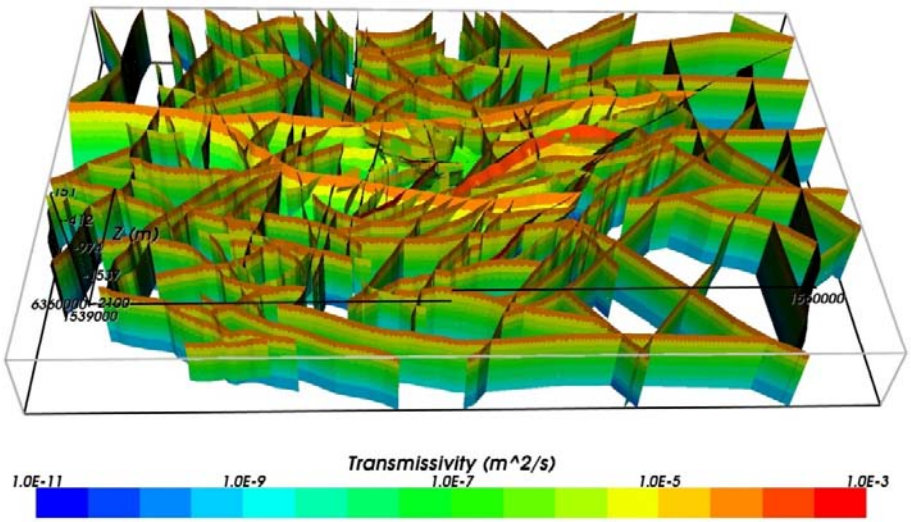

Figure 4-2. *All HCDs and their inferred depth dependent transmissivity for the deterministic SDM-Site base case model. Oblique view looking from the south. /Rhén and Hartley 2009/.*

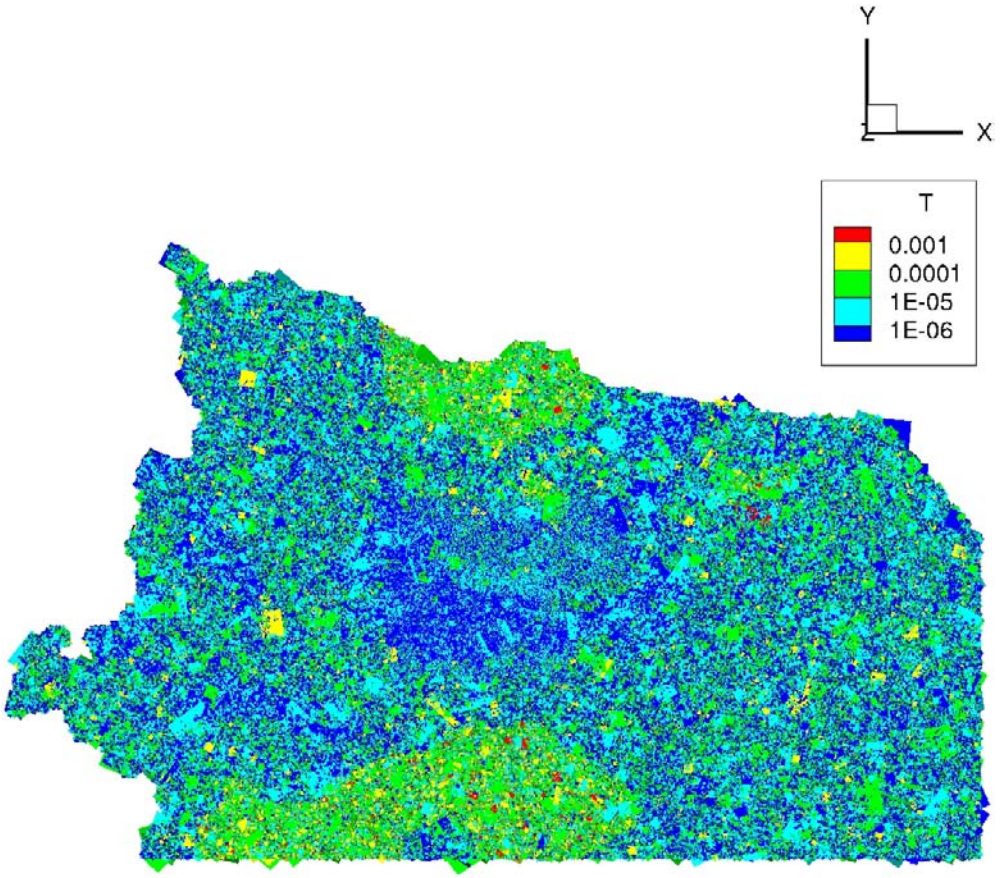

Figure 4-3. *Horizontal view of the studied stochastic fracture network realisation representing the Elaborated Hydro-DFN model coloured by transmissivity, T (m^2/s).*

Table 4-1. Grid cell hydraulic properties applied in this work for the uppermost 20 m of the model domain and the minimum values allowed below this depth.

Property	Depth interval	Value
Hydraulic conductivity K_c [m/s]	**< 20 m**	$K_{c,h} = \max \begin{cases} 1 \cdot 10^{-7} \\ 5 \cdot 10^{-3}\, 10^{-Depth/3} \end{cases}$ $K_{c,v} = 1 \cdot 10^{-6}$
	≥ 20 m	$K_{c,h} \geq 1 \cdot 10^{-10}$ $K_{c,v} \geq 1 \cdot 10^{-10}$
Kinematic porosity ϕ_c [–]	**< 20 m**	$\phi_c = \max \begin{cases} 1 \cdot 10^{-3} \\ 5 \cdot 10^{-2}\, 10^{-Depth/20} \end{cases}$
	≥ 20 m	$\phi_c = 5 \cdot \max \begin{cases} 1 \cdot 10^{-5} \\ f(\phi_f); \phi_f = (0.46 \sqrt{T_f}) / b_f \end{cases}^*$ T_f = fracture transmissivity b_f = fracture thickness
Specific storage S_s [m^{-1}]	**≥ 0 m**	$S_s = 1 \cdot 10^{-9}$

* The grid cell kinematic porosity was increased by five times to compensate for a reduced pore space due to the usage of a size-truncated Hydro-DFN model.

Table 4-2. Assumed initial conditions at 8000 BC at Laxemar /Selroos and Follin 2010/.

Depth interval	Initial salinity
Ground surface to –150 m	0%
–150 m to –2,100 m	Linearly increasing to 7.2%

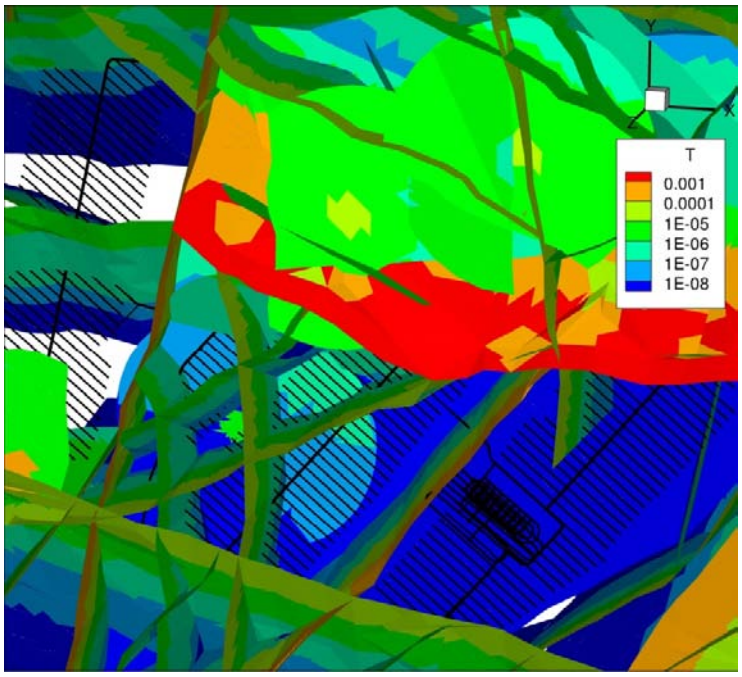

Figure 4-4. *Example view of the repository layout at –505 m elevation and some of the deterministically modelled deformation zones. In the Elaborated Hydro-DFN, the deformation zones have homogeneous hydraulic properties with depth dependency according to Equation (2-1). (Some zones are deleted in this visualisation for the sake of visibility).*

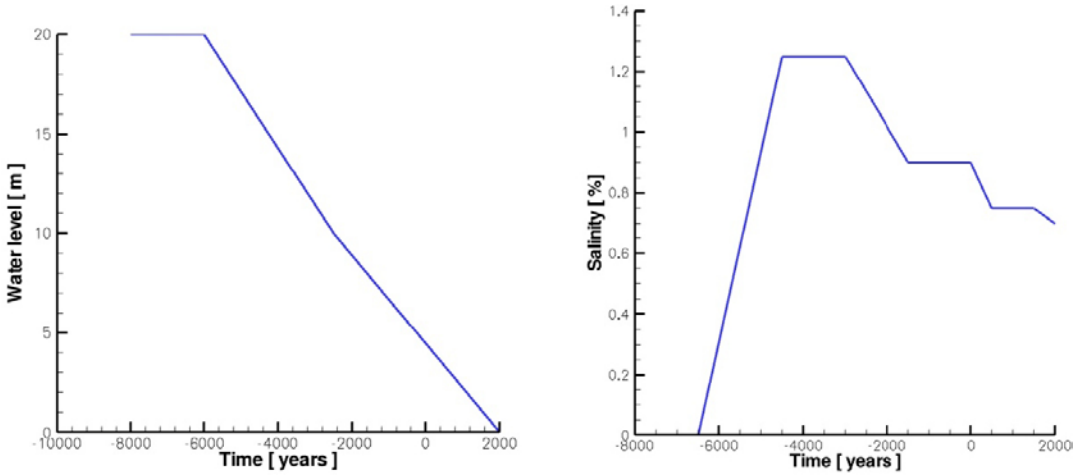

Figure 4-5. *Evolution of the shoreline displacement and the salinity of the Baltic Sea close to Laxemar during Holocene time (8000 BC to 2000 AD). (Modified after Figure 4-6 and Figure 4-7 in /Joyce et al. 2010/.)*

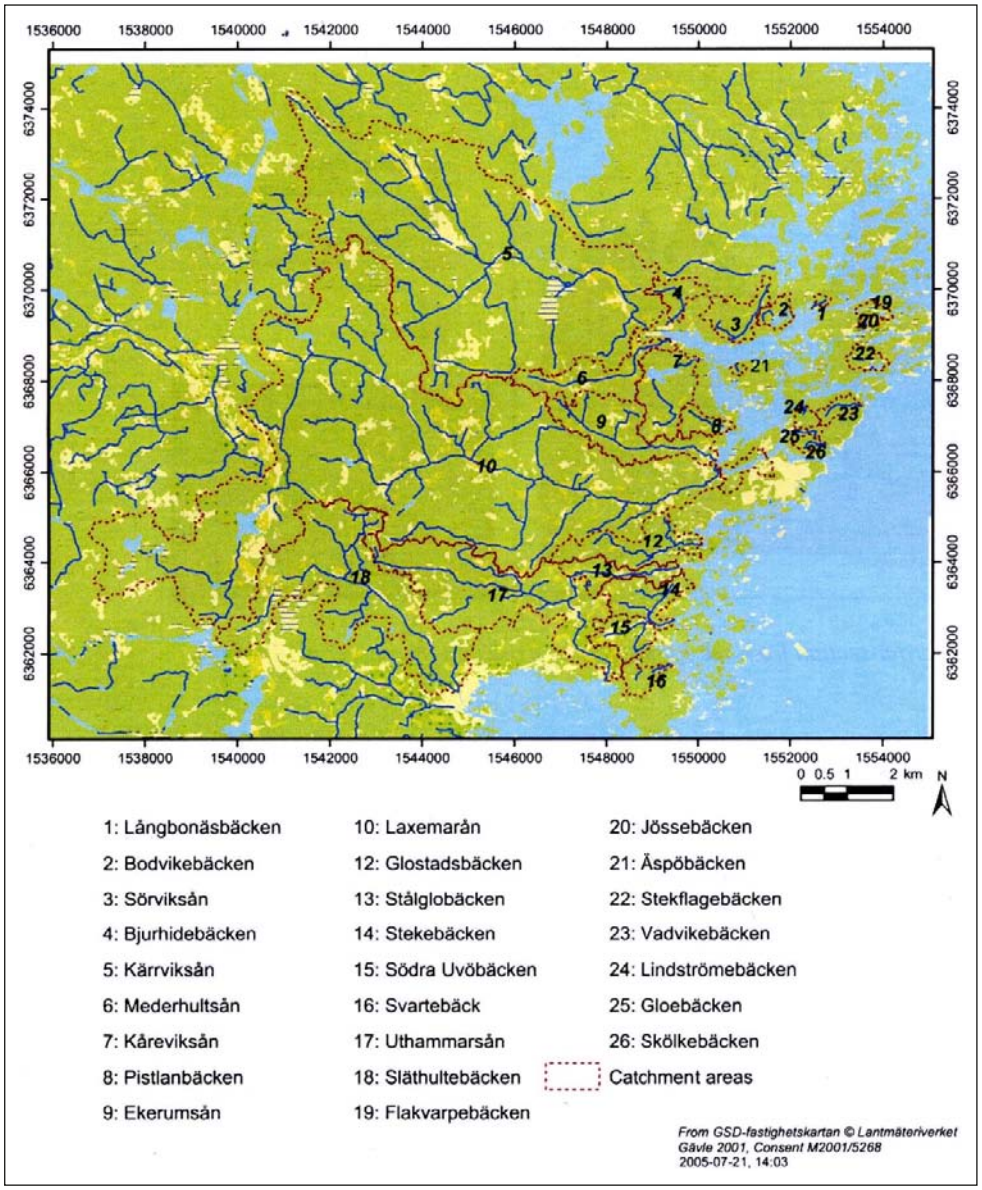

Figure 4-6. *Location of major streams, major lakes (blue areas) and wetlands (white coloured areas) in the Laxemar area. /Werner 2009/.*

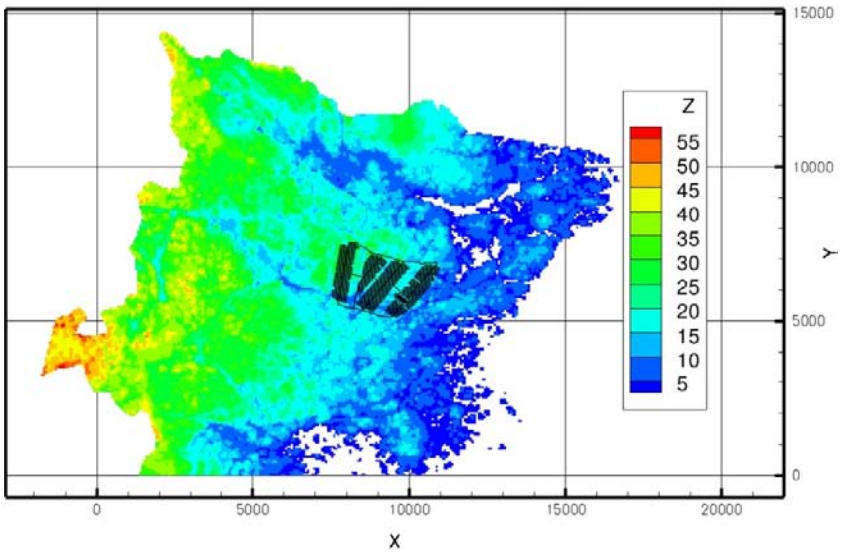

Figure 4-7. *Plan view of the ground elevation and the suggested location of a final repository at Laxemar in local DarcyTools coordinates. The values shown in the legend are expressed in m RHB 70. The origin of the local coordinate system is placed at Easting: 1,539,000 and Northing: 6,360,000 with regard to the national 2.5 gon W 0:-15, RT 90 coordinates ("RAK system"). The y-axis in the local coordinate system points towards north.*

Table 4-3. Definition of the studied levels of grouting efficiency. A cell size of 4 m is used for cells in contact with the repository.

Grouting level	Criteria
I	The conductivity for all cells in contact with the repository has a maximum value of 10^{-7} m/s.
II	As for level I, but maximum conductivity 10^{-8} m/s.
III	All structures are grouted to a hydraulic conductivity of K = $1 \cdot 10^{-9}$ m/s, with the exception of main and transport tunnels, as well as shafts, which are grouted to a hydraulic conductivity K = $1 \cdot 10^{-8}$ m/s.
IV	All structures are grouted to a hydraulic conductivity of K = $1 \cdot 10^{-10}$ m/s, with the exception of main and transport tunnels, as well as shafts, which are grouted to a hydraulic conductivity K = $1 \cdot 10^{-8}$ m/s.
V	As for level I, but maximum conductivity 10^{-9} m/s.
VI	All structures are grouted to a hydraulic conductivity of K = $1 \cdot 10^{-10}$ m/s, with the exception of main and transport tunnels, as well as shafts, which are grouted to a hydraulic conductivity K = $1 \cdot 10^{-9}$ m/s.

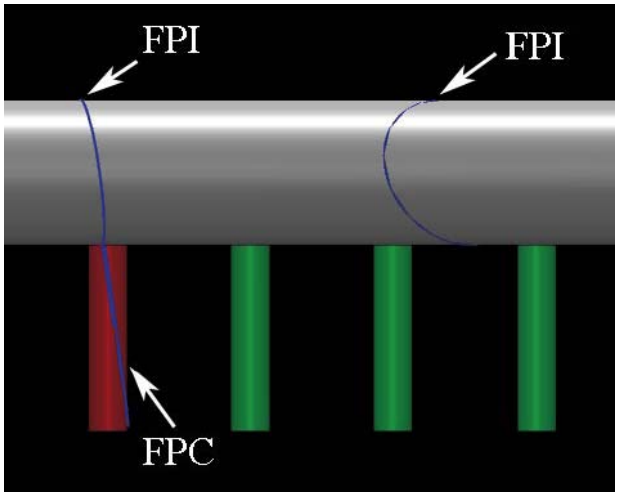

Figure 4-8. *Definition of FPI (Full Perimeter Intersection) and FPC (Full Perimeter Criterion). The FPI mapped in the deposition tunnel is judged to represent the trace of a discriminating fracture, FPC, if its projection intersects the deposition hole. (Figure 5-1 in /Munier 2006/.)*

Figure 4-9. *Definition of EFPC (Expanded Full Perimeter Criterion). A potentially discriminating fracture can remain undetected despite the use of the FPC in the deposition tunnel. (Figure 5-2 in /Munier 2006/.)*

4.3 Sensitivity study

Three cases are used as a means to study the sensitivity of the inflow rates to variations in the geometrical and hydraulic properties other than the impact of different levels of grouting efficiency.

1. The number of possible deposition holes was reduced by honouring the union probability of the FPC and EFPC criteria (Figure 4-10).
2. A single deposition tunnel (Figure 4-11).
3. No salinity (fresh water groundwater flow).

It was not feasible to carry out the sensitivity study for all operational stages and grouting levels. For the sake of simplicity, we therefore used a modified setup of the Elaborated Hydro-DFN model as a reference.

- All construction parts of the repository layout were held open at the same time.
- The grouting efficiency was fixed to level II (see Table 4-3).

Figure 4-10. *Plane view of the first variant and sensitivity test. The view shows the repository layout with the rejected deposition holes for the first realisation of the underlying Hydro-DFN model shown as dots. Out of a total of 8,031 possible deposition holes, 717 deposition holes were rejected prior to the flow simulation based on the union probability of the FPC and EFPC criteria {FPC ∪ EFPC}. The y-axis points towards north. The rejected holes were modelled as "not drilled".*

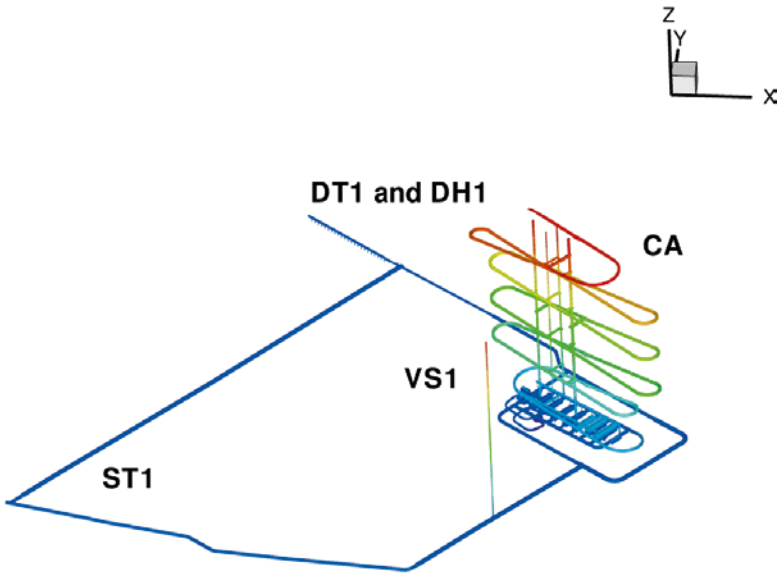

CA = Central area
ST = Main & Transport tunnel
DT = Deposition tunnel
DH = Deposition Holes
VS = Ventilation shaft

Figure 4-11. *Visualisation of the second variant; a single deposition tunnel. The y-axis points towards north.*

4.4 Grid setup and grid cell hydraulic properties

The discretisation of the computational grid was refined in the vicinity of the repository in order to resolve the repository layout and to study the effects of grouting. The largest cell size away from the repository was 128 m (Figure 4-12 and Figure 4-13) and in the proximity of the repository the cell size was 4 m (Figure 4-14). This high resolution was needed to resolve the deposition tunnels, which have a height of 4.8 m and width of 4.2 m. A vertical cross-section through the repository is shown in Figure 4-15. The vertical resolution of the cells close to the top boundary was 2 m. In total about 2.1 million cells were used to model the problem as outlined. The origin of the local grid horizontal coordinates was positioned at (Easting, Northing) = (1,539,000 and 6,360,000).

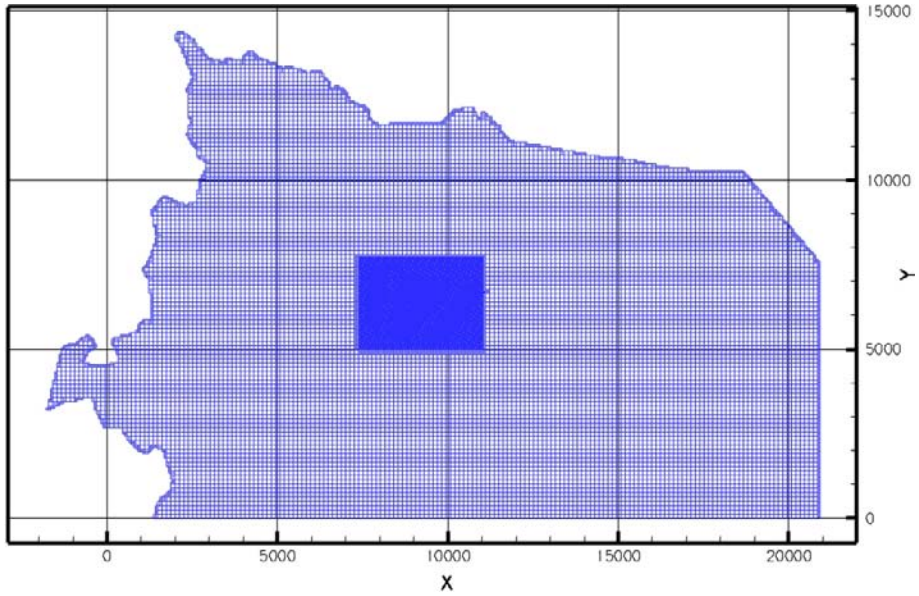

Figure 4-12. *Plane view of the model area and the computational grid at –505 m elevation. The size of the largest grid cells was 128 m. Within an area of about 3.5 km times 2.5 km around the repository the grid size was refined using an unstructured grid. The y-axis points towards north.*

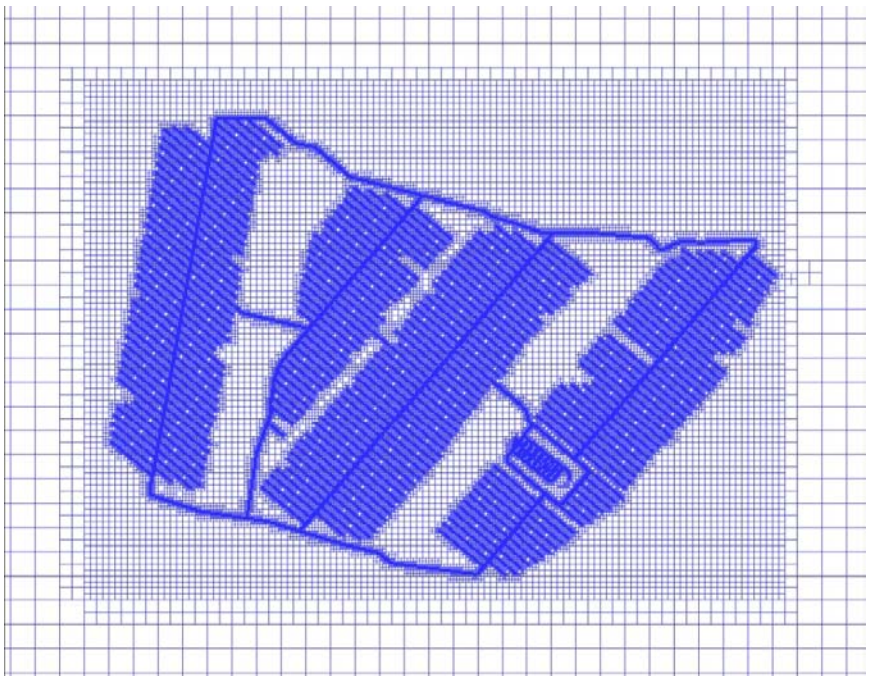

Figure 4-13. *Plane view of the computational grid at –505 m elevation. The discretisation around the repository was refined using an unstructured grid.*

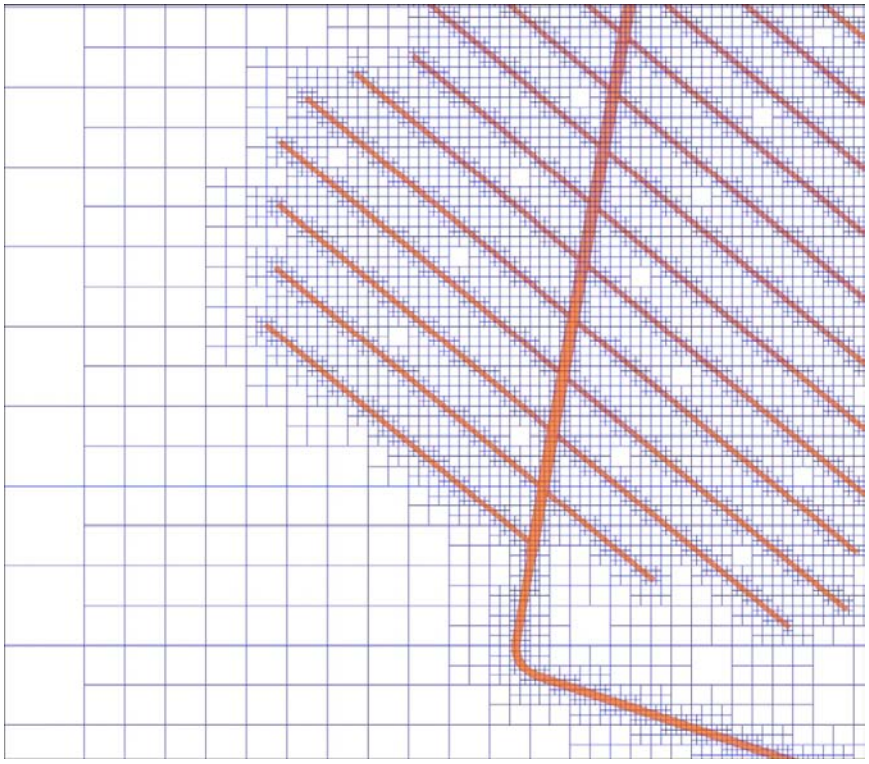

Figure 4-14. *Enlargement showing the discretisation of the eastern corner of the repository. The size of the smallest grid cells was 4 m.*

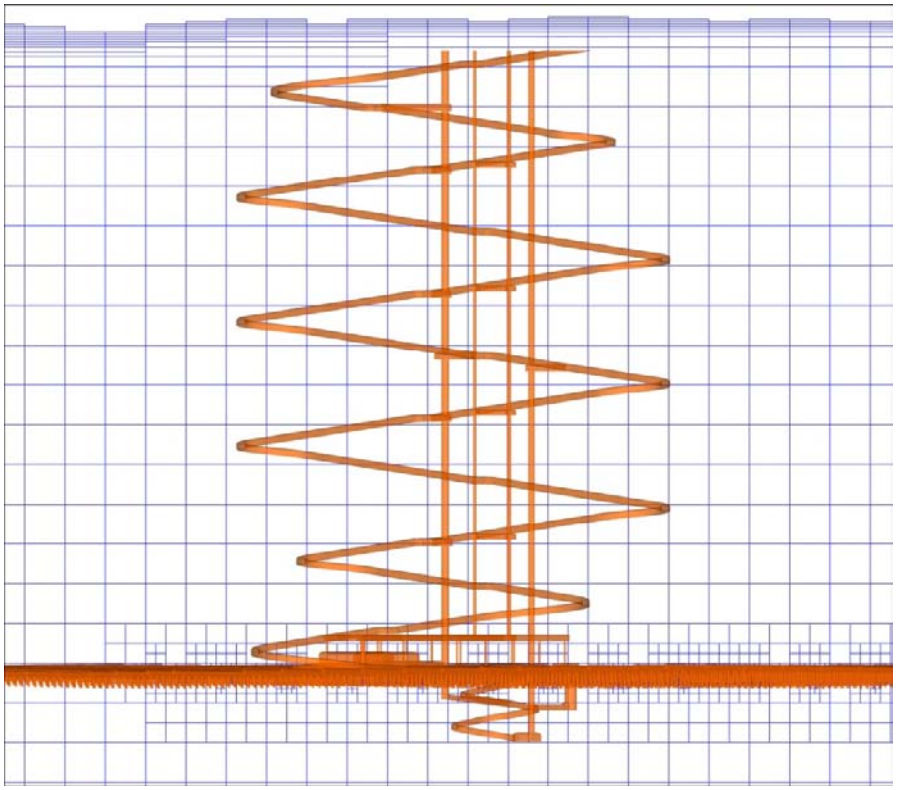

Figure 4-15. *Vertical cross-section (South-North) through the simulated repository.*

The vertical permeability field around the repository as implemented in the Elaborated Hydro-DFN model groundwater flow realisation is illustrated by two perpendicular vertical cross-sections and a horizontal plane at –505 m elevation in Figure 4-16. (It is recalled that the structural-hydraulic properties of the discrete features behind the Elaborated Hydro-DFN model realisation were imported from the temperate modelling work conducted by /Joyce et al. 2010/.) The horizontal permability fields are very similar to the vertical one and for this reason not shown.

Figure 4-17 and Figure 4-18 show horizontal close up views of the grid cell vertical permeability and kinematic porosity around the repository. The horizontal dimensions of the two views shown in Figure 4-17 and Figure 4-18 are approximately 2.5 km by 3.5 km. In Figure 4-19, the view in Figure 4-18 is accompanied by two other horizontal close up views of the grid cell kinematic porosity; –300 m and –600 m. Note that the repository layout is inserted in the views above and below repository depth in order to facilitate the reading.

The areas with high kinematic porosity in Figure 4-19 are of course due to the deformation zones. The repository is located to avoid direct contact with these as seen in the view at –505 m.

There is a clear depth trend in the vertical permeability, see Figure 4-16. This suggests that the changes in the groundwater chemistry at repository depth due to the excavation and operational phases will be more influenced by percolating shallow fresh and/or brackish water than by upconing of deep saline water.

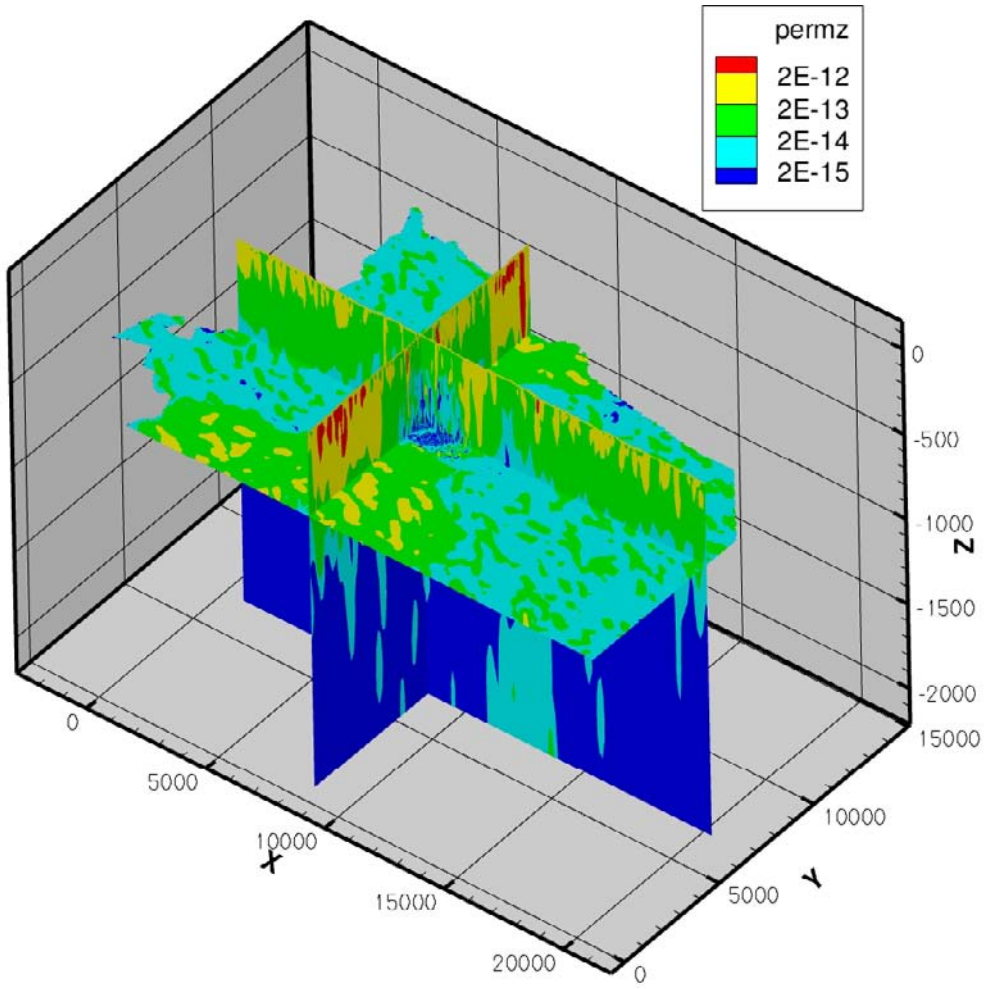

Figure 4-16. *The vertical permeability field around the repository illustrated by two perpendicular vertical cross-sections and a horizontal plane at –505 m elevation.*

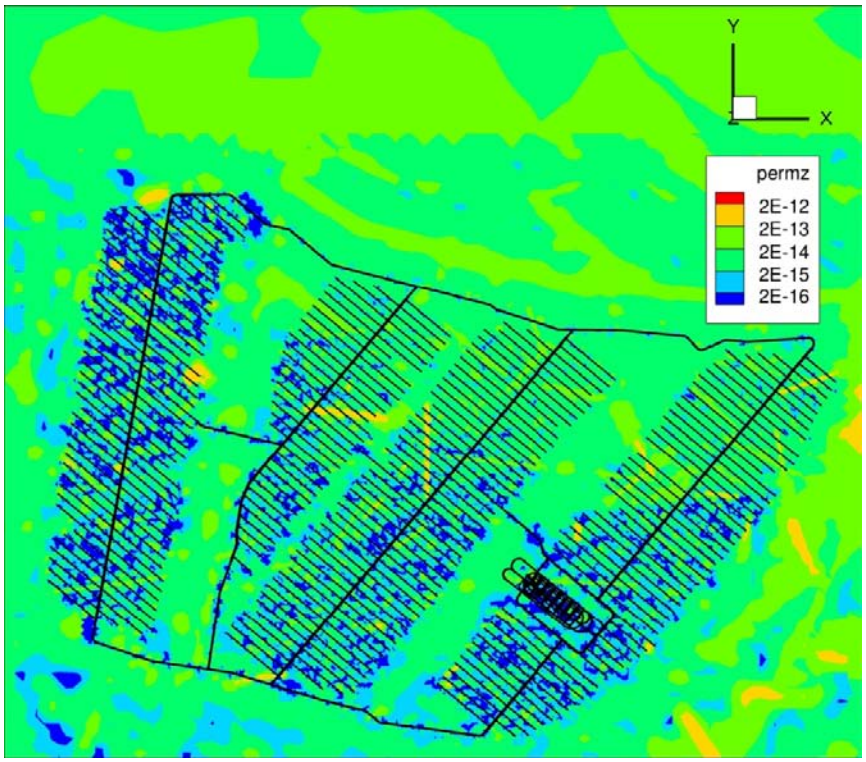

Figure 4-17. *Plane view of the grid cell vertical permeability field in the target area at –505 m elevation.*

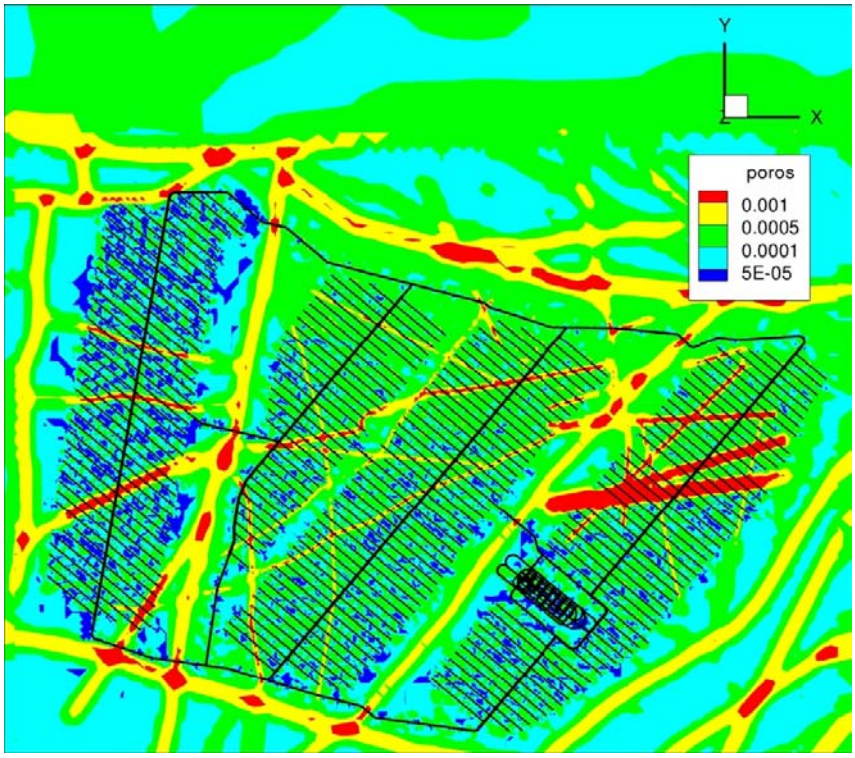

Figure 4-18. *Plane view of the grid cell kinematic porosity field in the target area at –505 m elevation.*

Elevation
–300 m

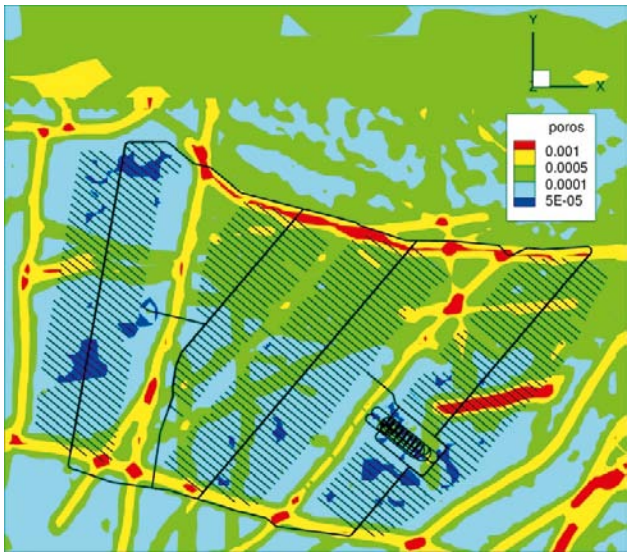

Elevation
–505 m
(repository depth)

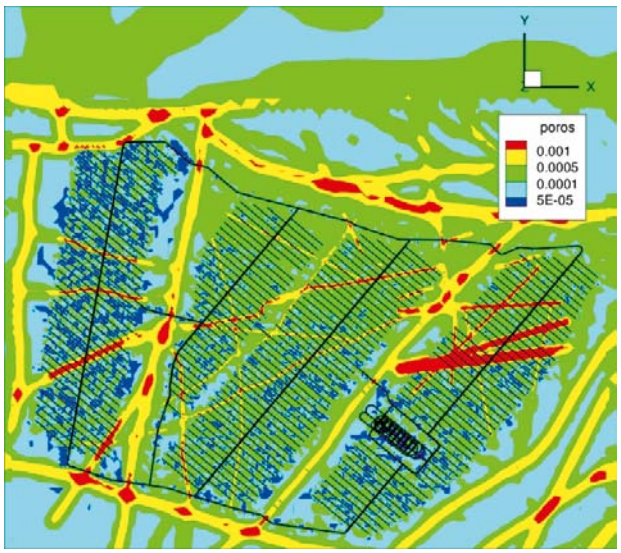

Elevation
–600 m

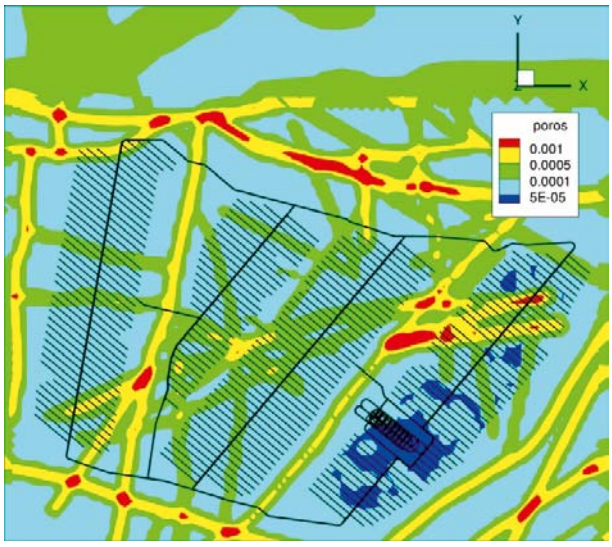

Figure 4-19. *Horizontal close up views of the grid cell kinematic porosity at three elevations; –300 m, –505 m and –600 m. The repository layout is inserted in the views above and below repository depth (–505 m elevation) in order to facilitate the reading.*

Figure 4-20 and Figure 4-21 show cumulative distribution functions (CDFs) of k_c and ϕ_c at –505 m elevation for a regular 4 m lattice within a subarea of (2 km)^2 centred on the two views shown in Figure 4-17 and Figure 4-18. The two CDF plots reveal that the kinematic porosity varies between $5 \cdot 10^{-5}$ and $2.0 \cdot 10^{-3}$, whereas the vertical permeability varies between $2 \cdot 10^{-17}$ m^2 ($K_{c,v} \approx 1 \cdot 10^{-10}$ m/s) and $2.0 \cdot 10^{-12}$ m^2 ($K_{c,v} \approx 10^{-5}$ m/s). Another representation of these data is shown in Figure 4-22. Here, it is found that a certain correlation between the two variables exists, but we also see that the scatter (uncertainty) is significant.

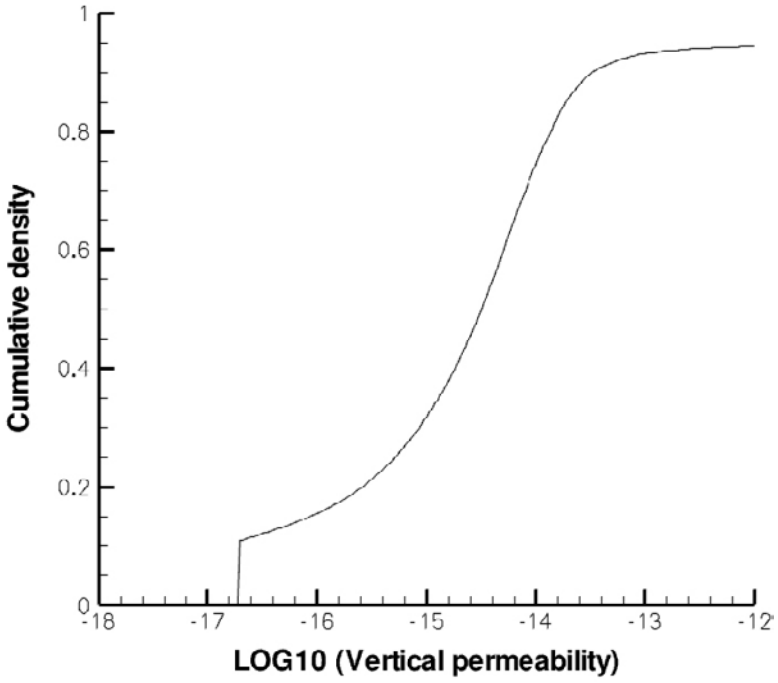

Figure 4-20. *Cumulative density function plot of k_c for all 4 m grid cells values within a subarea of (2 km)^2 centred on the view shown in Figure 4-17.*

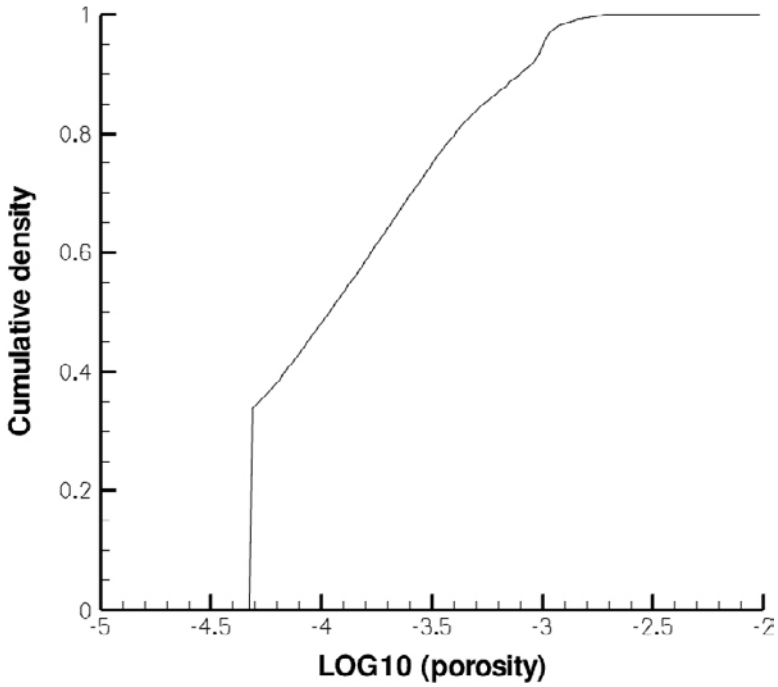

Figure 4-21. *Cumulative density function plot of ϕ_c for all 4 m grid cells values within a subarea of (2 km)^2 centred on the view shown in Figure 4-18.*

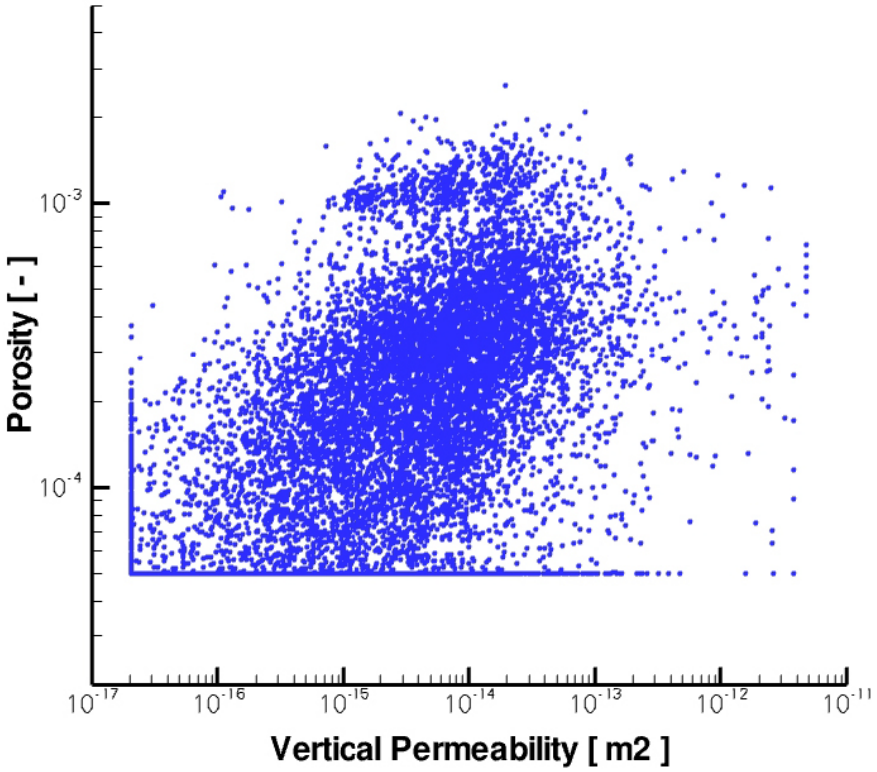

Figure 4-22. *Scatter plot of the kinematic porosity data and the vertical permeability data shown in Figure 4-17 and Figure 4-18.*

4.5 Scoping calculation of the total inflow rate and drawdown

Preliminary simulations indicate that the inflow rates to the open repository may be several hundreds of L/s. Such inflows will create both engineering and environmental problems and it is for this reason important to establish if the simulation results are realistic. Therefore, some scoping calculations of the total inflow and the corresponding drawdown are presented in Appendix D. It is found that the present conditions, i.e. the grouting levels and the mean conductivity of the rock, will result in large inflows and drawdowns.

5 Results

5.1 Comparison with natural conditions

Present-day lakes and wetlands, surface water (stream) runoff, and groundwater chemistry were loosely used as "calibration targets" for the modelled evolution of the hydrological and hydrochemical conditions during Holocene time. For the sake of the work reported here, the surface topography was resolved by a cell size of 64 m and potential streams of all dimensions by a cell size of 32 m (Figure 5-1).

Figure 5-2 shows the simulated saturation level close to ground surface at present day. Areas with a predicted groundwater table (hydraulic head) above ground surface are marked blue, whereas areas with a predicted groundwater table below, but very close, ground surface are marked green. The latter may be perceived as wetlands, cf. Figure 4-6. Figure 5-3 shows the simulated flow vectors. In the streams Laxemarån and Kärrviksån, see Figure 4-6, the flow rates were calculated to around 100–150 L/s. Field data indicate that the flow in these streams is very irregular, but the magnitudes seem to be in agreement with the present estimates; present simulations are based on the average annual precipitation.

Figure 5-4 shows the simulated salinities at 2000 AD in per cent by weight at –505 m elevation. Measured salinities in the Laxemar area are shown in Figure 5-5. As 1% salinity corresponds approximately to 10,000 mg/L, we find that a certain agreement between simulated and measured salinities is found .

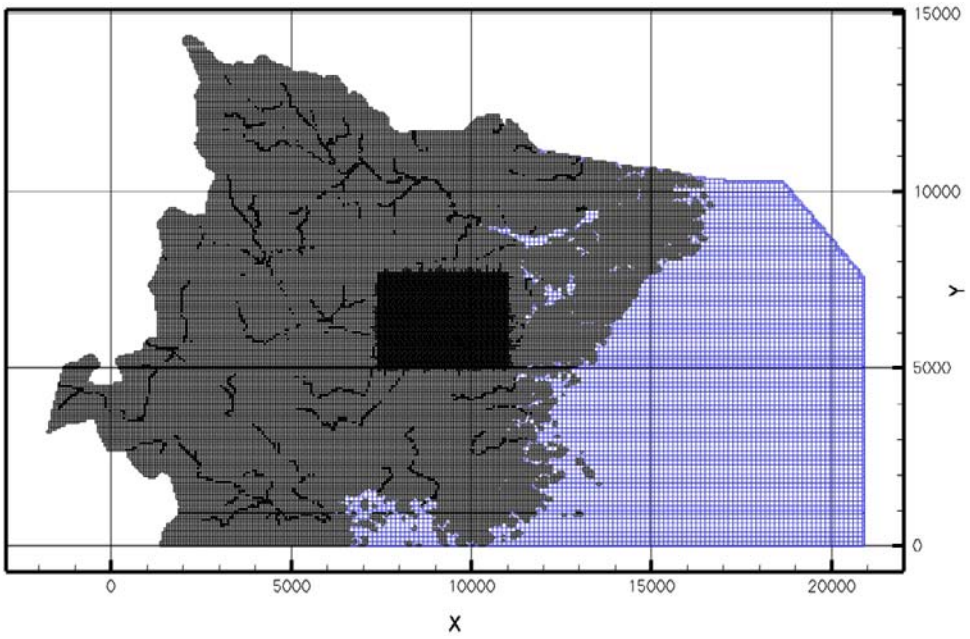

Figure 5-1. *The surface topography was resolved by a cell size of 64 m and potential streams by a cell size of 32 m. The latter are indicated as black lines. The "stream cells" were assigned a hydraulic conductivity of 2.0 m/s.*

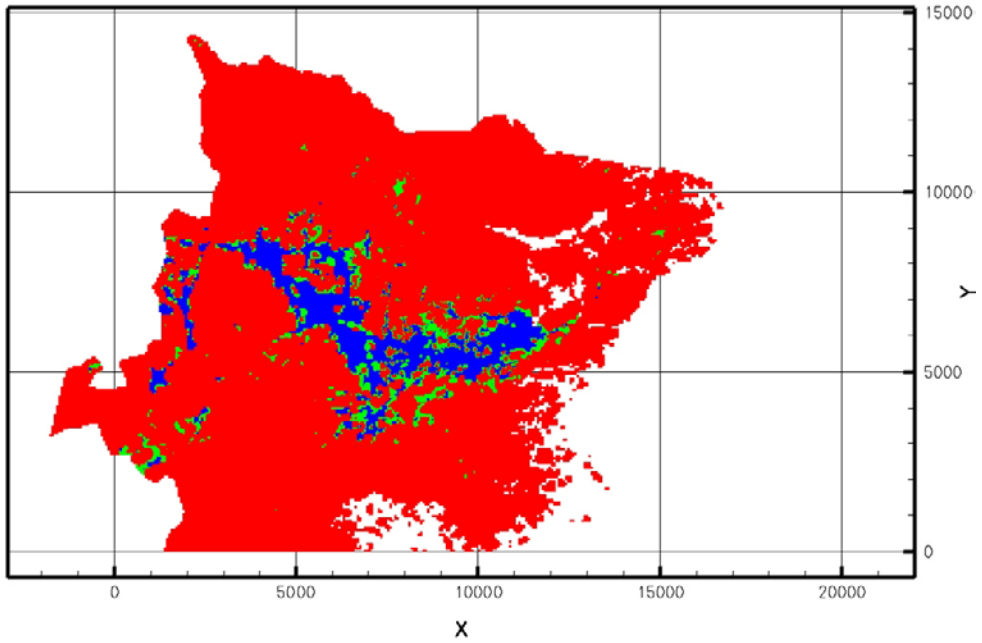

Figure 5-2. *Areas with a predicted groundwater table (hydraulic head) above ground surface are marked blue, whereas areas with a predicted groundwater table below, but very close, ground surface are marked green. The latter may be perceived as wetlands, cf. Figure 4-6. In the red areas the groundwater table is significantly below the ground surface.*

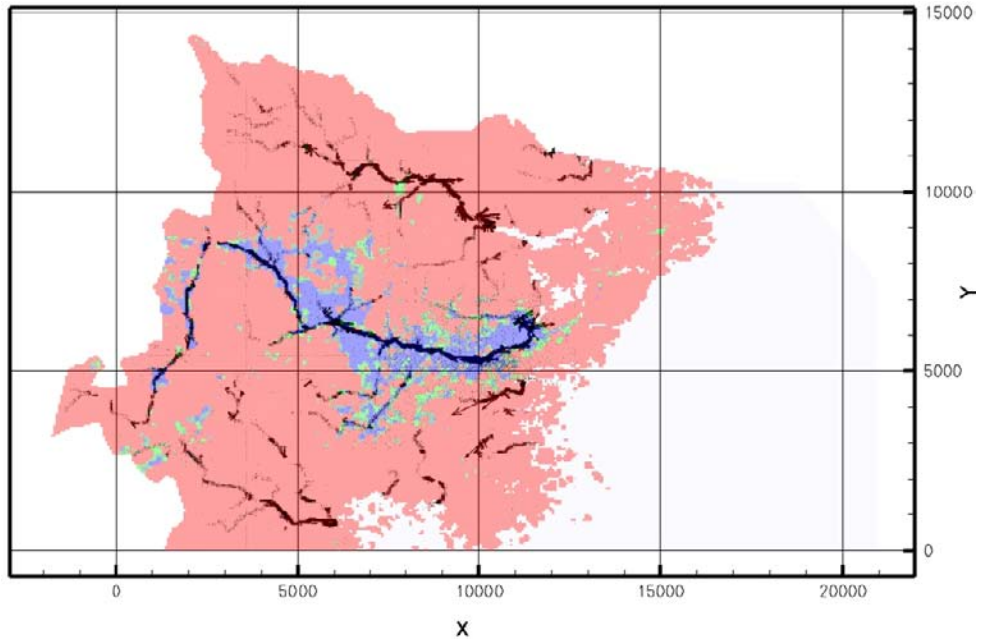

Figure 5-3. *Flow vectors. The two major streams are Kärrviksån and Laxemarån, cf. Figure 4-6. Saturation level shown as transparent contours (otherwise same as in Figure 5-2).*

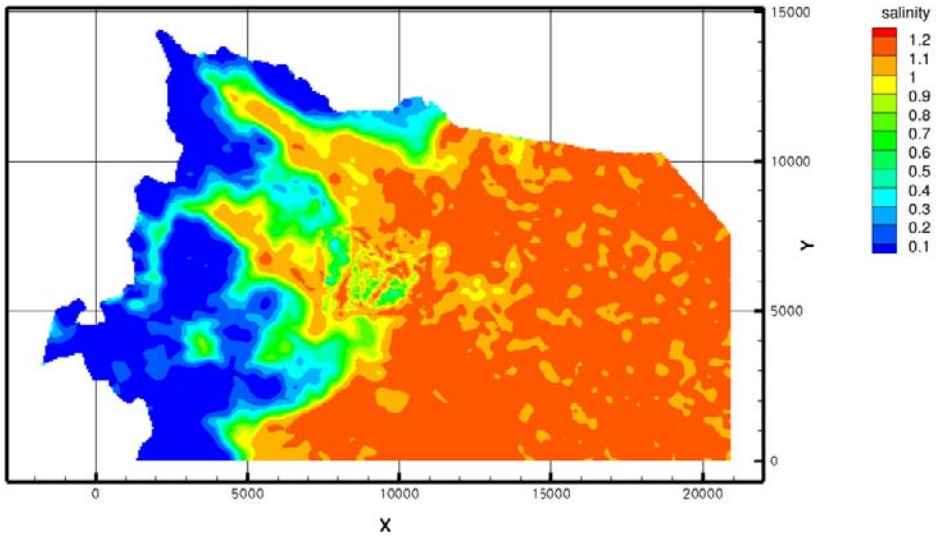

Figure 5-4. *Simulated salinities 2000 AD in per cent by weight at –505 m elevation. A salinity of 0.1% by weight corresponds approximately to 1g/L of TDS, cf. Equation (3-7).*

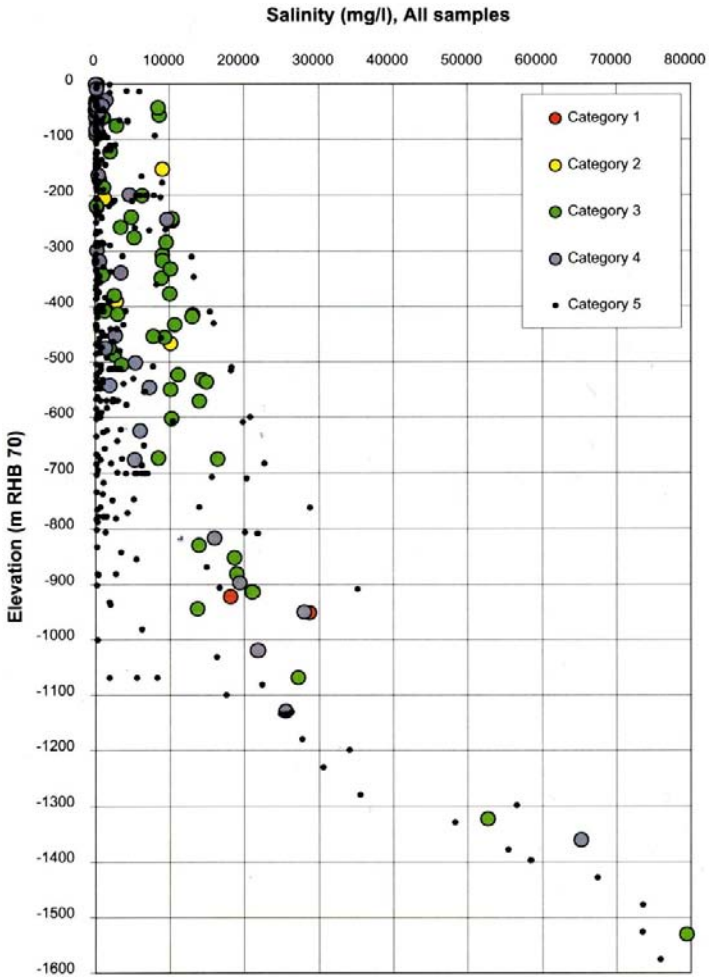

Figure 5-5. *Measured salinities in the Laxemar area /Rhén et al. 2009/. The categories refer to the quality of data, with category 1 being of highest quality.*

5.2 Grouting efficiency

5.2.1 Inflow calculations

The inflow simulations during the excavation and operational phases were done for five operation ×2 stages A–E (Figure 1-2) and six levels of grouting efficiency I–VI (Table 4-3). Table 5-1 summarises the calculated inflows to the different parts of a repository at Laxemar. The total inflow varied in the range 10 to 452 L/s (860 to 38,870 m^3/d), depending on which stage and level of grouting efficiency that is considered.

The five operation stages were run in sequence, where the first stage, A, lasted for 5 years, the second stage, B, lasted for 15 years, the third stage, C, lasted for 10 years, the fourth stage, D, lasted for 10 years and the fifth stage, E, lasted for 15 years, corresponding to a total operation time of 55 years.

It should be mentioned that for grouting levels one and two, operation stages four and five, the simulations were done with a ground water table that was fixed to the undisturbed level. The reason for this is that the drawdowns became greater than what could be handled by the numerical model. The approximation that this simplification introduces will be discussed below.

Figures 5-6 to 5-11 show the computational cells with an inflow greater than 0.1 L/min and 0.5 L/min, for the six grouting levels. Operation stage E is used throughout, as this stage gives the largest inflows.

There are two observations in the figures that need to be commented upon:

- The difference between main tunnels and deposition areas follows from the grouting levels assumed. Grouting level IV gives very small inflows in deposition areas, as one example. This is also confirmed by the pressure distribution for this case, see Figure 5-12; the ambient pressure advances far into the deposition areas. Grouting level II implies that the same efficiency is used for all parts of the repository. The pressure in the deposition areas then become more uniform, see Figure 5-12.
- A large number of cells are marked for the inflow criteria, indicating that the total inflow is high. This is also seen in Table 5-1.

Table 5-1. Inflow results in L/s to different parts of the repository, for five stages (A–E) and six grouting alternatives (I–VI) using the Elaborated Hydro-DFN model. The different parts of the repository are shown in Figure 1-2, the grouting levels are defined in Table 4-3 and the five stages are defined in Figure 1-2.

Part	Grouting Level																										
	I					II					III					IV					V					VI				
	A	B	C	D	E	A	B	C	D	E	A	B	C	D	E	A	B	C	D	E	A	B	C	D	E	A	B	C	D	E
CA	32	29	34	34	32	17	16	17	17	16	6	5	6	6	5	2	2	2	2	2	6	6	6	7	6	2	2	2	2	2
ST1	32	18	29	29	26	21	12	20	20	18	22	16	21	21	19	22	19	21	21	20	8	5	8	8	8	8	7	8	8	8
VS1	3	3	3	3	3	1	1	1	1	1	1	1	1	1	1	1	1	1	1	1	0	0	0	0	0	0	0	0	0	0
DT1	8					3					1					0					1					0				
DH1	2					1					0					0					0					0				
DT2		54					42					20					6					22					6			
DH2		17					13					8					3					8					3			
ST3			32	41	45			21	28	30			25	29	30			28	30	30			7	10	10			9	10	10
VS2			2	2	3			1	1	1			1	1	1			1	1	1			0	0	0			0	0	0
DT3			48					372					17					4					19					5		
DH3			13					11					6					2					7					2		
ST4				27	45				18	28				23	27				26	27				6	8				7	8
DT4				22					18					8					2					9					2	
DH4				75					55					21					4					24					5	
ST5					52					36					49					56					12					15
DT5					200					144					51					9					58					10
DH5					46					35					15					4					17					4
∑	77	121	161	233	452	43	84	108	158	309	30	50	77	110	198	25	31	59	87	150	15	41	47	64	119	10	18	26	34	57

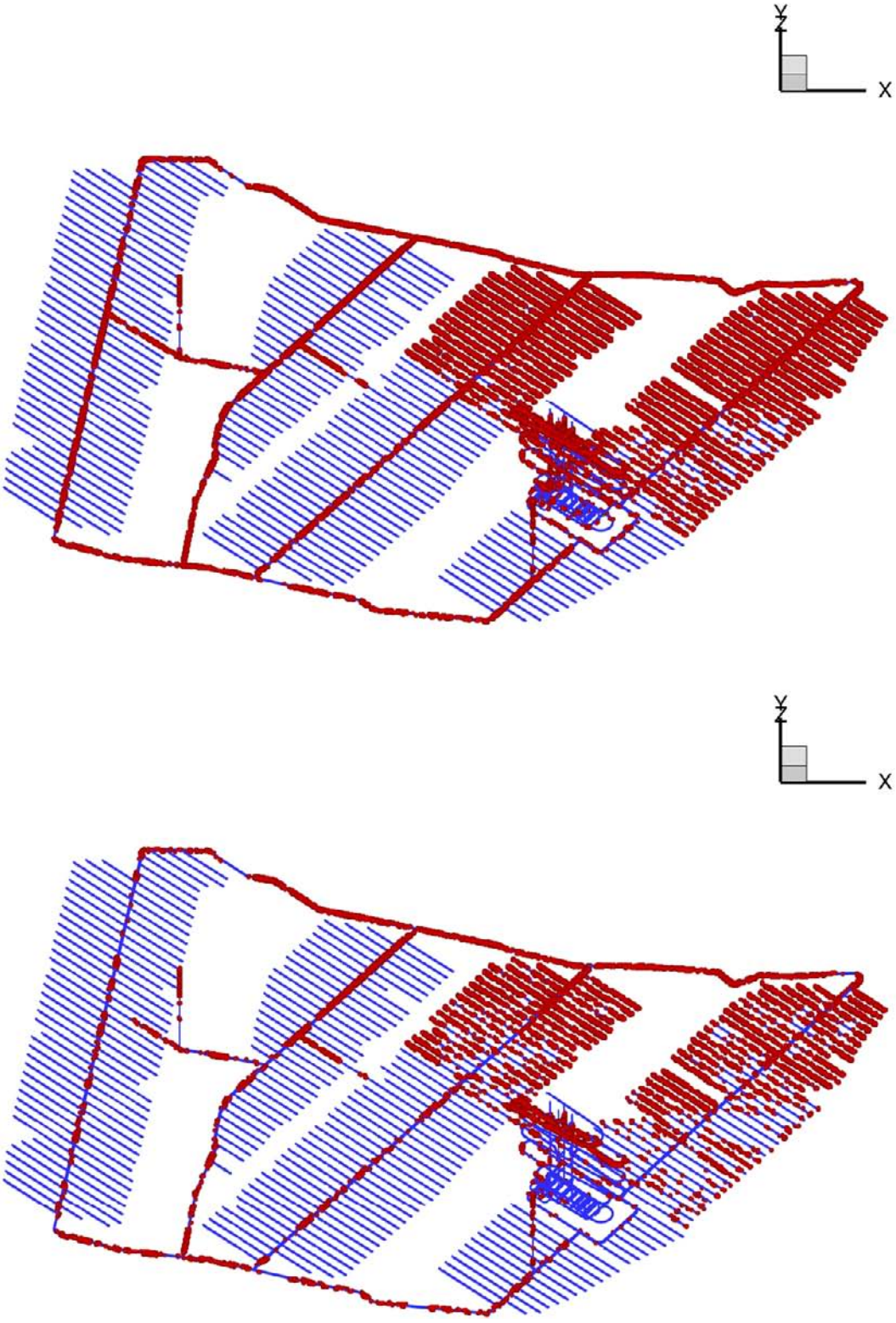

Figure 5-6. *Cells with an inflow rate greater than 0.1 L/min (top) and 0.5 L/min (bottom) are marked up by spheres. Operation stage E and grouting level I.*

Figure 5-7. *Cells with an inflow rate greater than 0.1 L/min (top) and 0.5 L/min (bottom) are marked up by spheres. Operation stage E and grouting level II.*

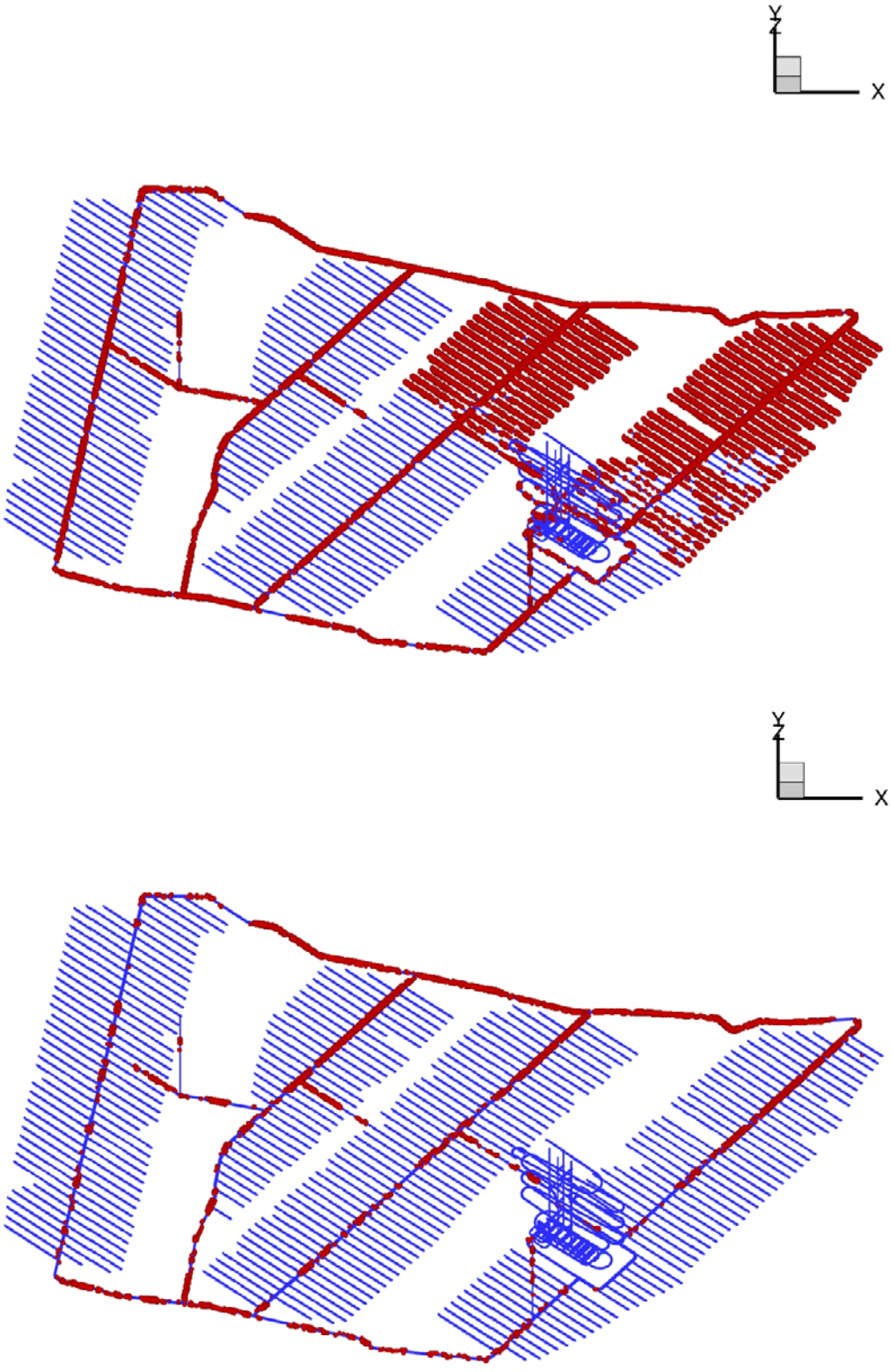

Figure 5-8. *Cells with an inflow rate greater than 0.1 L/min (top) and 0.5 L/min (bottom) are marked up by spheres. Operation stage E and grouting level III.*

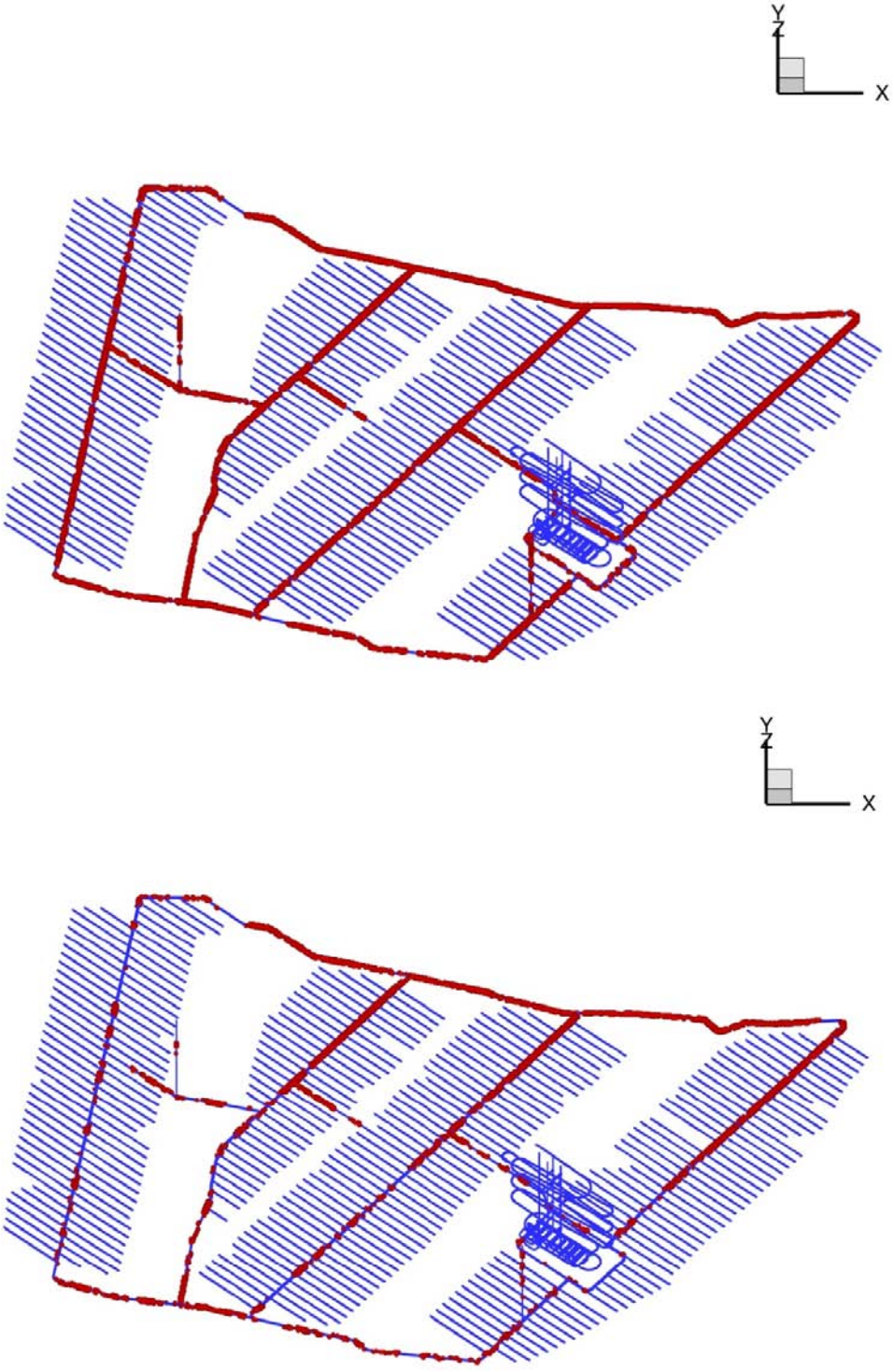

Figure 5-9. *Cells with an inflow rate greater than 0.1 L/min (top) and 0.5 L/min (bottom) are marked up by spheres. Operation stage E and grouting level IV.*

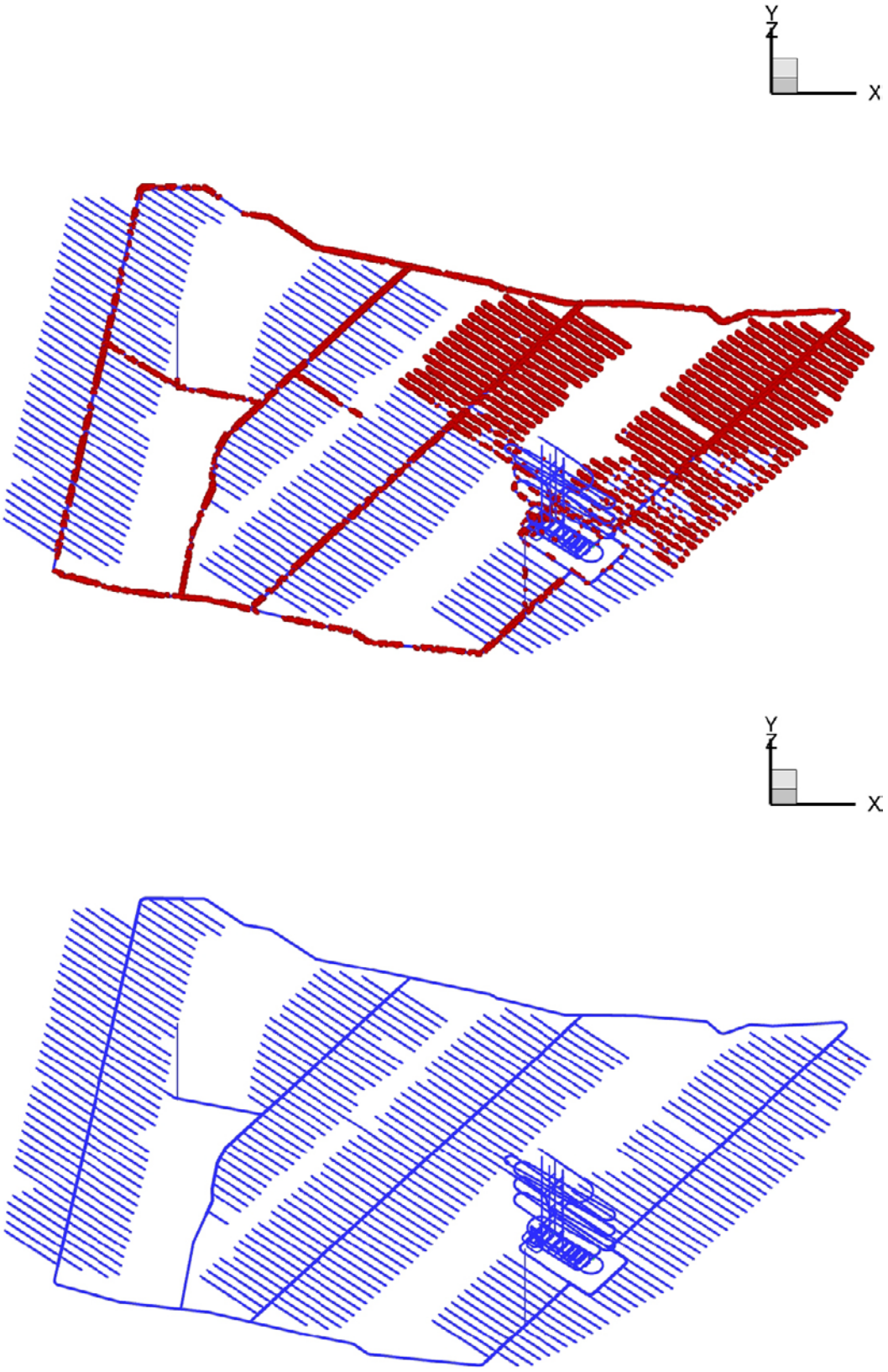

Figure 5-10. *Cells with an inflow rate greater than 0.1 L/min (top) and 0.5 L/min (bottom) are marked up by spheres. Operation stage E and grouting level V.*

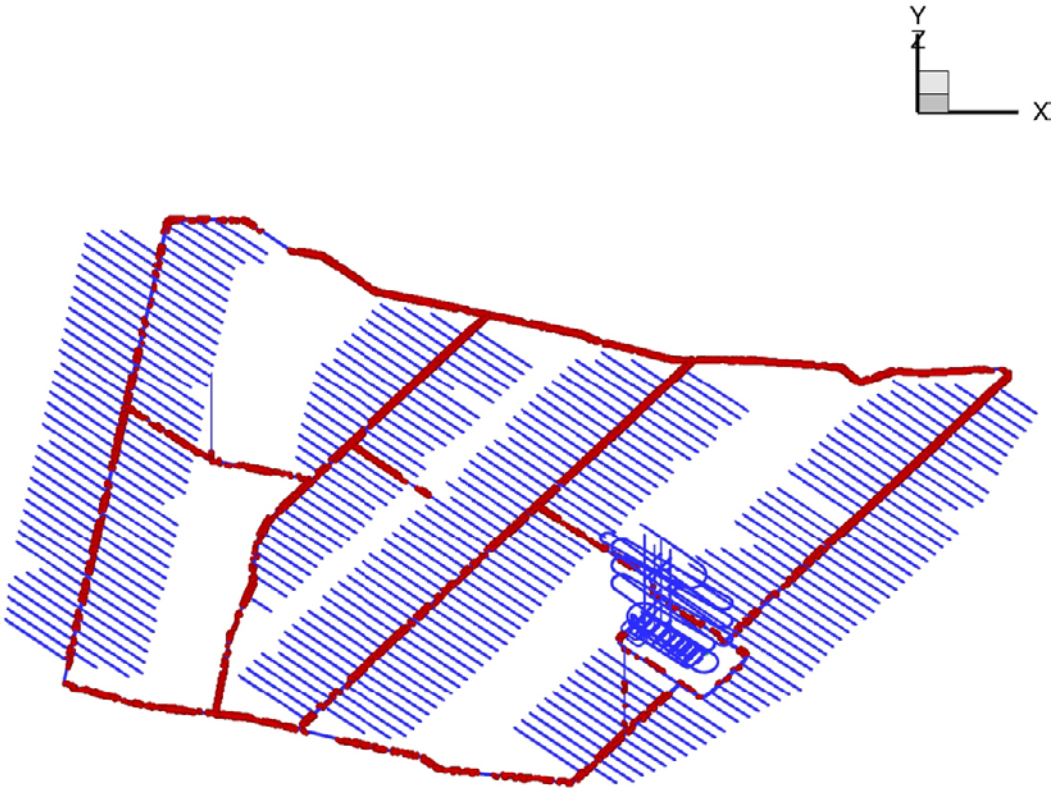

Figure 5-11. *Cells with an inflow rate greater than 0.1 L/min are marked up by spheres. Operation stage E and grouting level VI. No inflow rates greater than 0.5 L/min were found for grouting level VI.*

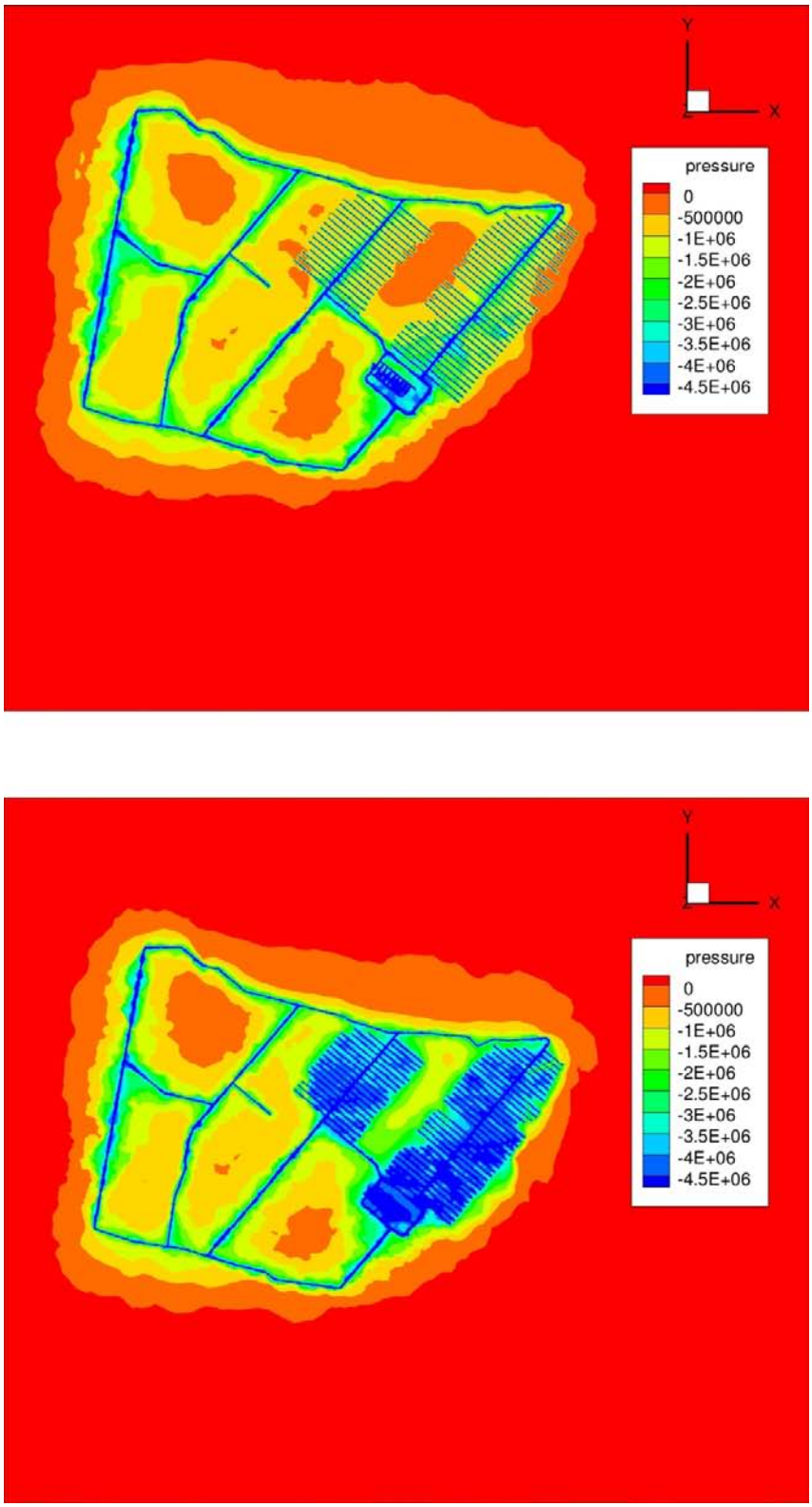

Figure 5-12. *Residual pressure distribution (Pa) around a final repository at –505 m elevation. Operation stage E and grouting level IV (top) and grouting level II. (The definition of the residual pressure is shown in Equation (3-3).) The y-axis points towards North.*

5.2.2 Drawdown of the groundwater table

The simulated drawdown of the groundwater table associated with four levels of grouting efficiency, III–VI, is shown in Figure 5-13. Only the drawdown for operation stage E is shown here. Stage E is the last stage and generates the largest inflows. For grouting levels I and II the groundwater table was frozen at the undisturbed levels and drawdowns can hence not be reported.

A drawdown of the groundwater table implies that shallow fresh and/or brackish water is transported towards the repository. The simulated drawdown is considerable and reaches the domain boundaries. This of course violates the boundary conditions and introduces some uncertainty.

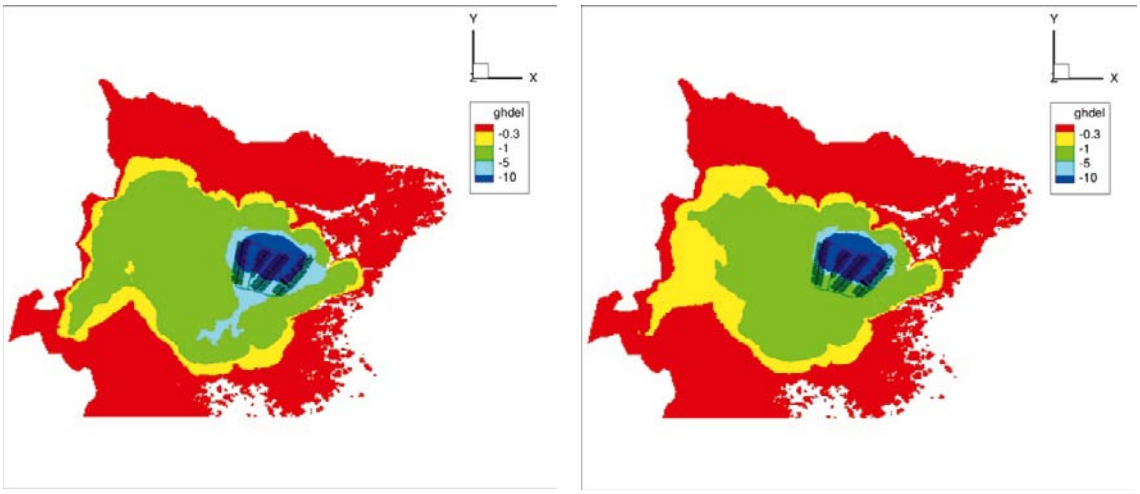

Grouting level III | Grouting level IV

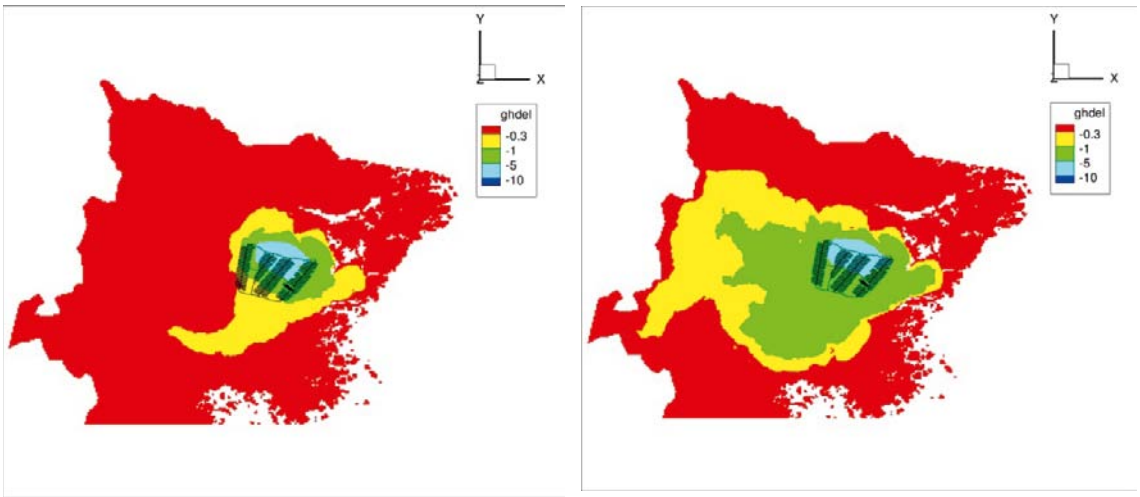

Grouting level V | Grouting level VI

Figure 5-13. *Simulated drawdown of the groundwater table at the end of operation stage E for four different levels of grouting efficiency, III–VI. The values shown in the legend are expressed in metres. The y-axis points towards North.*

5.2.3 Changes in the groundwater composition

The effect of the drawdown on the salinity distribution at repository depth for grouting level IV and operation stage E is shown in Figure 5-14 and Figure 5-15.

The figures suggest that the groundwater composition at repository depth is influenced by the less saline groundwater that exists above the repository.

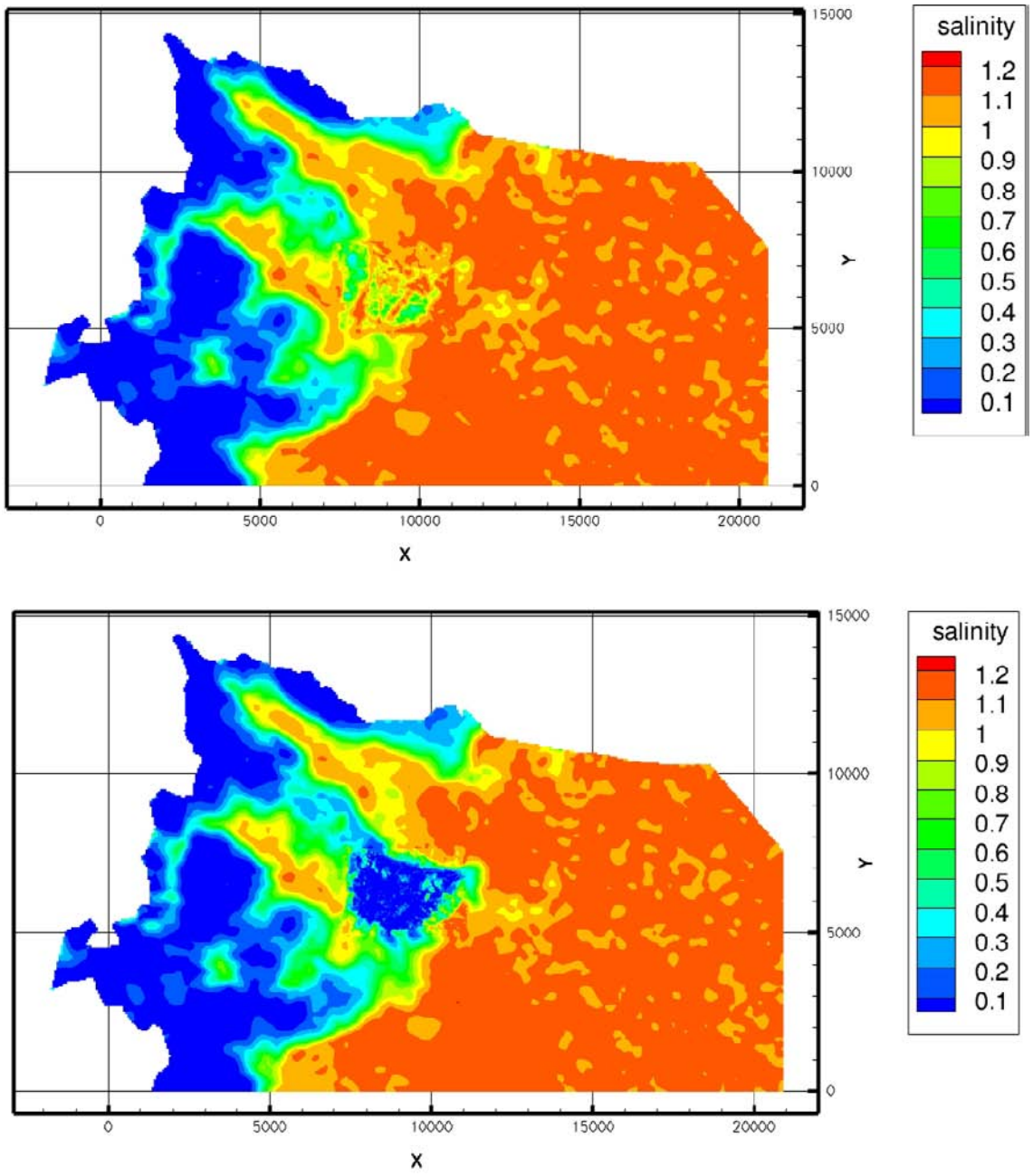

Figure 5-14. *Simulated salinity at –505 m elevation. Top: Pre-repository conditions (cf. Figure 5-4). Bottom: Conditions at the end of operation stage E for grouting level IV. The values shown in the legend are expressed in per cent by weight.*

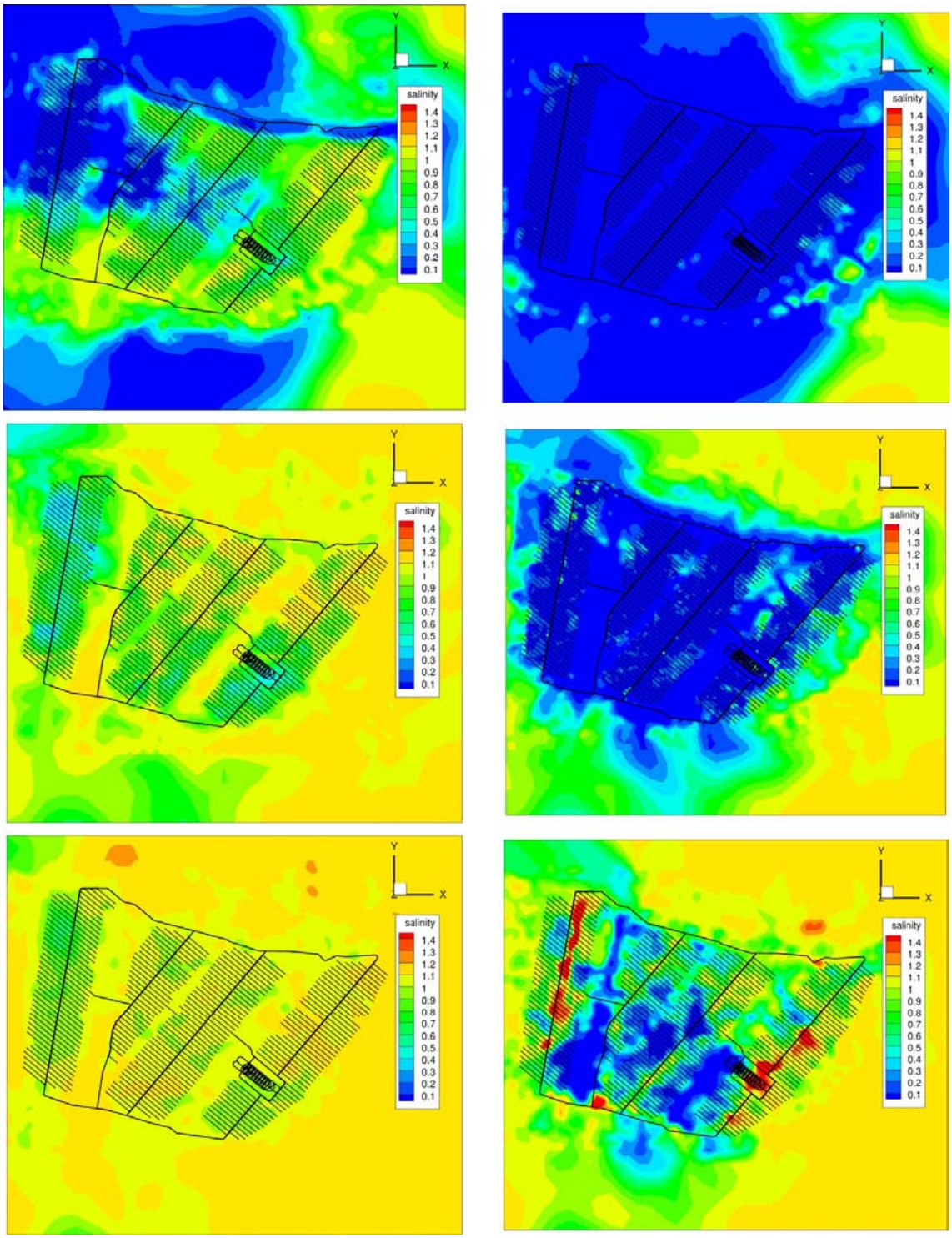

Figure 5-15. *Simulated salinity at –300 m (top), –505 m (middle) and –600 m (bottom) elevation. Left: Pre-repository conditions. Right: Conditions at the end of operation stage E for grouting level IV. The values shown in the legend are expressed in per cent by weight.*

5.3 Flow paths and travel times to an open repository

It is of interest to investigate the advective flow paths and travel times to the modelled repository. The flow paths indicate the location of potential recharge areas and the travel times can be used in hydrochemical calculations. For the sake of the work reported here, the modification described in Section 4.3, i.e. all parts of the repository layout were held open and had a grouting efficiency corresponding to level II.

The flow paths from the recharge areas carrying water to the open repository were identified by means of reversed particle tracking. That is, particles were released at repository depth and traced in a reversed flow field. The total simulation time was one year and the time step was one day.

The starting positions for the released particles were all cells in contact with the repository below –500 m elevation with an inflow rate greater than 1.0 L/min. In total 2,607 inflow points fulfilled this criterion. Figure 5-16 shows traces of 100 randomly selected particles. The body of these particles recharge right above the repository.

The advective travel times for the 2,607 inflow points are shown as a cumulative density function curve in Figure 5-17. The mass recovery was 98% and the median of the advective travel time from ground surface to an open repository is of the order of twenty days. This value is very low and suggests high advective transport velocities close to the repository. It is noted that the advective travel time computations are uncertain since the specified values of the grid cell hydraulic properties are provisional. This uncertainty is particularly true for the applied definition of the grid cell kinematic porosity.

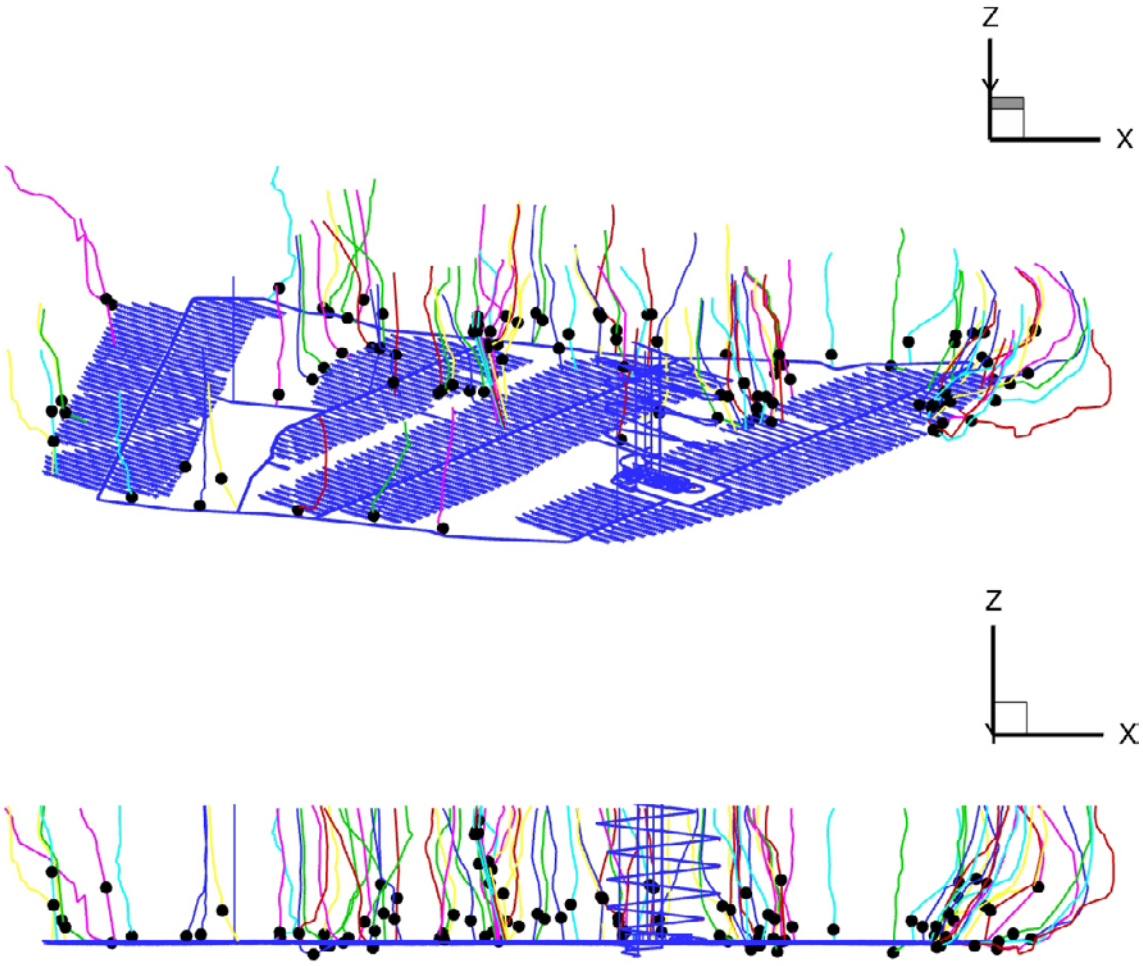

Figure 5-16. *Flow paths of 100 randomly selected particles traced by means of reversed particle tracking. The total simulation time was one year and the time step was one day. The black dots indicate the particle positions after one time step, i.e. the transport velocity close the repository is very high. The x-axis points towards East.*

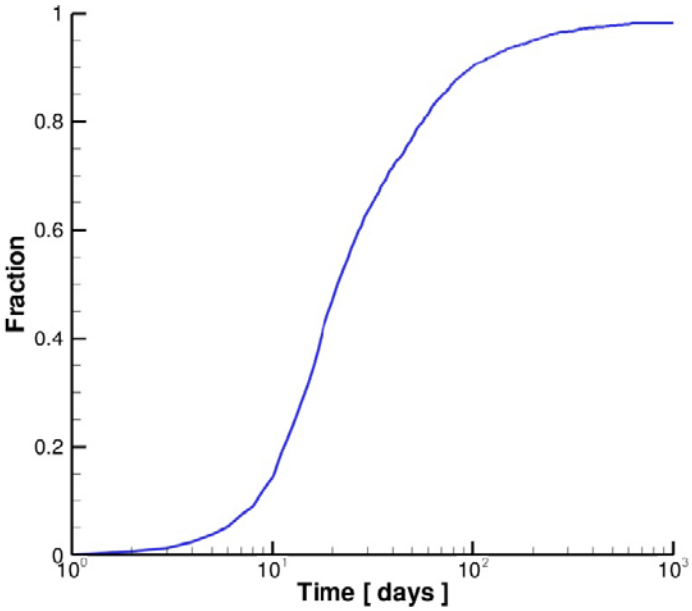

Figure 5-17. *The advective travel times for 2,607 inflow points shown as a cumulative density function curve.*

5.4 Saturation of the backfill

The modelling of the excavation and operational phases handled four successive stages of operation, A–D, see Figure C-2. When stage B was in operation, the part of the repository layout associated with stage A was assumed to be fully saturated, i.e. closed and with a zero inflow. By the same token, all parts of the repository layout associated with stages A and B were assumed to be fully saturated while stage C was in operation.

The assumption of an instantaneous, full saturation is obviously an approximation as the backfilling of the tunnels defines a starting point of a long transient phase, during which the backfill material will be gradually saturated. Appendix C is an excerpt of /Svensson 2010/. Appendix C briefly presents the hydration process and the approximate method used here to estimate the time scale of the saturation of the backfilling material. In short, the time was estimated by assuming that the hydration process of the unsaturated parts of the backfill can be modelled as a single-phase, saturated groundwater flow system. The specific storage of the unsaturated backfill was assigned a constant value and the specific storage of the saturated backfill another constant value.

The image shown in Figure 5-18 serves an example of the simulation results presented in Appendix C. In Figure 5-18, the boundary condition away from the unsaturated parts of the repository layout equals the hydrostatic pressure at –505 m elevation, i.e. about 5 MPa. Figure 5-18 suggests that large volumes associated with operation stage A are still at negative pressures after 100 days of hydration, i.e. unsaturated. The main conclusion of the results presented in Appendix C is that the time scale of the saturation process is around 10–30 years. Due to the approximate method used, where the specific storage is constant regardless the degree of saturation of the unsaturated backfill, it is not possible to be more specific.

A cell size of 1 m was used inside the tunnels in these simulations. This means that only two cells cover the distance from the tunnel axis to the tunnel/rock interface. This is probably the reason for the very fast (about 100 days) saturation of a tunnel section in contact with a fracture. From /Börgesson et al. 2006/ one can conclude that a more realistic time scale for the radial saturation is several years. However, the method used has been compared with simulations presented in /Börgesson et al. 2006/ and a good agreement was found. We hence conclude that the present simulations are carried out with too large cell sizes inside the tunnels.

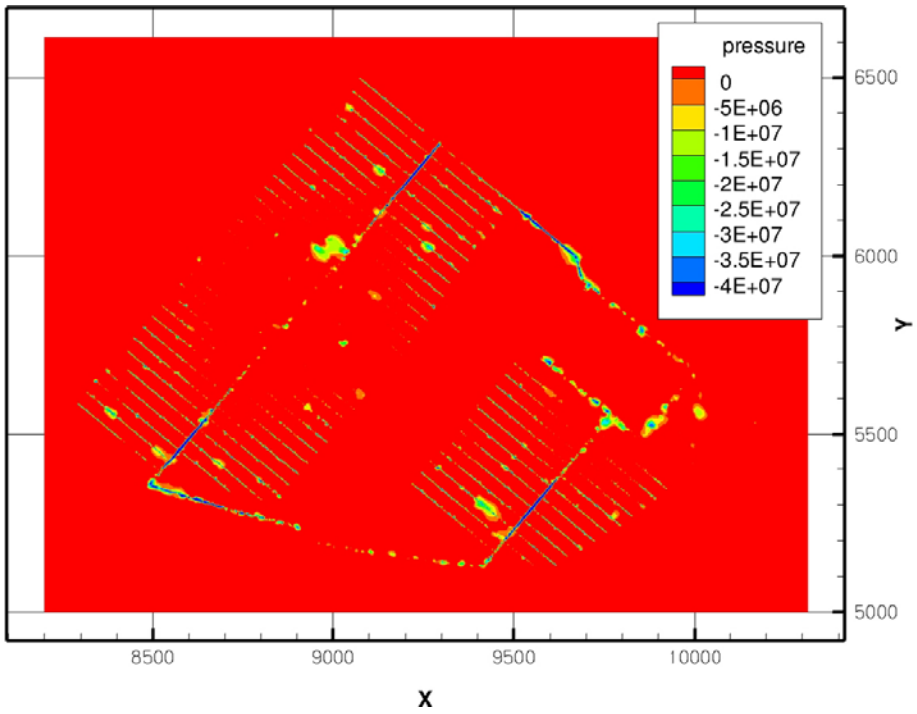

Figure 5-18. *Gauge pressure distribution (Pa) at –505 m elevation after hundred days of saturation of those parts of the repository layout associated with operation stage A. The pressure on the boundaries away from the unsaturated parts of the repository layout equals the hydrostatic pressure at repository depth, i.e. c. 5 MPa. The pressure distribution is based on a constant value of the specific storage in the unsaturated parts of the backfill, i.e. regardless of the degree of unsaturation.*

According to /Enssle and Poppei 2009/, saturation-dependent values of the specific storage enables a dynamic evolution of the hydration process and a method for the implementation in DarcyTools was derived. The implementation was verified numerically by /Enssle and Poppei 2009/ by comparisons with the TOUGH2 code /Pruess et al. 1999/. According to Figure 5-19, the pressure build-up proceeds more rapidly for saturation-dependent values of the specific storage. However, Figure 5-19 also indicates that the time needed to reach "full saturation" is almost the same, which demonstrates the capacity of the approximate method with a constant specific storage. A physical reason for a more rapid saturation is the non-linear capillary suction effects of the backfilling material, which are better described by the dynamic method. Hence, it is suggested that future calculations dealing with saturation are made with the dynamic method. For the sake of objectives of this report, the difference between the two approaches is sufficiently described by /Enssle and Poppei 2009/.

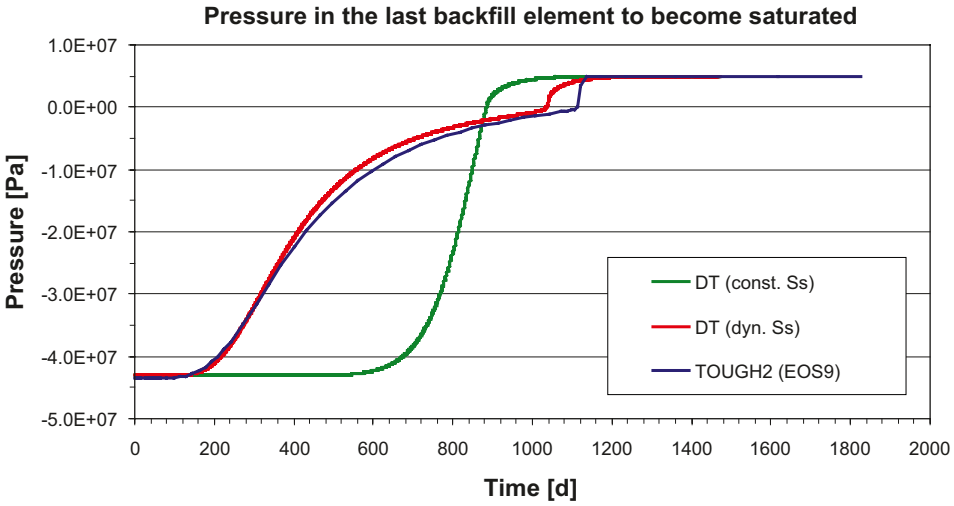

Figure 5-19. *Plot showing results from one of the test cases run by /Enssle and Poppei 2009/. The progress of the pressure build-up in the backfill using a dynamic (red graph) or a constant (green graph) specific storage in DarcyTools differs significantly. A solution obtained with the TOUGH2 code (blue graph) was used to verify the implementation of a dynamic specific storage in DarcyTools. (Source: Figure 3-3 in /Enssle and Poppei 2009/.)*

5.5 Sensitivity study

Table 5-2 shows the results of the sensitivity study. A few observations can be made in comparison with inflow rates for the modification described in Section 4.3.

- Case 1. The exclusion of deposition holes that did not pass the FPC and EFPC criteria rendered a slight decrease in the simulated total inflow rates in the deposition areas, all other parts are unaffected. The small effect found did not motivate any further analysis, for example differentiating between the FPC and EFPC criteria. The total inflow rate for this case was 428 L/s vs. 435 L/s for the base case.
- Case 2. A single deposition tunnel open rendered a slight increase in the inflow rates to some of the other open parts of the repository layout. This is due to higher pressure gradients to those parts when only one deposition tunnel is present.
- Case 3. Groundwater salinity appears to have little or no impact on the inflow rates, i.e. the fresh water variant rendered a very minute change in the total inflow rate, 420 L/s vs. 435 L/s for the base case.

As mentioned above, some cases shown in Table 5-1 were carried out with a frozen (or constant head) top boundary condition. Some tests, using grouting level IV, were done to study the impact of this approximation. Running cases with a free/frozen upper boundary showed that the frozen boundary condition may result in up to 10% too high inflows.

Table 5-2. Simulated inflow rates [L/s] to a final repository at Laxemar for the three cases handled in the sensitivity study. The simulations were carried out with the entire final repository open and a grouting efficiency corresponding to level II (cf. Table 4-3). CA = central area, DT = deposition tunnel, DH = deposition holes, ST = transportation and main tunnels, VS = ventilation shaft.

Part of repository	Modified Elaborated Hydro-DFN	1. FPC ∪ EFPC	2. Single tunnel	3. Fresh water
CA	17	15	17	15
ST1	10	10	21	10
VS1	1	1	1	1
DT1	2	2	3	2
DH1	–	–	1	–
DT2	36	37	–	35
DH2	11	10	–	11
ST3	18	18	–	18
VS2	1	1	–	1
DT3	33	33	–	32
DH3	10	8	–	9
ST4	17	17	–	16
DT4	16	14	–	16
DH4	51	52	–	49
ST5	36	36	–	35
DT5	141	143	–	137
DH5	35	31	–	32
∑	**435**	**428**	**43**	**420**

5.6 Hydraulic rejection criteria

The four variants of criteria presented in Section 4.2 were analysed using the modification described in Section 4.3. The numbers of rejected deposition holes are presented in Table 5-3. The prioritised variants for the scenario analyses carried out in SR-Site are number III and number IV. Variant III looks at the combination of criteria Q1 and Q2 and Variant IV looks at the combination of criteria Q1 and Q2 after all deposition hole positions that fail the combination of criteria FPC and EFPC have been excluded.

Table 5-3. Rejected number of deposition holes for the four variants studied.

Variant	Criterion	Rejected number of deposition holes	Figure
I	{Q1}	5,147	5-20
II	{Q2}	2,758	5-21
III	{Q1 ∪ Q2}	5,183	5-22
IV	{Q1 ∪ Q2} | exclusion of {FPC ∪ EFPC}	4,997	5-23

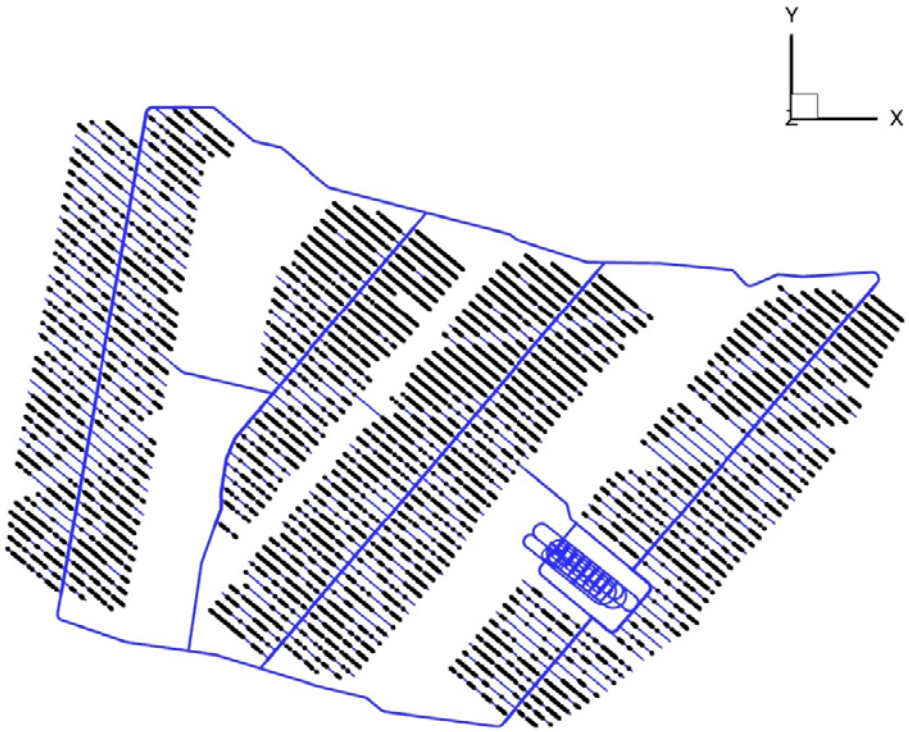

Figure 5-20. *Positions of the 5,147 deposition holes that did not pass the {Q1} criterion (Variant I).*

Figure 5-21. *Positions of the 2,758 deposition holes that did not pass the {Q2} criterion (Variant II).*

Figure 5-22. *Positions of the 5,183 deposition holes that did not pass the {Q1 ∪ Q2} criterion (Variant III).*

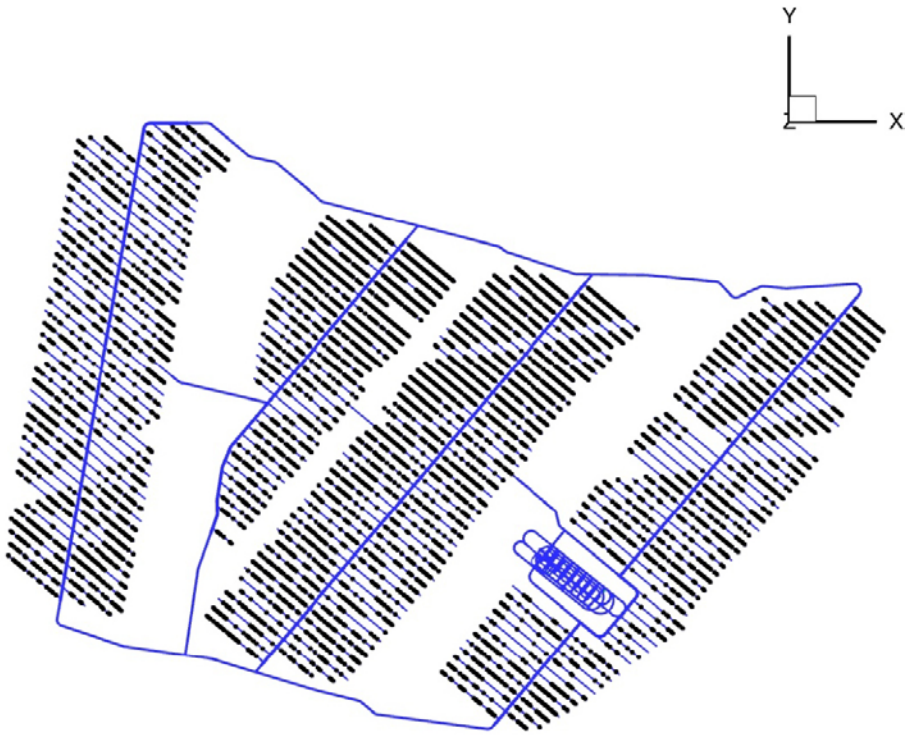

Figure 5-23. *Positions of the 4,997 deposition holes that did not pass the ({Q1 ∪ Q2} | exclusion of {FPC ∪ EFPC}) criterion (Variant IV).*

6 Summary and conclusions

6.1 Scope of work

This report presents inflow rates, drawdown of the groundwater table and upconing of deep saline water for an open final repository for spent fuel at Laxemar. All flow simulations were carried out with the computational code called DarcyTools, which is based on the assumption that flow and transport through sparsely fractured crystalline rocks can be handled as flow and transport through an equivalent continuous porous medium (ECPM). The body of the flow simulations was made for the Elaborated Hydro-DFN model setup, which was accompanied by a sensitivity study. The latter handled, among other matters, different deposition hole rejection criteria. Besides informing about possible effects of the excavation and operational phases, the report also presents tentative modelling results for the saturation phase, which starts once the completed parts of the repository are being backfilled.

In principle, the setup of the Elaborated Hydro-DFN model has followed the guidelines specified by SKB for the SR-Site project at Forsmark, see /Selroos and Follin 2010/ for details. In concrete words, the geometries and hydraulic properties of all modelled discrete features such as individual fractures, deformation zones and repository layout components (shafts, ramp, tunnels and deposition holes) were explicitly imported from a quality assured database managed by SKB, whereas other modelling issues such as initial and boundary conditions, model variants etc. followed the prerequisites for modelling outlined in /Selroos and Follin 2010/.

Present-day lakes and wetlands, surface water (stream) runoff rates and groundwater chemistry were loosely used as "calibration targets" for the modelled evolution of the hydrological and hydrochemical conditions during Holocene time (8000 BC to 2000 AD). The simulated conditions at 2000 AD were used as reference for the identification of disturbances caused by the subsequent flow modelling of the excavation and operational phases.

Five scenarios, or operation stages A–E, of the repository development were studied, i.e. not all parts of the repository were open at the same time. As a variant and sensitivity test, the effect of only one deposition tunnel open was also studied.

The impact of grouting on the calculated inflow rates, drawdown of the groundwater table and upconing of deep saline water was studied by altering the hydraulic conductivity of the computational grid cells in contact with the modelled repository. Six levels of grouting efficiency, I–VI, were studied for each operation stage A–E.

For the modelling of the saturation process following the closure of the operational phase, a tentative, approximate method was applied. The backfilling material was assumed to have hydraulic properties similar to that of Friedland Clay.

Two inflow rate thresholds were analysed to study the implication of using hydraulic criteria for the rejection of deposition holes. The effect of the hydraulic rejection criteria was analysed alone and in combination with two fracture-geometry-based rejection criteria (Figure 4-8 and Figure 4-9).

6.2 Elaborated Hydro-DFN model

The simulated total inflow to the modelled repository was found to be in the range 10–452 L/s, depending on the level of the grouting efficiency, see Table 5-1.

The simulated drawdown was generally extensive. The largest simulated drawdown was observed above the north part of the repository (more than 10 m).

The bedrock below the repository is less permeable than the bedrock above, and, in principle, the groundwater salinity in the vicinity of the repository decreased from about 1% to almost zero salinity. This result suggests an infiltration of the less saline groundwater that occur above the repository and very little or no upconing of deep saline groundwater.

In the present groundwater flow model, the recharge flux of meteoric water was unchanged during the excavation and operational phases. Since the inflow was not accompanied by an increase of the net precipitation, the radius of influence is probably larger than otherwise.

The median of the advective travel times from ground surface to an open repository is of the order of twenty days. This value is very low and suggests high advective transport velocities close to the repository. It is noted that the advective travel time computations are uncertain since the specified values of the grid cell hydraulic properties are provisional. This uncertainty is particularly true for the applied definition of the grid cell kinematic porosity.

The time needed to achieve a full saturation in the backfilled parts of the repository can be expected to be about 10 years using a constant specific storage for the hydration of the unsaturated parts of the backfilling material. In reality, the hydration process can be expected to be more rapid, due to, among other things, the capillary suction of the backfilling material. However, it is noted that the time needed to reach complete saturation is about the same for a constant specific storage as for a saturation dependent specific storage. Nevertheless, it is suggested that future calculations with DarcyTools dealing with saturation are made with saturation-dependent values of the specific storage since this enables a dynamic evolution of the hydration process /Enssle and Poppei 2009/. It is further noted that the simulations presented need to be checked for grid independence; a cell size of 1 m inside the tunnels is probably too large.

6.2.1 Sensitivity study

The exclusion of deposition holes that did not pass the FPC and EFPC criteria rendered a slight decrease in the simulated inflow rates in the deposition areas, all other parts are unaffected. The small effect found did not motivate any further analysis, for example differentiating between the FPC and EFPC criteria.

A single deposition tunnel open rendered a slight increase in the inflow rates to some of the other open parts of the repository layout. This is due to higher pressure gradients to those parts when only one deposition tunnel is present.

Groundwater salinity appears to have little or no impact on the inflow rates.

6.2.2 Hydraulic rejection criteria

The combination of hydraulic deposition hole rejection criteria and geometry-based deposition hole rejection criteria led to rejection of about 62% of the possible deposition holes (4,997 out of a total of 8,031), based on the conditions specified in Section 4.3. This is of course a very high number which however directly relates to the hydro DFN used. It is beyond the scope of the present report to evaluate if the hydro DFN is a good representation of the rock, but it certainly results in very transmissive conditions.

6.3 Hydrogeological base case model

As explained in the work by /Joyce et al. 2010/, two hydrogeological discrete fracture network (Hydro-DFN) models are defined for Laxemar; the Hydrogeological base case and the Elaborated Hydro-DFN.

The Hydrogeological base case model is compared with the Elaborated Hydro-DFN model in Appendix E. The comparison between the two models shows that the Elaborated Hydro-DFN model results in lower inflow rates to an open repository (about 56% of the total inflow rate generated by the Hydrogeological base case model). A corresponding lower drawdown of the groundwater table is found, while the salinity field at repository depth seems to be less affected.

7 References

Börgesson L, Fälth B, Hernelind J, 2006. Water saturation phase of the buffer and backfill in the KBS-3V concept. Special emphasis given to the influence of the backfill on the wetting of the buffer. SKB TR-06-14, Svensk Kärnbränslehantering AB.

Dershowitz W, Wiberg A, Hermanson J, Byegård J, Tullborg E-L, Andersson P, Mazurek M, 2003. Äspö Task Force on modelling of groundwater flow and transport of solutes. Task 6c. A semi-synthetic model of block scale conductive structures at the Äspö HRL. SKB IPR-03-13, Svensk Kärnbränslehantering AB.

El Tani M, 2003. Circular tunnel in a semi-infinite aquifer. Tunneling and Underground Space Technology, 18, pp 49–55.

Enssle C P, Poppei J, 2010. Implementation and testing of an improved methodology to simulate resaturation processes with DarcyTools. SKB R-09-54, Svensk Kärnbränslehantering AB.

Fetter C W, 1994. Applied hydrogeology. 3rd ed. Upper Saddle River: Prentice-Hall.

Follin S, 2008. Bedrock hydrogeology Forsmark, Site descriptive modelling, SDM-Site Forsmark, R-08-95, Svensk Kärnbränslehantering AB.

Follin S, Stigsson M, Berglund S, Svensson U, 2004. Variable-density groundwater flow simulations and particle tracking – numerical modelling using DarcyTools. Preliminary site description of the Simpevarp area – version 1.1. SKB R-04-65, Svensk Kärnbränslehantering AB.

Follin S, Stigsson M, Svensson U, 2005. Variable-density groundwater flow simulations and particle tracking – numerical modelling using DarcyTools. Preliminary site description. Simpevarp subarea – version 1.2. SKB R-05-11, Svensk Kärnbränslehantering AB.

Follin S, Stigsson M, Svensson U, 2006. Hydrogeological DFN modelling using structural and hydraulic data from KLX04. Preliminary site description, Laxemar subarea – version 1.2. SKB R-06-24, Svensk Kärnbränslehantering AB.

Fredén C (ed), 2002. Sveriges nationalatlas. Berg och Jord (in Swedish). Stockholm: SNA publishing.

Gustafson G, Fransson Å, Funehag J, Axelsson M, 2004. Ett nytt angreppssätt för bergbeskrivning och analysprocess för injektering. V-byggaren: Väg- och vattenbyggaren, 4, pp 10–15 (in Swedish).

Haggerty R, Gorelick S M, 1995. Multiple-rate mass transfer for modeling diffusion and surface reactions in media with pore-scale heterogeneity. Water Resources Research, 31, pp 2383–2400.

Harlow F H, Welsch J E, 1965. Numerical calculations of time-dependent viscous incompressible flow of fluid with free surface. Physics of Fluids, 8, pp 2182–2189.

Hartley L, Worth D, Gylling B, Marsic N, Holmén J, 2004. Preliminary site description: Groundwater flow simulations. Simpevarp area (version 1.1) modelled with CONNECTFLOW. SKB R-04-63, Svensk Kärnbränslehantering AB.

Hartley L, Hoch A, Hunter F, Jackson P, Marsic N, 2005. Regional hydrogeological simulations – numerical modelling using CONNECTFLOW. Preliminary site description. Simpevarp sub area – version 1.2. SKB R-05-12, Svensk Kärnbränslehantering AB.

Hartley L, Hunter F, Jackson P, McCarthy R, Gylling B, Marsic N, 2006a. Regional hydrogeological simulations using CONNECTFLOW. Preliminary site description. Laxemar subarea – version 1.2. SKB R-06-23, Svensk Kärnbränslehantering AB.

Hartley L, Hoch A, Jackson P, Joyce S, McCarthy R, Rodwell W, Swift B, Marsic N, 2006b. Groundwater flow and transport modelling during the temperate period for the SR-Can assessment. Forsmark area – version 1.2. SKB R-06-98, Svensk Kärnbränslehantering AB.

Hartley L, Hoch A, Jackson P, Joyce S, McCarthy R, Swift B, Gylling B, Marsic N, 2006c. Groundwater flow and transport modelling during the temperate period for the SR-Can assessment. Laxemar subarea – version 1.2. SKB R-06-99, Svensk Kärnbränslehantering AB.

Hartley L, Jackson P, Joyce S, Roberts D, Shevelan J, Swift B, Gylling B, Marsic N, Hermanson J, Öhman J, 2007. Hydrogeological pre-modelling exercises. Assessment of impact of the Äspö Hard Rock Laboratory. Sensitivities of palaeo-hydrogeology. Development of a local near-surface Hydro-DFN for KLX09B–F. Site descriptive modelling, SDM-Site Laxemar SKB R-07-57, Svensk Kärnbränslehantering AB.

Holmén J G, 2008. Premodelling of the importance of the location of the upstream hydraulic boundary of a regional flow model of the Laxemar-Simpevarp area. Site descriptive modelling, SDM-Site Laxemar. SKB R-08-60, Svensk Kärnbränslehantering AB.

Joyce S, Simpson T, Hartley L, Applegate D, Hoek J, Jackson P, Roberts D, Swan D, Gylling B, Marsic N, Rhén I, 2010. Groundwater flow modelling of periods with temperate climate conditions – Laxemar. SKB R-09-24, Svensk Kärnbränslehantering AB.

Larsson-McCann S, Karlsson A, Nord M, Sjögren J, Johansson L, Ivarsson M, Kindell S, 2002. Meteorological, hydrological and oceanographical data for the site investigation program in the community of Oskarshamn. SKB TR-02-03, Svensk Kärnbränslehantering AB.

Munier R, 2006. Using observations in deposition tunnels to avoid intersections with critical fractures in deposition holes. SKB R-06-54, Svensk Kärnbränslehantering AB.

Nyman H, Sohlenius G, Strömgren M, Brydsten L, 2008. Depth and stratigraphy of regolith. Site descriptive modelling, SDM-Site Laxemar. SKB R-08-06, Svensk Kärnbränslehantering AB.

Patankar S V, 1980. Numerical heat transfer and fluid flow. New York: Hemisphere. (Series in computational methods in mechanics and thermal sciences)

Pruess K, Oldenburg C, Moridis G J, 1999. TOUGH2 user's guide, version 2.0. Report LBNL-43134, Lawrence Berkeley National Laboratory, Berkeley.

Rhén I, Hartley L, 2009. Bedrock hydrogeology Laxemar, Site descriptive modelling, SDM-Site Laxemar. SKB R-08-92, Svensk Kärnbränslehantering AB.

Rhén I (ed), Gustafson G, Stanfors R, Wikberg P 1997. Äspö HRL – Geoscientific evaluation 1997/5. Models based on site characterization 1986–1995. SKB TR 97-06, Svensk Kärnbränslehantering AB.

Rhén I, Follin S, Hermanson J, 2003. Hydrological Site Descriptive Model – a strategy for its development during Site Investigations. SKB R-03-08, Svensk Kärnbärnslehantering AB.

Rhén I, Forsmark T, Forssman I, Zetterlund M, 2006a. Hydrogeological single-hole interpretation of KSH01, KSH02, KSH03, KAV01 and HSH01–03, Preliminary site description, Simpevarp subarea – version 1.2, SKB R-06-20, Svensk Kärnbränslehantering AB.

Rhén I, Forsmark T, Forssman I, Zetterlund M, 2006b. Hydrogeological single-hole interpretation of KLX02, KLX03, KLX04, KAV04A and B, HAV09–10 and 9 HLXxx boreholes. Laxemar subarea – version 1.2. SKB R-06-21, Svensk Kärnbränslehantering AB.

Rhén I, Forsmark T, Forssman I, Zetterlund M, 2006c. Evaluation of hydrogeological properties for Hydraulic Conductor Domains (HCD) and Hydraulic Rock Domains (HRD). Laxemar subarea – version 1.2. SKB R-06-22, Svensk Kärnbränslehantering AB.

Rhén I, Forsmark T, Hartley L, Jackson C P, Roberts D, Swan D, Gylling B, 2008. Hydrogeological conceptualisation and parameterisation. Site descriptive modelling, SDM-Site Laxemar. SKB R-08-78, Svensk Kärnbränslehantering AB.

Rhén I, Forsmark T, Hartley L, Joyce S, Roberts D, Gylling B, Marsic N, 2009. Bedrock hydrogeology. Model testing and synthesis. Site descriptive modelling, SDM-Site Laxemar. SKB R-08-91, Svensk Kärnbränslehantering AB.

Selroos J-O, Follin S, 2010. SR-Site groundwater flow modelling methodology, setup and results. SKB R-09-22, Svensk Kärnbränslehantering AB.

SKB, 2002. Simpevarp – site descriptive model version 0. SKB R-02-35, Svensk Kärnbränslehantering AB.

SKB, 2004. Preliminary site description Simpevarp area – version 1.1. SKB R-04-25, Svensk Kärnbränslehantering AB.

SKB, 2005. Preliminary site description. Simpevarp subarea – version 1.2. SKB R-05-08, Svensk Kärnbränslehantering AB.

SKB, 2006a. Preliminary site description. Laxemar subarea – version 1.2. SKB R-06-10, Svensk Kärnbränslehantering AB.

SKB, 2006b. Preliminary site description Laxemar stage 2.1. Feedback for completion of the site investigation including input from safety assessment and repository engineering. SKB R-06-110, Svensk Kärnbränslehantering AB.

SKB, 2007. Final repository facility. Underground design premises/D2. SKB R-07-33, Svensk Kärnbränslehantering AB.

SKB, 2008. Site description of Forsmark at completion of the site investigation phase. SDM-Site Forsmark. SKB TR-08-05, Svensk Kärnbränslehantering AB.

SKB, 2009a. Site description of Laxemar at completion of the site investigation phase. SDM-Site Laxemar. SKB TR-09-01, Svensk Kärnbränslehantering AB.

SKB, 2009b. Confidence assessment. Site descriptive modelling, SDM-Site Laxemar. SKB R-08-101, Svensk Kärnbränslehantering AB.

SKB, 2010. Comparative analysis of safety related site characteristics. SKB TR-10-54, Svensk Kärnbränslehantering AB.

Sohlenius G, Hedenström A, 2008. Description of regolith at Laxemar-Simpevarp. Site descriptive modelling, SDM-Site Laxemar. SKB R-08-05, Svensk Kärnbränslehantering AB.

Svensson U, 2010. Evaluation of a new method to estimate the hydration time of the tunnel backfill. SKB R-10-06 Svensk Kärnbränslehantering AB.

Svensson U, Ferry M, Kuylenstierna H-O, 2010. DarcyTools, Version 3.4. Concepts, methods and equations. SKB R-07-38, Svensk Kärnbränslehantering AB.

Söderbäck B (ed), 2008. Geological evolution, palaeoclimate and historical development of the Forsmark and Laxemar-Simpevarp areas. Site descriptive modelling, SDM-Site. SKB R-08-19, Svensk Kärnbränslehantering AB.

Thiem G, 1906. Hydrologische Methoden. Leipzig: Gebhardt.

Vidstrand P, Rhén I, Zugec N, 2010. Groundwater flow modelling of periods with periglacial and glacial climate conditions – Laxemar. SKB R-09-25, Svensk Kärnbränslehantering AB.

Wahlgren C-H, Curtis P, Hermanson J, Forssberg O, Öhman J, Fox A, La Pointe P, Drake H, Triumf C-A, Mattsson H, Thunehed H, Juhlin C, 2008. Geology Laxemar. Site descriptive modelling, SDM-Site Laxemar. SKB-R-08-54, Svensk Kärnbränslehantering AB.

Werner K, 2009. Description of surface hydrology and near-surface hydrogeology at Laxemar-Simpevarp. Site descriptive modeling, SDM-Site Laxemar. SKB R-08-71, Svensk Kärnbränslehantering AB.

Werner K, Öhman J, Holgersson B, Rönnback K, Marelius F, 2008. Meteorological, hydrological and hydrogeological monitoring data and near-surface hydrogeological properties data from Laxemar-Simpevarp. Site descriptive modelling, SDM-Site Laxemar. SKB R-08-73, Svensk Kärnbränslehantering AB.

Appendix A

Free surface algorithm

A1 Introduction

The elevation of the groundwater table may affect the pressure field in the bedrock depending on the hydraulic contact between the Quaternary deposits and the bedrock. Unfortunately it is not straight forward to calculate the position of the groundwater table. From the literature two methods are available:

- The unsaturated-saturated approach, which means that the unsaturated zone is included in the flow simulation and that the so called Richard's equation is solved.
- Free surface approach. The main assumption of the method is that the conditions in the unsaturated zone do not significantly affect the position of the groundwater table.

DarcyTools applies a method to determine the groundwater table that is somewhat in between the two approaches listed above. The basic idea is as follows.

The flow situation shown in Figure A-1 assumes saturated flow through porous medium and results in a particular pressure distribution results where points on a surface with atmospheric pressure (gauge pressure = 0) can be identified. This surface is not the groundwater table, however, because horizontal flow is calculated above this surface. The key feature of the free surface algorithm in DarcyTools is to prevent horizontal flow above the surface of atmospheric pressure by simply reducing the horizontal hydraulic conductivity above this surface. This is done in an iterative manner: 1) the flow problem is solved and the position of the atmospheric pressure is identified, 2) the horizontal conductivities are revised according to the position of the surface of atmospheric pressure, and 3) the flow problem is recalculated, etc. Note that if a rising surface is recalculated, the horizontal conductivities below the new surface of atmospheric pressure should be restored to the fully saturated values.

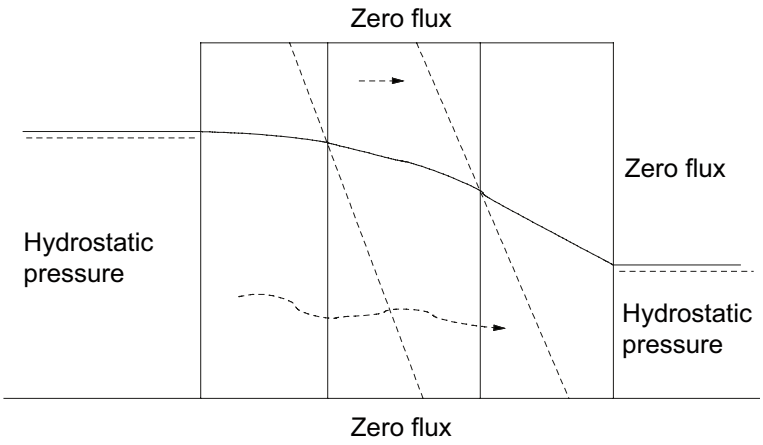

Figure A-1. *Illustration of a flow solution where saturated flow is assumed. This assumption results in an incorrect position of the groundwater table.*

A2 Objectives

The objective of this appendix case is to verify that the free surface algorithm in DarcyTools predicts a groundwater table that is in agreement with an analytical solution to the flow situation shown in Figure A-2.

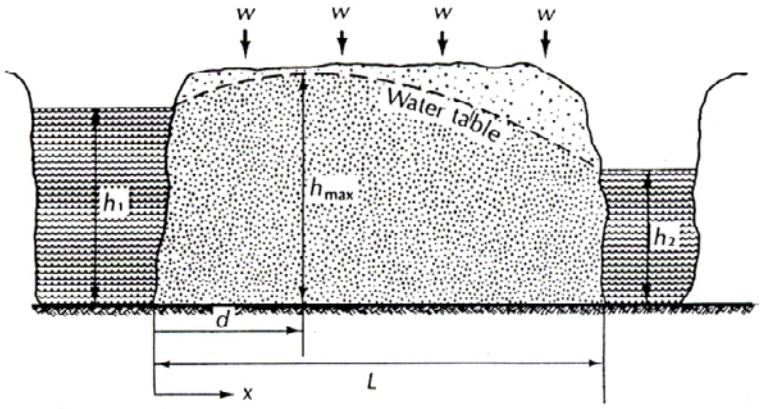

Figure A-2. *Illustration of the studied situation and the notation used in Equation (A-1). The symbols are explained in the text. (Figure 5-19 in /Fetter 1994/.)*

A3 Analytical solution

If Dupuit's assumption is invoked, which imply vertical equipotentials, the hydraulic head, h, between $h(x = 0) = h_1$ and $h(x = L) = h_2$, at a distance, x, between the two head boundaries, may be written as /Fetter 1994/:

$$h(x) = \sqrt{h_1^2 - \frac{\left(h_1^2 - h_2^2\right)x}{L} + \frac{w}{K}(L - x)x} \qquad \text{(A-1)}$$

where K [LT^{-1}] is the hydraulic conductivity in the direction of flow and w [LT^{-1}] is the recharge.

One way to simulate Dupuit's assumptions in DarcyTools is to introduce a higher conductivity in the vertical direction (as compared to the horizontal ones). This will make the vertical pressure distribution close to the hydrostatic one, i.e. vertical equipotentials.

A3 Numerical simulation

The hydraulic properties used for the flow simulation in DarcyTools are shown in Table A-1.

Table A-1. Simulation parameters.

Domain size	100 m (horizontal), 50 m (vertical)
Grid (cell) size	$\Delta x = \Delta z = 1$ m
Hydraulic conductivity	10^{-8} m/s (horizontal), 10^{-6} m/s (vertical)
Boundary conditions	Bottom: no flow Top: prescribed flux (P–E); 100 mm/y or 20 mm/y Left: hydrostatic pressure, $h_1 = 30$ m Right: hydrostatic pressure, $h_2 = 20$ m

A4 Summary and conclusions

The comparison with the analytical solution is shown in Figure A-3. Figure A-4 shows the flow pattern. The steady state groundwater table, as predicted by DarcyTools, is in good agreement with the corresponding analytical solution.

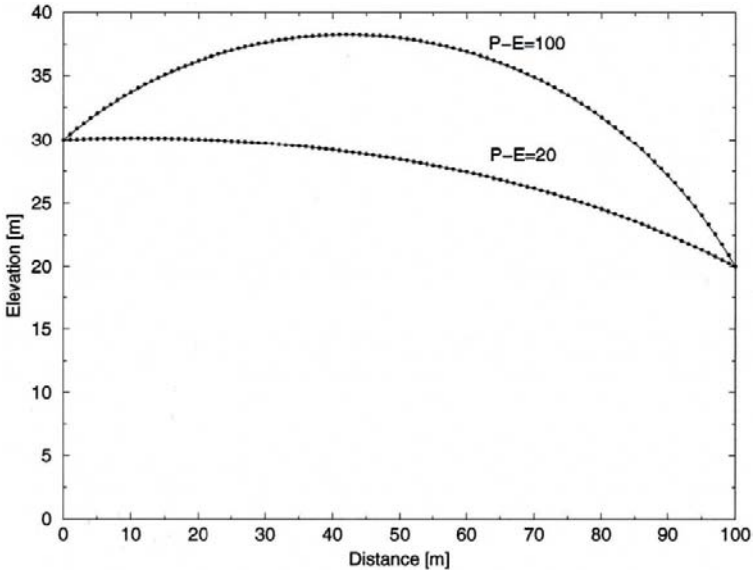

Figure A-3. *Comparison between analytically (line) and numerically (dots) calculated hydraulic heads for two (P–E) values, 20 mm/y and 100 mm/y.*

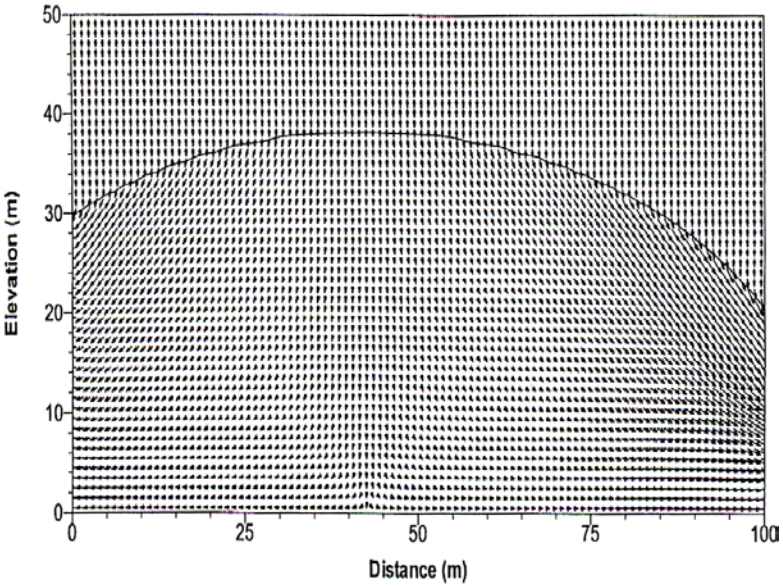

Figure A-4. *Predicted flow and groundwater table for (P–E) = 100 mm/y.*

Appendix B

Tunnel routine

B1 Introduction

A routine is implemented in DarcyTools to simulate the inflow of groundwater to tunnels and other underground objects that are subjected to atmospheric pressure. The routine assumes that the resolution of the computational grid is of the same size as the underground objects handled.

Figure B-1 shows the basic idea. The large circle indicates the cross-section of an underground object (construction). All cells that are in contact with the border of the object are marked up by red rectangles and the associated cell walls are indicated by blue circles. The marked up cells are assigned an atmospheric pressure ($p = 0$) at their centres and the hydraulic conductivities of the cell walls (K_{cw}) are matched against a predefined hydraulic conductivity threshold (K_t) representing a specified level of grouting efficiency. The routine applies the following criterion:

$$K_{cw,new} = \min(K_{cw,old}, K_t \qquad \text{(B-1)}$$

This adjustment of the cell wall hydraulic conductivity was used to simulate the effect of grouting in the work reported here.

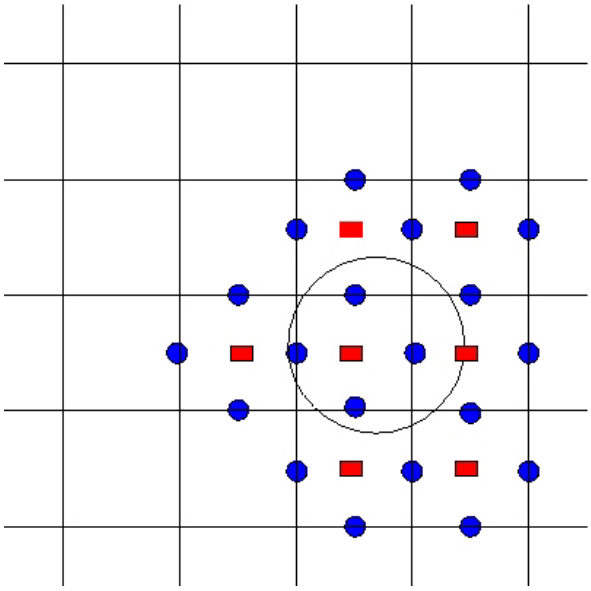

Figure B-1. *Cartoon showing the structural components of the tunnel routine in DarcyTools. The thin line is the perimeter of a tunnel. Red rectangles indicate the centres of the cells in contact with the tunnel. Blue circles indicate the cell walls of these cells.*

B2 Objectives

The objective of this appendix is to evaluate the accuracy of the tunnel routine for conditions (grid cell size and tunnel geometries) relevant for a final repository.

B3 Comparison with an analytical solution

For steady-state flow towards a circular tunnel in a semi-infinite isotropic and homogeneous aquifer the inflow rate per unit length of the tunnel, q [m^3/s, m], may be derived from well function provided by /Thiem 1906/:

$$q = 2\pi K d \left[\ln\left(\frac{2d}{r} \right) \right]^{-1} \qquad \text{(B-2)}$$

where K is the hydraulic conductivity of the porous medium, r is the radius of the tunnel and d is the depth below a constant-head boundary, e.g. a fixed groundwater table. Equation (B-2) is valid for $\frac{d}{r} >> 1$. If $\frac{d}{r} \approx 10$, the error in q is of the order of 1%.

An outline of the flow model setup in DarcyTools is shown in Figure B-2. The hydraulic properties used for the flow simulation are shown in Table B-1.

Table B-1. Parameters values for simulations of inflow to an open tunnel.

Domain size	4,000 m (horizontal), 2,000 m (vertical)
Grid (cell) size	Tunnel: Max(Δx, Δz) = 0.1 m Near field: Max(Δx, Δz) = 0.5 m Far field: Max(Δx, Δz) = 8 m
Hydraulic conductivity	10^{-8} m/s
Boundary conditions	Bottom: no flow Vertical: no flow Top: atmospheric pressure Tunnel: atmospheric pressure
Tunnel data	Depth: 500 m Radius: 1 m, 2 m and 4 m

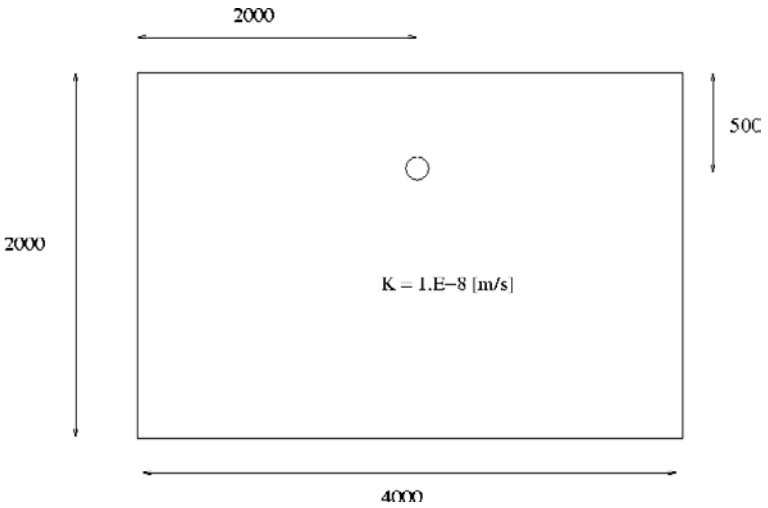

Figure B-2. *Illustration of the studied situation.*

The comparison with the analytical solution is shown in Figure B-3. /El Tani 2003/ provides means to calculate correction factors for finite values of *d/r*. For the present setup variants of *d/r*, it was found that the calculated correction factors are insignificant. Moreover, a sensitivity study with focus on the discretisation of the computational grid in proximity to the tunnel showed that grid independent solutions were achieved when the cell size was of the same size as the tunnel radius or smaller, see Table B-2.

It was found, however, that the horizontal size of the domain needed to be quite large (4,000 m) to achieve correct solutions. A smaller size (2,000 m) affected the inflow rates with several percent.

Table B-2. Comparison between analytical and numerical solutions of the inflow rate, q, to the tunnel shown in Figure B-2 and Table B-1. Inflow rates ($q = N \cdot 10^{-6}$ m³/s/m) are shown for three radii and three cell sizes.

Solution	Tunnel radius (m)		
	1	2	4
Analytical	4.55	5.06	5.69
Numerical, cell size (Δx, Δz) = 0.5 m	4.62	5.04	5.63
Numerical, cell size (Δx, Δz) = 1 m	4.80	5.14	5.67
Numerical, cell size (Δx, Δz) = 2 m	4.80	5.37	5.79

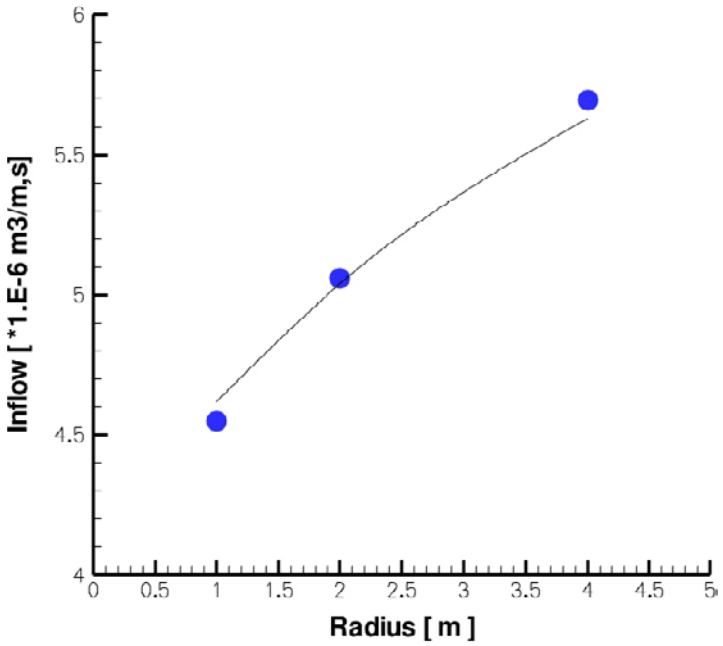

Figure B-3. *Comparison between analytically (line) and numerically (dots) calculated inflow rates for different tunnel radii.*

B4 Coarse computational grids vis-à-vis the tunnel radius

Figure B-4 shows three different cases of tunnels where the tunnel diameter is less than the cell size of the computational grid (4 m). In case A, four cells will be marked as tunnel cells, in case B two cells and in case C one cell. The numerical flow simulations were carried out for a tunnel radius of 1 m and the analytical solutions were made for two values of the tunnel radius, 1 m and 2 m. The numerical and analytical solutions are shown in Table B-3. (It is noted that the analytical solution is sensitive to the tunnel radius, whereas the tunnel radius is unimportant for the numerical solution if the radius is less than the cell size (discretisation).)

Table B-3. The inflow rates ($q = N \cdot 10^{-6}$ m^3/s/m) shown in the upper row are calculated using the tunnel routine for three different positions of the tunnel, A–C, see Figure B-4. The values shown in the lowermost two rows represent inflow rate ratios for two different tunnel radii, 1 m and 2 m. The average of the six ratios is 1.01.

	Case		
Solution	A	B	C
Numerical q (tunnel routine with r =1)	5.28	4.87	4.36
(Numerical q)/(Analytical q with r = 1 m)	1.16	1.07	0.96
(Numerical q)/(Analytical q with r = 2 m)	1.04	0.96	0.86

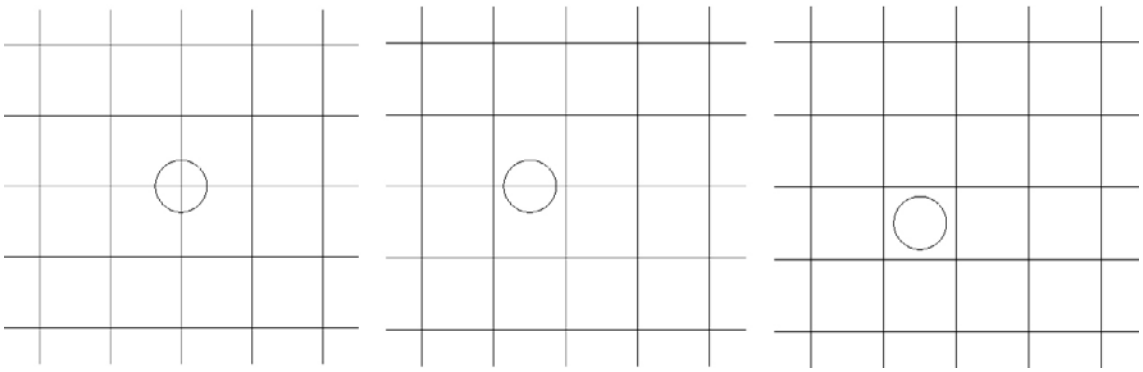

Figure B-4. *Illustration showing three tunnel positions, A–C, with regard to the cell size of a coarse computational grid.*

B5 Grouting

The analytical equation shown in Equation (B-2) does not account for the effect of grouting. If the thickness, t, of the grouted zone around an open tunnel and the hydraulic conductivity of the grouted bedrock, K_t (cf. Equation (B-1), are known, the inflow rate to the tunnel may be written as /Gustafson et al. 2004/:

$$q = 2\pi K d\left[\ln\left(\frac{2d}{r}\right) + (K/K_t - 1)\ln(1 + t/r)\right]^{-1} \quad \text{(B-3)}$$

The application of the tunnel routine to the studied repository layout at Forsmark uses a cell size of the computational grid of 4 m close to the deposition tunnels. This resolution compares well with the dimensions of the deposition tunnels, which have a height 4.8 m and a width 4.2 m. Hence, the equivalent diameter of the tunnel is c. 5 m, which is somewhat greater than the cell size of the computational grid. From Figure B-1, it is concluded that the "penetration depth" associated with Equation (B-1) for a uniform computational grid is approximately of the same size as the cell size, i.e. in this case c. 4 m.

Table B-4 shows the parameter values used in DarcyTools to evaluate the accuracy of the tunnel routine as applied in the work reported here. The calculated inflow rates are compared with the analytical solution shown in Equation (B-3). The background hydraulic conductivity of the bedrock was set to 10^{-7} m/s and three different levels of the grouting efficiency were tested: 10^{-9} m/s, 10^{-8} m/s and 10^{-7} m/s. The thickness of the grouted zone was set to 4 m. The calculations were made for the three tunnel positions shown in Figure B-3. The results are summarised in Table B-5.

Table B-4. Parameters values for simulations of inflow to an open tunnel in a grouted bedrock.

Domain size	4,000 m (horizontal), 2,000 m (vertical)
Grid (cell) size	(Δx, Δz) = 4 m
Hydraulic conductivity	K = 10^{-7} m/s K_t = 10^{-9} m/s, 10^{-8} m/s, 10^{-7} m/s
Boundary conditions	Bottom: no flow Vertical: no flow Top: atmospheric pressure Tunnel: atmospheric pressure
Tunnel data	Depth: 500 m Radius: 1 m t = 4 m

Table B-5. Comparison between numerical and analytical solutions of the inflow rate, q, for the parameter values specified in Table B-4. Inflow rates (q = N·10^{-5} m^3/s/m) are shown for three tunnel positions, A–C, and three levels of grouting efficiency (K_t).

	K_t (m/s)		
Tunnel position	**10^{-9}**	**10^{-8}**	**10^{-7}**
A	0.38	2.41	5.28
B	0.29	1.98	4.87
C	0.19	1.48	4.36
Numerical q (Average)	0.29	1.96	4.84
Analytical q with r = 1 m	0.19	1.47	4.55
(Numerical q)/(Analytical q with r = 1 m)	1.52	1.33	1.06

B6 Summary and conclusions

The comparison with the analytical solutions in Equation (B-2) and Equation (B-3) are shown in Table B-3 and Table B-5, respectively.

The results of the flow simulations using the tunnel routine for a non grouted bedrock are summarised in Table B-3. It is found that the tunnel routine give inflow rates that are close to rates of the analytical solution shown in Equation (B-2).

For a grouting efficiency of $K_t = 10^{-7}$ m/s, the values shown in Table B-5 represent the effect of the position of the tunnel in the grid only as no modification of the hydraulic conductivity of the bedrock near the tunnel was applied, i.e. for this case Equation (B-3) becomes identical to Equation (B-2). The average deviation from the analytical solution for $K_t = 10^{-7}$ m/s is c. 6%, thus suggesting that the tunnel routine works quite well also when the cell size is comparable to the tunnel diameter.

When the level of the grouting efficiency increases, i.e. when the value of K_t decreases, the calculated inflow rates decreases significantly. For $K_t = 10^{-8}$ m/s, the average deviation from the analytical solution was found to be c. 33%, and for $K_t = 10^{-9}$ m/s, the average deviation from the analytical solution was found to be c. 52%.

The values shown in Table B-5 assume that the cell size of the computational grid is of the same order as the tunnel diameter. The sensitivity of the results to the cell size was looked at by using a systematic grid refinement of the resolution of the computational grid near the tunnel from 4 m to 0.25 m. This change rendered an average deviation from the analytical solution for the higher resolution of c. 10% for $K_t = 10^{-9}$ m/s.

Appendix C

Saturation of backfill

C1 Background

When the deposition tunnels are backfilled, large parts of the pore space in the backfill are filled with air. The unsaturated pore space will eventually be filled with water, but the time scale for this hydration process is not known in detail. /Börgesson et al. 2006/ studied the problem using advanced two-phase models. Such models provide solutions based on fundamental physical laws and well tested empirical relations. /Börgesson et al. 2006/ concluded that both the properties of the backfill and those of the surrounding rock affect the time scale of the hydration process.

C2 Objectives

A problem of using two-phase models is that it is presently hard to include an adequate description of the structural-hydraulic properties of a discrete fracture network. For this reason, a simplistic approach to the complex hydration process of the backfill has been suggested using DarcyTools /Svensson 2010/. The suggested approach has the advantage of being applicable to the geometry of the final repository modelled in SR-Site, which is embedded in sparsely fractured bedrock with water carrying fractures. The objective of this appendix is to describe the essence of the simplistic approach suggested by /Svensson 2010/ and to provide a demonstration of its application to a final repository at Laxemar.

C3 Brief description of the saturation process

Unsaturated flow conditions occur during the different stages of a final repository for spent nuclear fuel (construction, operation and post-closure). Different processes and properties such as capillary suction and relative permeability act upon the hydraulic behaviour of the system and may affect the duration of the saturation of the initially unsaturated parts. Figure C-1 shows an illustration of some of the processes involved. The illustration does not claim to be complete, but it is clear that we are dealing with three phases (solid, air and water) with an air phase that is subject to compression and dissolution in the water phase.

- The groundwater flow in the discrete fracture network in the bedrock provides the groundwater up to the tunnel face.
- The saturation front is defined by the zero pressure line, i.e. where the gauge pressure equals the atmospheric pressure. Towards the tunnel, the gauge pressure decreases and towards the bedrock it increases.
- In the unsaturated part, groundwater is transported by capillary suction and may also be transported as vapor diffusion.
- The air initially present in the backfill may disappear by several processes: dissolution in the water, gravitational rise and by diffusion and advection when dissolved in the water. A significant compression of the air can also be expected when the pore pressure rises.
- Temperature and salinity gradients may affect most processes.

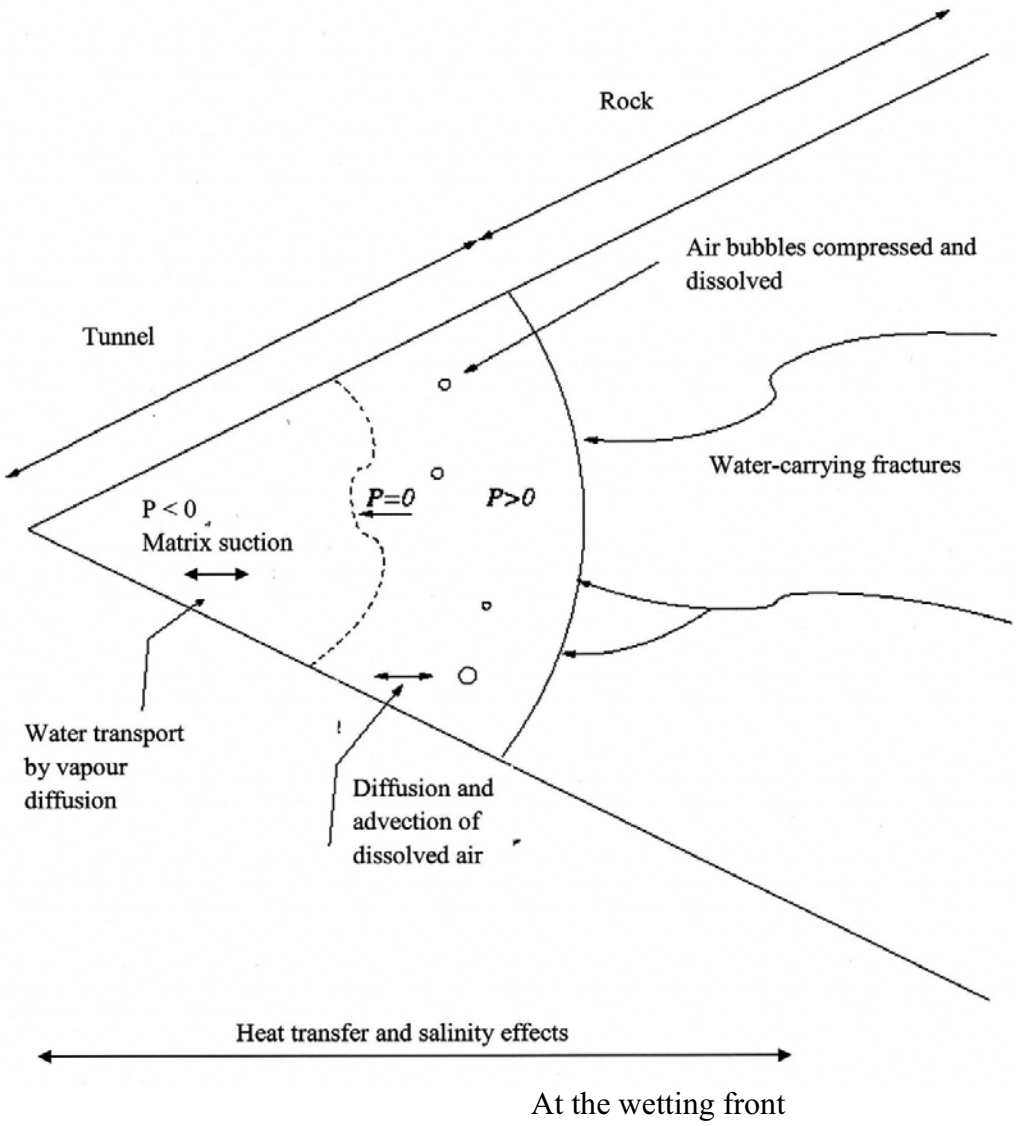

Figure C-1. *Schematic illustration of relevant physical processes during the saturation of the unsaturated tunnel backfill. In the figure, P denotes gauge pressure.*

C4 Attempted simplification

If all, or most, of the processes discussed above are considered in a numerical model, the solution has to be based on fundamental physical laws and well tested empirical relations, see /Börgesson et al. 2006/. The simplistic approach suggested by /Svensson 2010/ was used in the work reported here. The approach is based on two main assumptions.

- It is assumed that the hydration process of the unsaturated parts of the backfill can be modelled as single-phase, saturated groundwater flow system, where the inflow of groundwater to the repository is mainly governed by the pressure gradients and the resistance in the rock, the saturated part of backfill and the position of the wetting front.
- The specific storativity, S_s, is given an untraditional role, as it is used to simulate the removal of the volume occupied by air in the backfill. That is, it is regarded as the ratio of the change of the initially air filled porosity in the backfill , $\Delta[\phi(1–S_w)]$, and the associated head change, $\Delta P/\rho g$:

$$S_s = \frac{\Delta[\phi(1-S_w)]\,\rho g}{\Delta P} \qquad \text{(C-1)}$$

where
ϕ = porosity of the backfill [–]
S_w = saturation [–]
ρ = fluid density [kg/m^3]
g = acceleration of gravity [m/s^2]
P = dynamic pressure [Pa]

With reference to Figure C-1 it is obvious that the problem is drastically simplified, but Equation (C-1) seems reasonable from a physical point of view since air bubbles may be present in the backfill after saturation. These bubbles will be compressed due to the pressure rise and cause a storage effect.

Following /Börgesson et al. 2006/, the hydraulic conductivity of the unsaturated backfill was related to the degree of saturation and the saturation was related to the retention curve. Following /Svensson 2010/, the specific storage of the unsaturated backfill was assumed to have a constant value and the specific storage of the saturated backfill another constant value. Moreover, the backfill was considered saturated as soon as the pressure turned positive. At that instant, the value of the specific storage was switched from an unsaturated value to a saturated. It is noted that with this definition of the specific storage, non-linear capillary suction effects of the unsaturated material were not taken into account.

C5 Application to a final repository at Laxemar

For the sake of the work reported here, the attempted simplification was applied to a final repository at Laxemar. For the simulations, a number of assumptions were made.

- The layout of the repository was simplified (no central area, ramps, deposition holes, or ventilation shafts), see Figure C-2.
- The simulation of the saturation process was adapted to the four stages of operation, A–D, see Figure C-2. For each stage, the computational grid was set up to form a box around the corresponding part of the repository. That is, it was assumed that the saturation of the four stages does not interfere.
- A constant fluid density was assumed (freshwater) and hydrostatic pressure was fixed at all boundaries. The domain boundaries were at least 100 m away from the repository.
- The cell size inside the tunnels was set to 1 m. In total, the computational grid consisted of about 2.5 million cells.
- The volume inside the tunnels varied somewhat between the four stages, but was on the average c. 3·105 m^3.
- The properties of the backfilling material was assumed to be similar to those of Friedland Clay /Börgesson et al. 2006/.

Based on the above assumptions, the unsaturated pore volume in the backfill at the start of the saturation process was estimated to 4–4.1 m^3/m of tunnel.

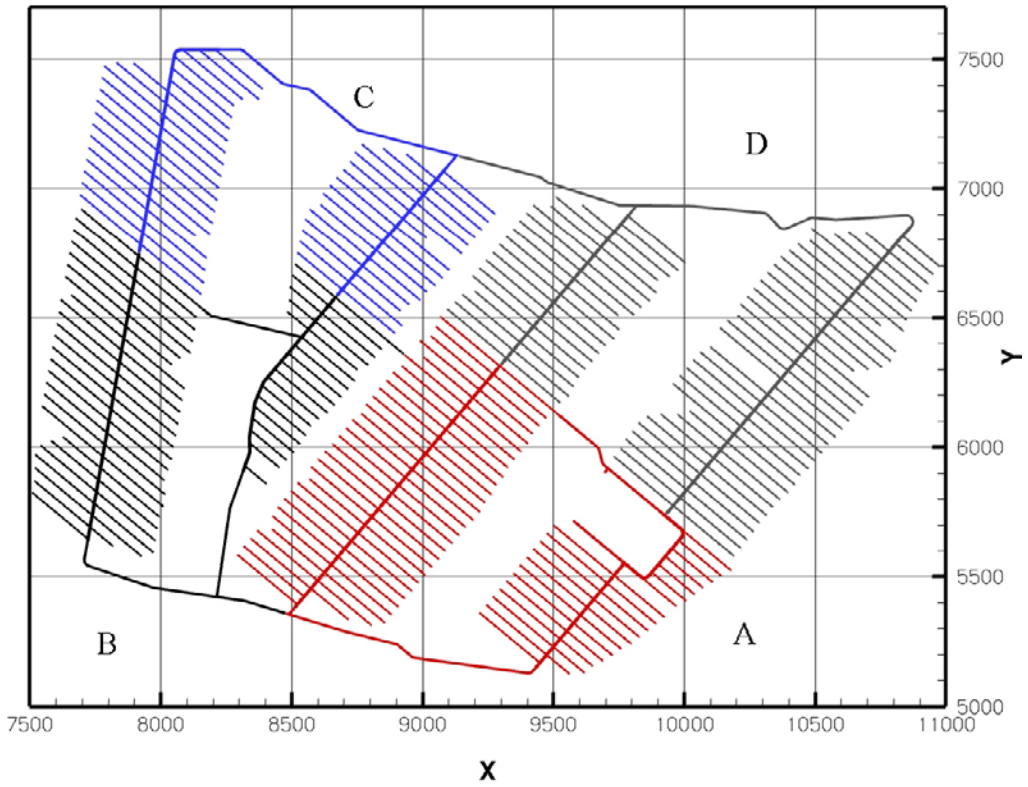

Figure C-2. *A simplified layout was used (no central area, no deposition holes, ramp or ventilation shafts). The simulation of the saturation process was adapted to the four stages of operation, A–D. For each stage, the computational grid was set up to form a box around the corresponding part of the repository. The y-axis points towards north.*

C6 Results

The simulated pressure build-up following the closure of the deposition tunnels for the four stages, A–D, is shown in Figure C-3, Figure C-4, Figure C-5 and Figure C-6. The plots shown in these figures display the pressure after 100 days.

For stage D the simulation time was extended to about 20 years. It is seen (Figure C-7 and Figure C-8) that full saturation is achieved after this time.

The impression from Figure C-3, Figure C-4, Figure C-5 and Figure C-6 is that the backfill is saturated fairly quickly where a fracture crosses the tunnel, while other parts are still unaffected.

The simulation time for stage E was extended to about 20 years and a more detailed analysis was carried out. The inflow and accumulated inflow is shown in Figure C-6. It is found that the total inflow rate is around 0.01 L/s for a long period and the tunnel is not fully saturated after 20 years. Figure C-7 shows the fraction of the tunnel volume that was saturated as a function of time.

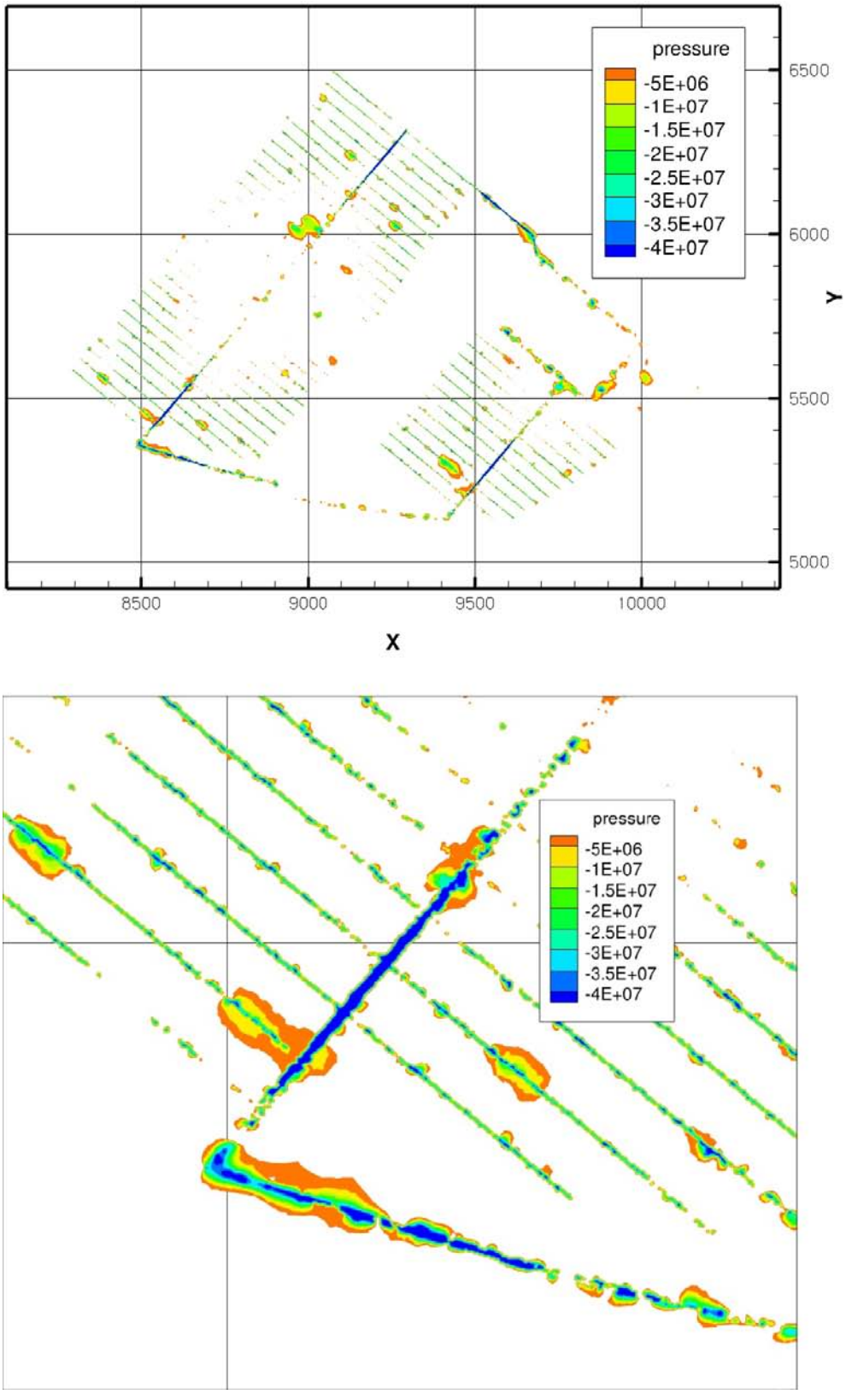

Figure C-3. *Gauge pressure distribution (in Pa) 100 days after closure of stage A. Bottom figure shows a magnified view.*

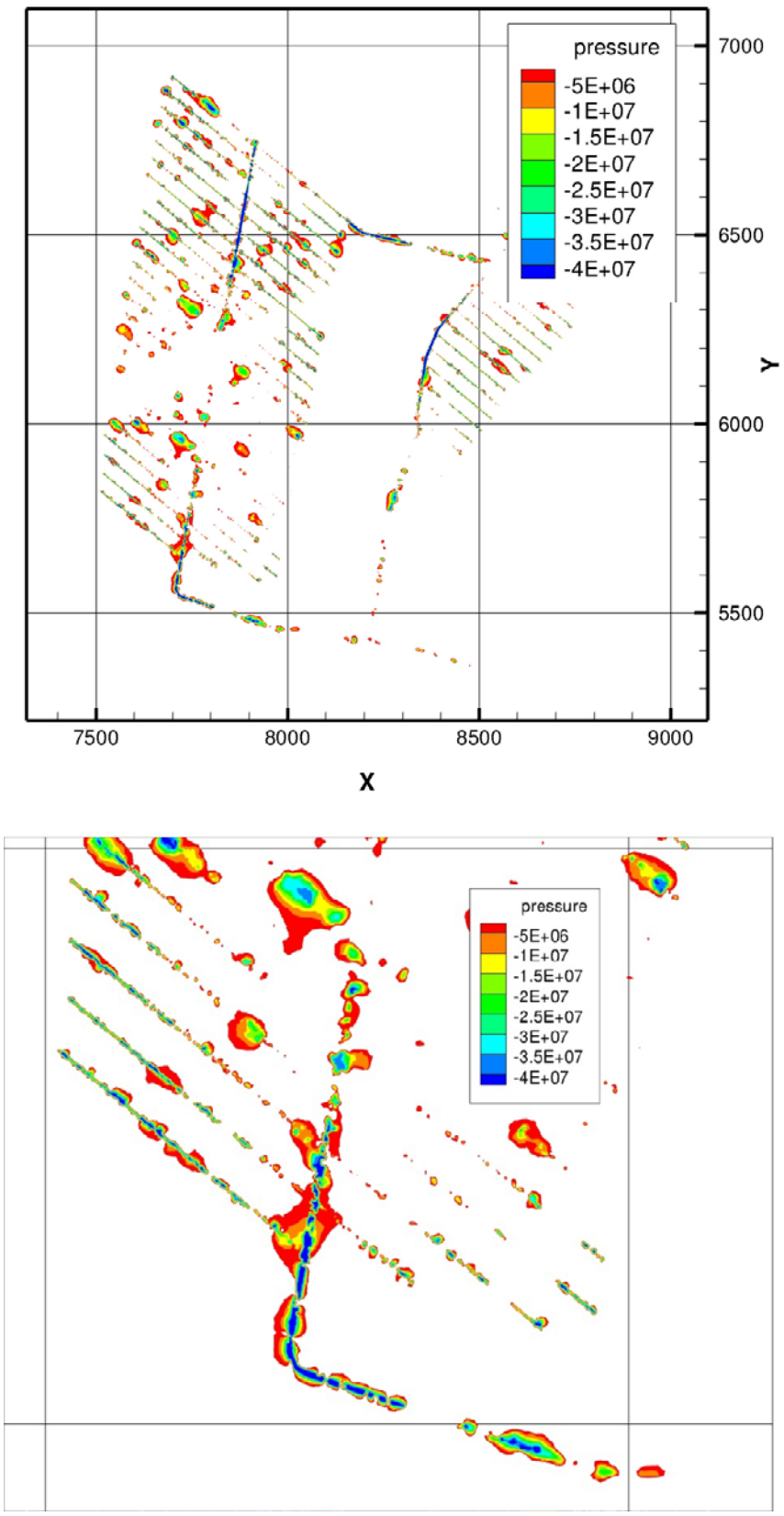

Figure C-4. *Gauge pressure distribution (in Pa) 100 days after closure of stage B. Bottom figure shows a magnified view.*

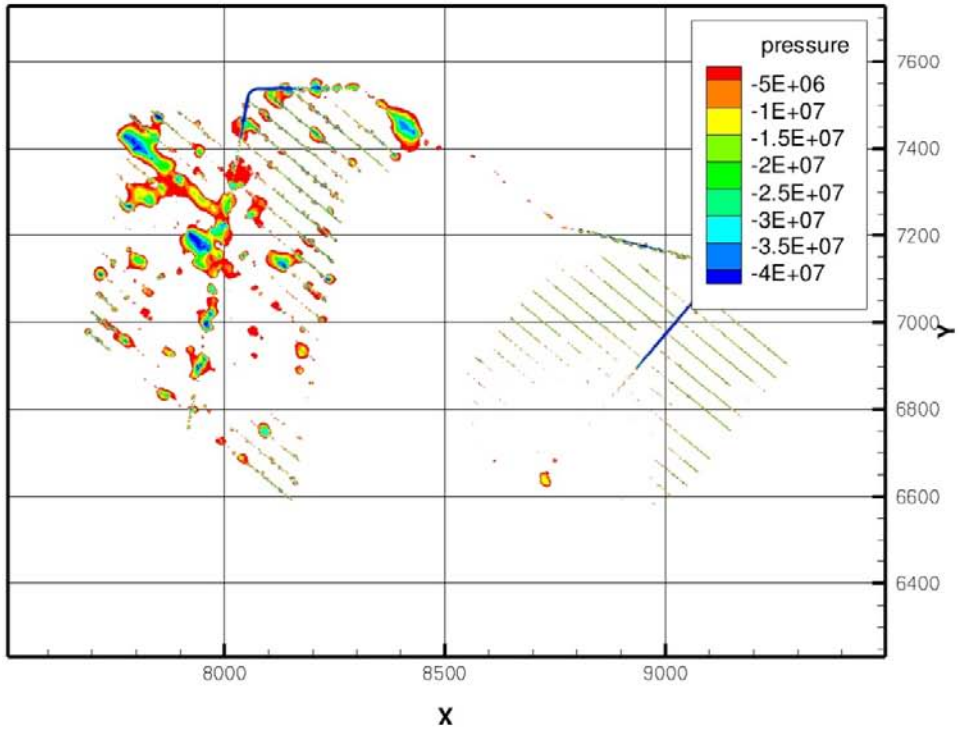

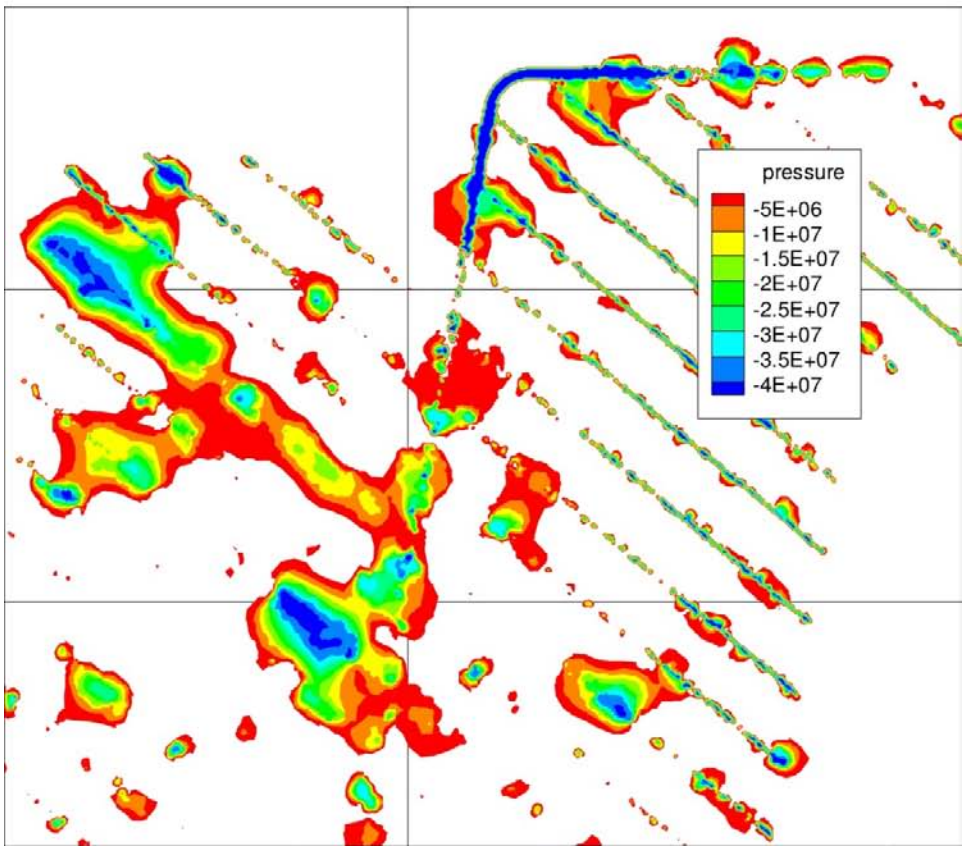

Figure C-5. *Gauge pressure distribution (in Pa) 100 days after closure of stage C. Bottom figure shows a magnified view.*

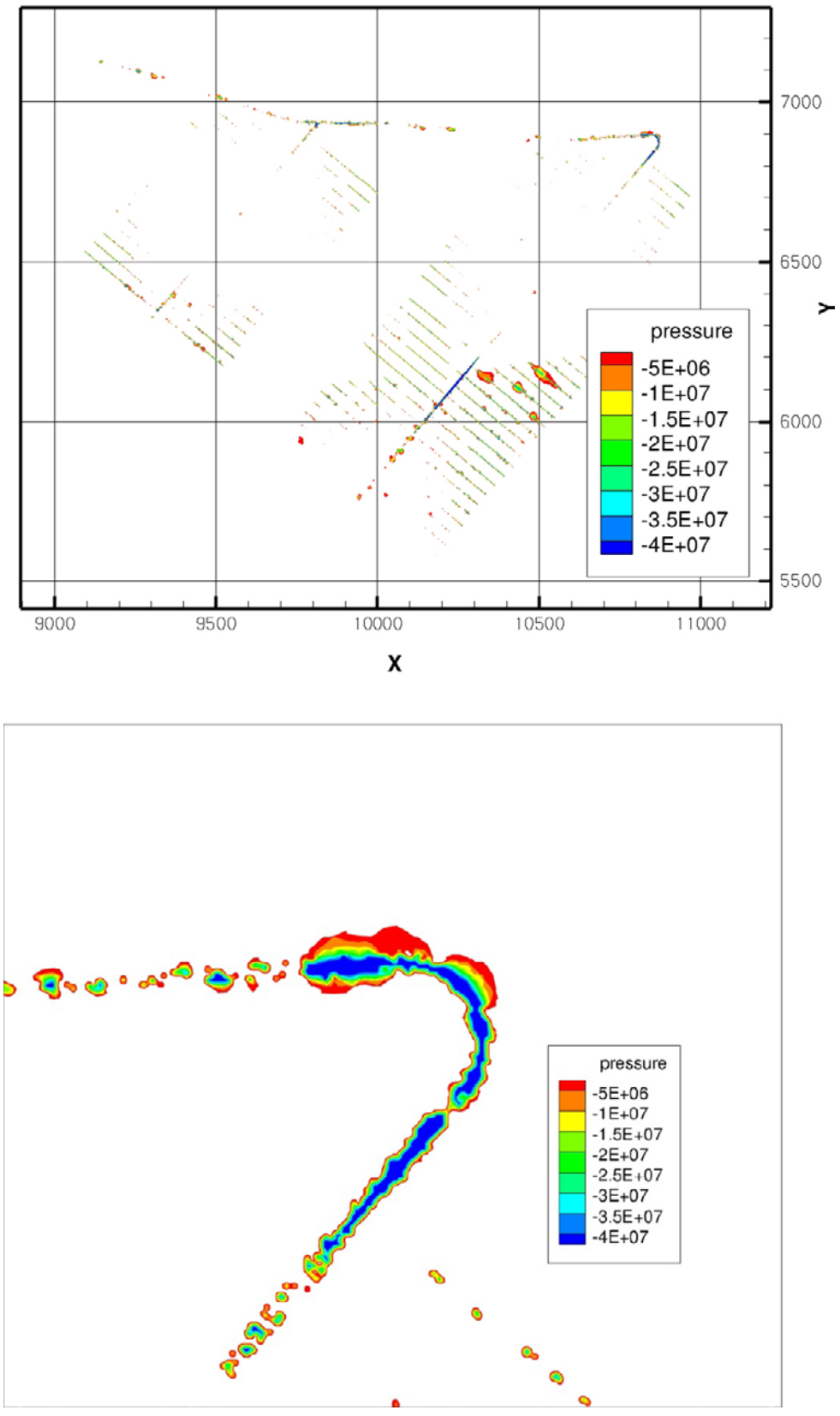

Figure C-6. *Gauge pressure distribution (in Pa) 100 days after closure of stage D. Bottom figure shows a magnified view.*

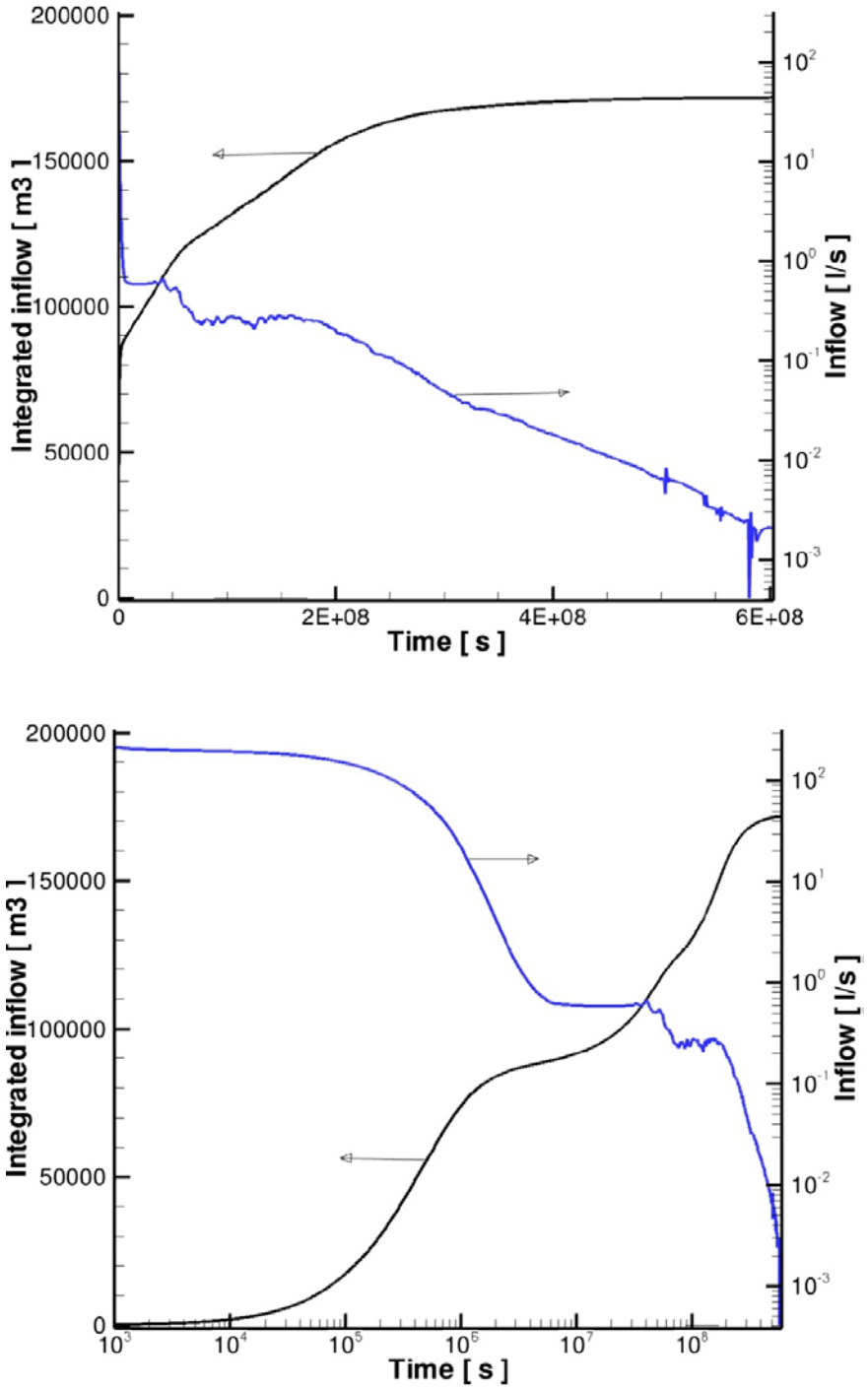

Figure C-7. *Inflow rate [L/s] and cumulate inflow [m^3] for stage E with a linear (top) and logarithmic time scale. One year is about $31.5 \cdot 10^6$ s.*

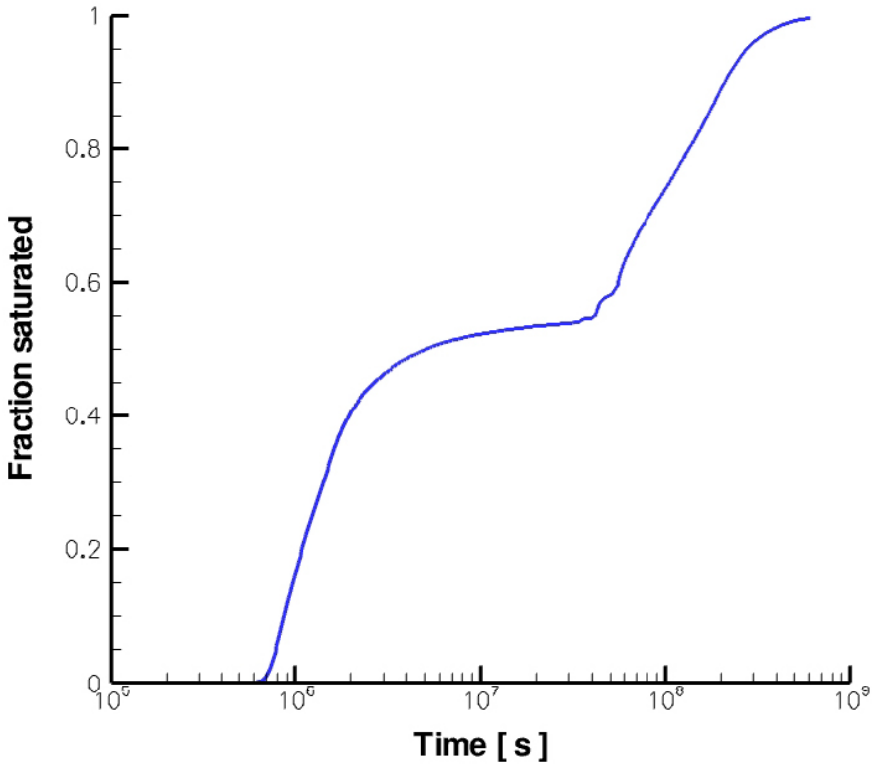

Figure C-8. *The fraction of the tunnel volume that was saturated as a function of time.*

C7 Discussion and conclusions

A few observations can be made from the simulations carried out in this appendix.

- The approximate method for modelling the hydration process of an unsaturated backfill in a fractured medium suggested by /Svensson 2010/ works well computationally.
- The simulations reported here indicate that the backfill is saturated fairly quickly at those locations where a fracture crosses the tunnel (radial saturation). Where there are no fracture intersections, the saturation process progresses along the tunnel (axial saturation). No account was made for a crown space, excavated damage zone or other hydraulic imperfections. If such features are included, the saturation process most likely progresses more rapidly.
- The total time scale for the hydration process is probably 10–30 years. It is presently not possible to be more specific about the time scale.

It should be noted that the simplifications invoked by the approximate method call for further systematic studies before any firm conclusions about the hydration time can be drawn. For example, it is presently not clear how various processes and parameter values may influence the results. Capillary suction is one example of a physical process that is simplistically treated in the work reported here. Another example is the effect of the minimum value used for the hydraulic conductivity of the intact bedrock. In most groundwater flow simulations that use a continuum model, the minimum hydraulic conductivity of the intact (non-fractured) bedrock is set to c. 10^{-10} m/s. For the present simulation, however, it was found that this value has to be reduced to 10^{-13} m/s, otherwise it controls the saturation time.

Appendix D

Scoping calculations of the total inflow rate and drawdown

Preliminary simulations indicate that the inflow rates to the open repository at Laxemar may be several hundreds of L/s. Such inflows will create both engineering and environmental problems and it is for this reason important to establish if the simulation results are realistic.

D1 What inflow rates can be expected?

The basic techniques for calculation of inflows to a repository have been validated by comparisons with analytical solutions. Some of this work is found in Appendix B.

Here only one such comparison with an analytical solution will be discussed, see Figures D-1 and D-2. The analytical solution is applied to the main and transport tunnels, assuming homogeneous rock conductivity and various grouting levels; for details see Appendix B. The same case was also simulated with DarcyTools, but now with the present fracture network. From the figure the following is noted:

- Inflows of 100 L/s or higher are generally obtained for a rock conductivity of 10^{-7} m/s or higher. Note that the grouting efficiency for tunnels is defined by maximum conductivities of 10^{-8} or 10^{-7} m/s, as a result of grouting, for grouting levels I→IV (Table 4-3).
- A grouting conductivity of 10^{-9} m/s reduces the inflow to about 50 L/s or smaller, irrespective of the rock conductivity.
- The DarcyTools results, given by the dots, agree quite well with the curve for a constant rock conductivity of $5.7 \cdot 10^{-8}$ m/s ($\log_{10} K_0 = -7.2$). From Figure 4-20 we find that the median conductivity at repository level is higher than this value.

The main conclusion from the Appendix B (and from /Svensson 2010/) is that the accuracy of the simulation model is acceptable. The reason for the high inflows is probably due to the high transmissivity of the fracture network. For grouting conductivities larger than 10^{-8} m/s and a realistic mean conductivity for the rock, the tunnels alone will give inflows of several hundreds L/s.

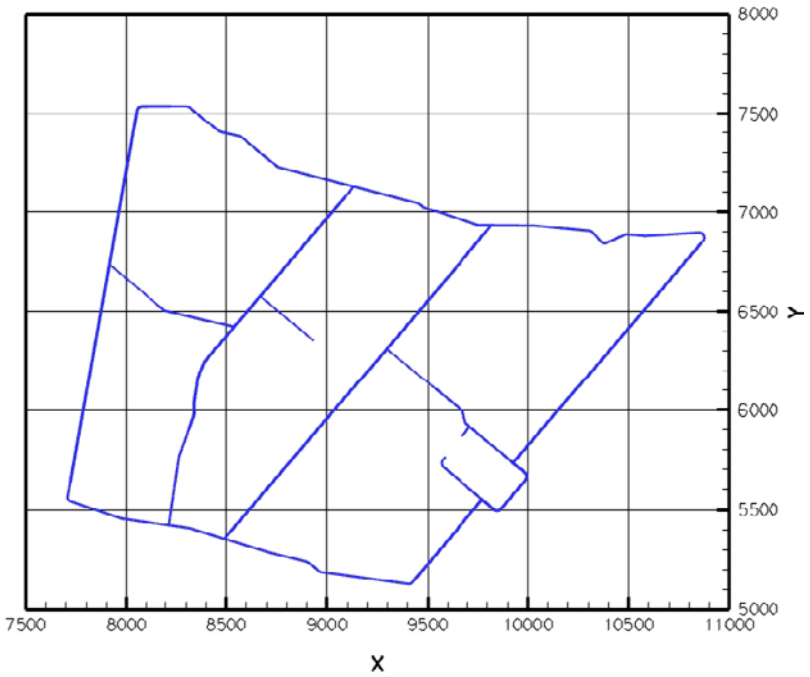

Figure D-1. *All main and transport tunnels. Total length about 16 km.*

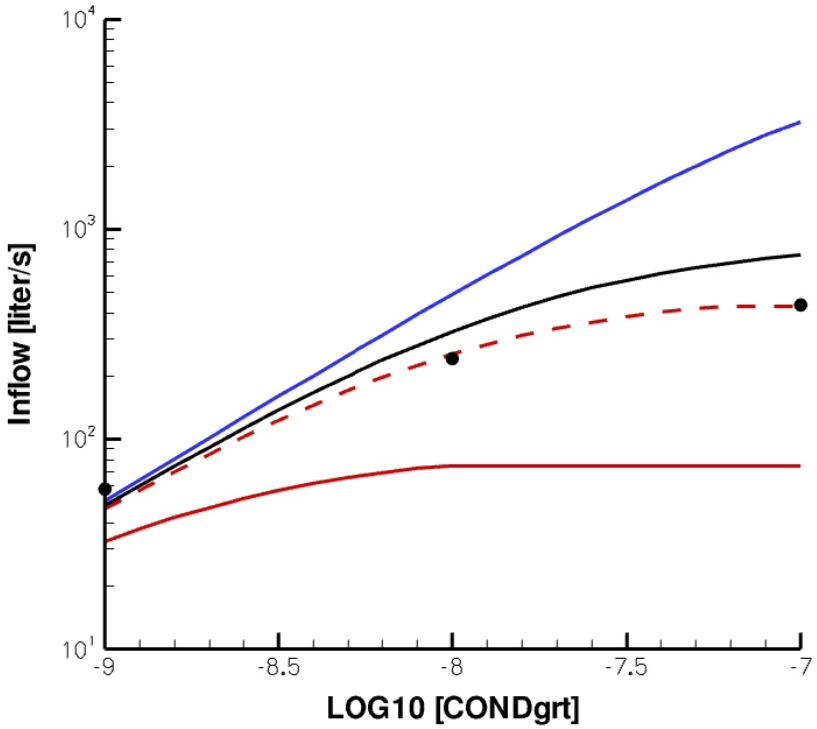

Figure D-2. *Solid lines represent the inflows given by the analytical solution for K_0 equal to10^{-8} (red), 10^{-7} (black) and 10^{-6} (blue). Dots give the DarcyTools results and the broken line represents the analytical solution for $K_0 = 5.7 \cdot 10^{-8}$ m/s. For further details, see Appendix B.*

D2 What drawdowns can be expected?

If the inflow will be "several hundred L/s" we need to understand the source of this water and what the resulting drawdown of the groundwater table will be. The simple answer regarding the source is "net precipitation and the Baltic Sea". We need however to be a bit more specific in particular if we should be able to understand the drawdown. Let us study the situation outlined in Figure D-3. The circle in the top figure has a diameter of about 4 km and as can be seen we have streams or the Baltic Sea almost all around the perimeter. Let us assume that the circle defines a line of constant pressure and that the drawdown is all inside the circle. Regarding the source of water it is useful to divide the source into:

- Net precipitation over the circle. With $P–E$ = 165 mm/year we can estimate this to about 65 L/s.
- Near surface fluxes from streams and the Baltic Sea.
- A quasi-horizontal ground water flux driven by the pressure gradient from the drawdown cone.

It is also of interest to note that the repository is located in the catchment area of Laxemarån. As this area is about 40 km^2 the net precipitation over the area amounts to about 200 L/s. This flux is hence the upper limit for "the easily accessible source".

Next we will estimate the magnitude of the deeper ground water flux. In Figure D-3 a control volume is indicated and it is the horizontal flux over the vertical boundaries we should estimate. If we assume that the pipe-shaped control volume has a diameter of 2 km and a depth of, say, 700 m we have:

$$Q = AK\frac{H}{2000}\cdot 10^3 \ \ [\mathrm{L/s}]$$

or

$$Q \approx 2.2\cdot 10^6 KH \ \ [\mathrm{L/s}]$$

where K is the average hydraulic conductivity and H the drawdown.

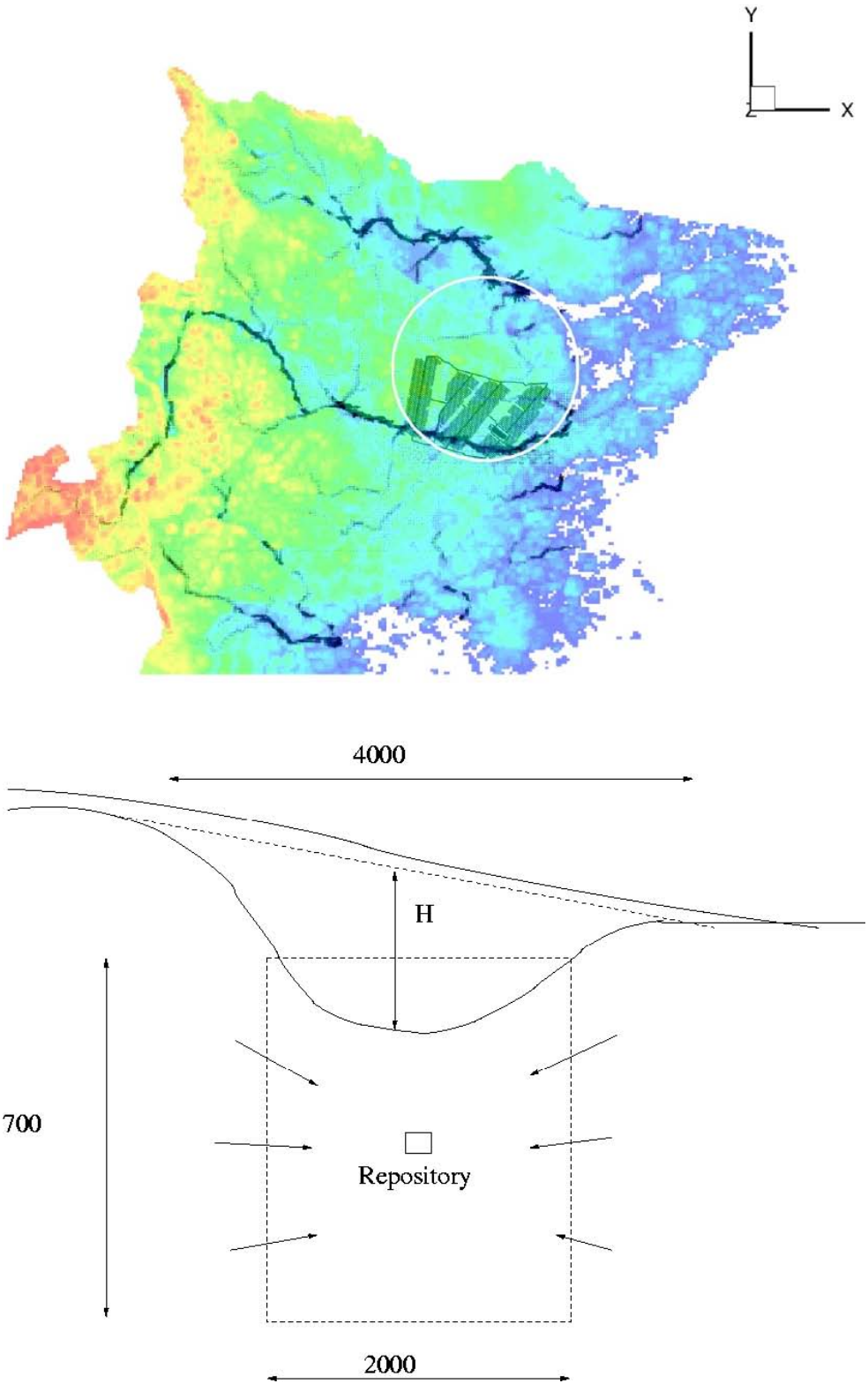

Figure D-3. *Schematic figures for the estimate of ground water flux towards the repository.*

This relation is illustrated in Figure D-4 for two different conductivities; one of which is the indicated mean conductivity used in Figure D-2. The main conclusion is anyway that the contribution from the deep ground water flux is small for drawdowns of less than 200 m.

The overall conclusion regarding the source is that the net precipitation over the draw down cone and the deep ground water flux may contribute with about 100 L/s. A larger inflow needs to be supported by surface processes, for example an inflow from Laxemarån. One can however not assume that this stream is directly "available" as a source; streams can flow over an unsaturated ground with only minor infiltration.

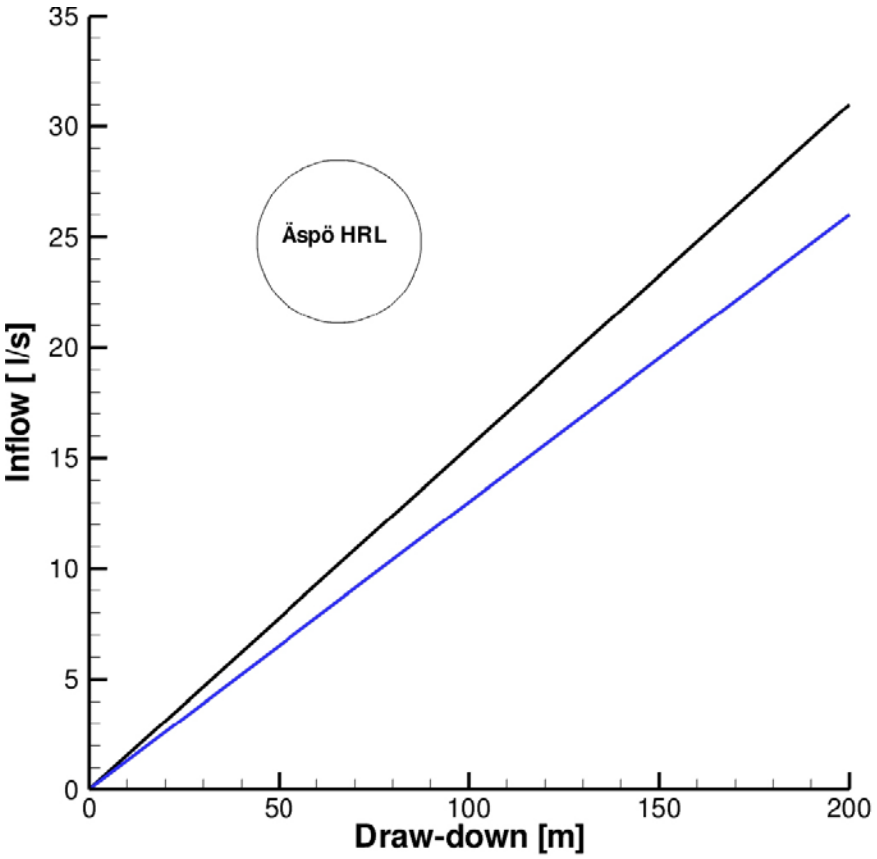

Figure D-4. *Groundwater flux versus drawdown for a mean conductivity of* 10^{-7} *m/s (black) and* $5.8 \cdot 10^{-8}$ *m/s (blue). Conditions for the Äspö HRL included as a reference.*

Appendix E

Hydrogeological base case model

E1 Introduction

As described in Section 1.5, the results from numerical model simulations using the Hydrogeological base case have raised the question whether the stochastic part of the network is too transmissive. The models are compared in this appendix.

It should be noted that it is only the hydrogeological DFN part of the two models that is different in the comparisons presented below. The deterministic fractures and zones, the repository layout, the computational grid, etc will be the same for the two cases.

E2 Objective

The main objective of this appendix is to demonstrate how different versions of the hydrogeological DFN model may influence the simulation results, in particular the inflow to an open repository. The comparison between the two DFN models are carried out by simply showing simulation results for corresponding conditions (like undisturbed conditions, operation stage E grouting level V, etc). The simulated inflow rates are given in detail, i.e. all grouting levels and operation stages, while other aspects are only described superficially, i.e. drawdowns and salt water changes.

E3 Results

As described in /Joyce et al. 2010/, it is the difference in the connected open fracture frequency that has been the main discussion point. The difference in this important quantity results from a different fracture size distribution, which in turn creates changes in the fracture transmissivity model.

The comparison start with a comparison of the vertical permeability at repository depth, see Figure E-1. It is clear that the Elaborated Hydro-DFN model is less permeable.

Next, we look on the inflow to different parts of the repository, see Table E-1 and Table E-2. It is logical that the lower permeability of the Elaborated Hydro-DFN model also results in lower inflows. From Table E-3, which more directly compares the inflows, it is noted that the Elaborated Hydro-DFN model has about 56% of the total inflow rate of the Hydrogeological base case model.

The simulated drawdowns of the groundwater table are compared in Figure E-2. The Hydrogeological base case model generates a large area with a drawdown greater than 10 m. Such drawdown values are absent in the Elaborated Hydro-DFN.

Finally the salinity field at repository depth at undisturbed conditions are shown in Figure E-3. It is found that very similar fields are generated by the two DFN models.

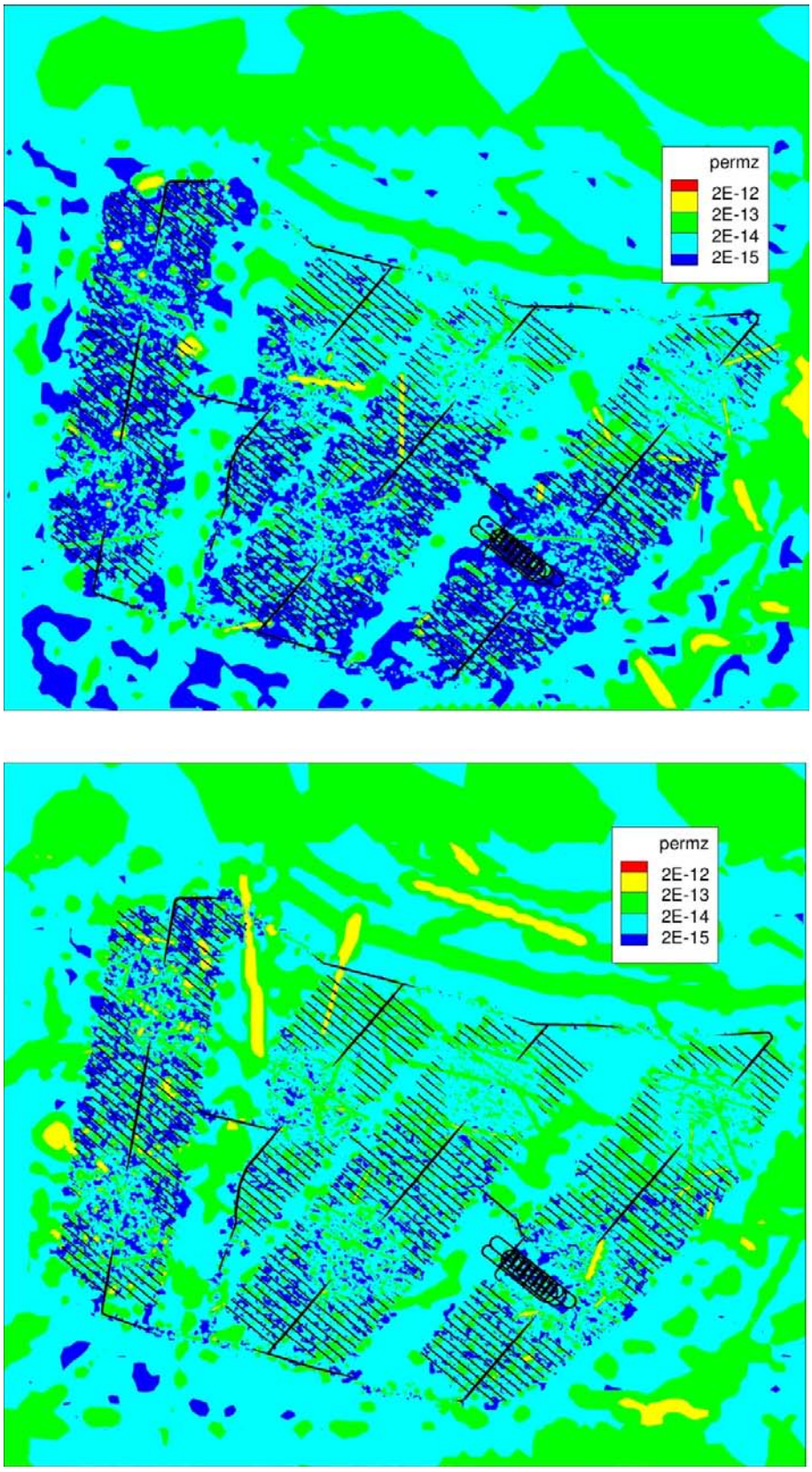

Figure E-1. *Vertical permeability field at repository depth for the Elaborated Hydro-DFN model (top) and the Hydrogeological base case (bottom).*

Table E-1. The Elaborated Hydro-DFN model. Inflow, in L/s, to different parts of the repository, for five stages and six grouting alternatives. The different parts of the repository are shown in Figure 1-2, the grouting efficiency are defined in Table 4-3 and the five stages are defined in Figure 1-2.

Part	Grouting Level																												
	I					II					III					IV					V					VI				
	A	B	C	D	E	A	B	C	D	E	A	B	C	D	E	A	B	C	D	E	A	B	C	D	E	A	B	C	D	E
CA	32	29	34	34	32	17	16	17	17	16	6	5	6	6	5	2	2	2	2	2	6	6	6	7	6	2	2	2	2	2
ST1	32	18	29	29	26	21	12	20	20	18	22	16	21	21	19	22	19	21	21	20	8	5	8	8	8	8	7	8	8	8
VS1	3	3	3	3	3	1	1	1	1	1	1	1	1	1	1	1	1	1	1	1	0	0	0	0	0	0	0	0	0	0
DT1	8					3					1					0					1					0				
DH1	2					1					0					0					0					0				
DT2		54					42					20					6					22					6			
DH2		17					13					8					3					8					3			
ST3			32	41	45			21	28	30			25	29	30			28	30	30			7	10	10			9	10	10
VS2			2	2	3			1	1	1			1	1	1			1	1	1			0	0	0			0	0	0
DT3			48					372					17					4					19					5		
DH3			13					11					6					2					7					2		
ST4				27	45				18	28				23	27				26	27				6	8				7	8
DT4				22					18					8					2					9					2	
DH4				75					55					21					4					24					5	
ST5					52					36					49					56					12					15
DT5					200					144					51					9					58					10
DH5					46					35					15					4					17					4
∑	77	121	161	233	452	43	84	108	158	309	30	50	77	110	198	25	31	59	87	150	15	41	47	64	119	10	18	26	34	57

Table E-2. The Hydrogeological base case model. Inflow, in L/s, to different parts of the repository, for five stages and six grouting alternatives. The different parts of the repository are shown in Figure 1-2, the grouting efficiency are defined in Table 4-3 and the five stages are defined in Figure 1-2.

Part	Grouting Level																												
	I					II					III					IV					V					VI				
	A	B	C	D	E	A	B	C	D	E	A	B	C	D	E	A	B	C	D	E	A	B	C	D	E	A	B	C	D	E
CA	38	36	72	72	68	30	26	35	35	32	10	9	10	10	8	2	2	2	2	2	12	10	12	12	11	3	3	3	3	3
ST1	87	49	87	87	75	55	31	54	54	48	58	45	55	56	51	59	54	57	57	54	16	11	15	15	14	16	14	16	16	15
VS1	3	3	3	3	3	1	1	1	1	1	1	1	1	1	1	1	1	1	1	1	0	0	0	0	0	0	0	0	0	0
DT1	9					4					1					0					1					0				
DH1	2					1					0					0					0					0				
DT2		110					88					36					7					41					8			
DH2		36					32					15					4					17					4			
ST3			50	72	78			31	44	47			39	46	45			44	47	46			10	13	13			12	13	13
VS2			6	6	6			2	2	2			2	2	1			2	2	2			0	0	0			0	0	0
DT3			77					62					24					5					28					6		
DH3			26					21					9					2					10					3		
ST4				53	101				31	51				41	47				47	48				9	10				10	11
DT4				61					44					13					3					16					3	
DH4				171					114					33					6					39					7	
ST5					78					50					69					81					15					18
DT5					245					189					61					9					73					11
DH5					64					58					22					4					26					5
∑	139	234	321	525	718	91	178	206	325	478	70	106	140	202	305	62	68	113	165	247	29	79	75	104	152	19	29	40	52	76

Table E-3. Comparison between the inflows, in L/s, to the Elaborated Hydro-DFN model and the Hydrogeological base case model.

Grouting efficiency	Operation stage	Elaborated Hydro-DFN	Base case Hydro-DFN	Ratio·100 (%)
I	A	77	139	55
	B	121	234	52
	C	161	321	50
	D	233	525	44
	E	452	718	63
II	A	43	91	47
	B	84	178	47
	C	108	206	52
	D	158	325	49
	E	309	478	65
III	A	30	70	43
	B	50	106	47
	C	77	140	55
	D	110	202	54
	E	198	305	65
IV	A	25	62	40
	B	31	68	46
	C	59	113	52
	D	87	165	53
	E	150	247	61
V	A	15	29	52
	B	41	79	52
	C	47	75	63
	D	64	104	62
	E	119	152	78
VI	A	10	19	53
	B	18	29	62
	C	26	40	65
	D	34	52	65
	E	57	76	75
				Mean 56%

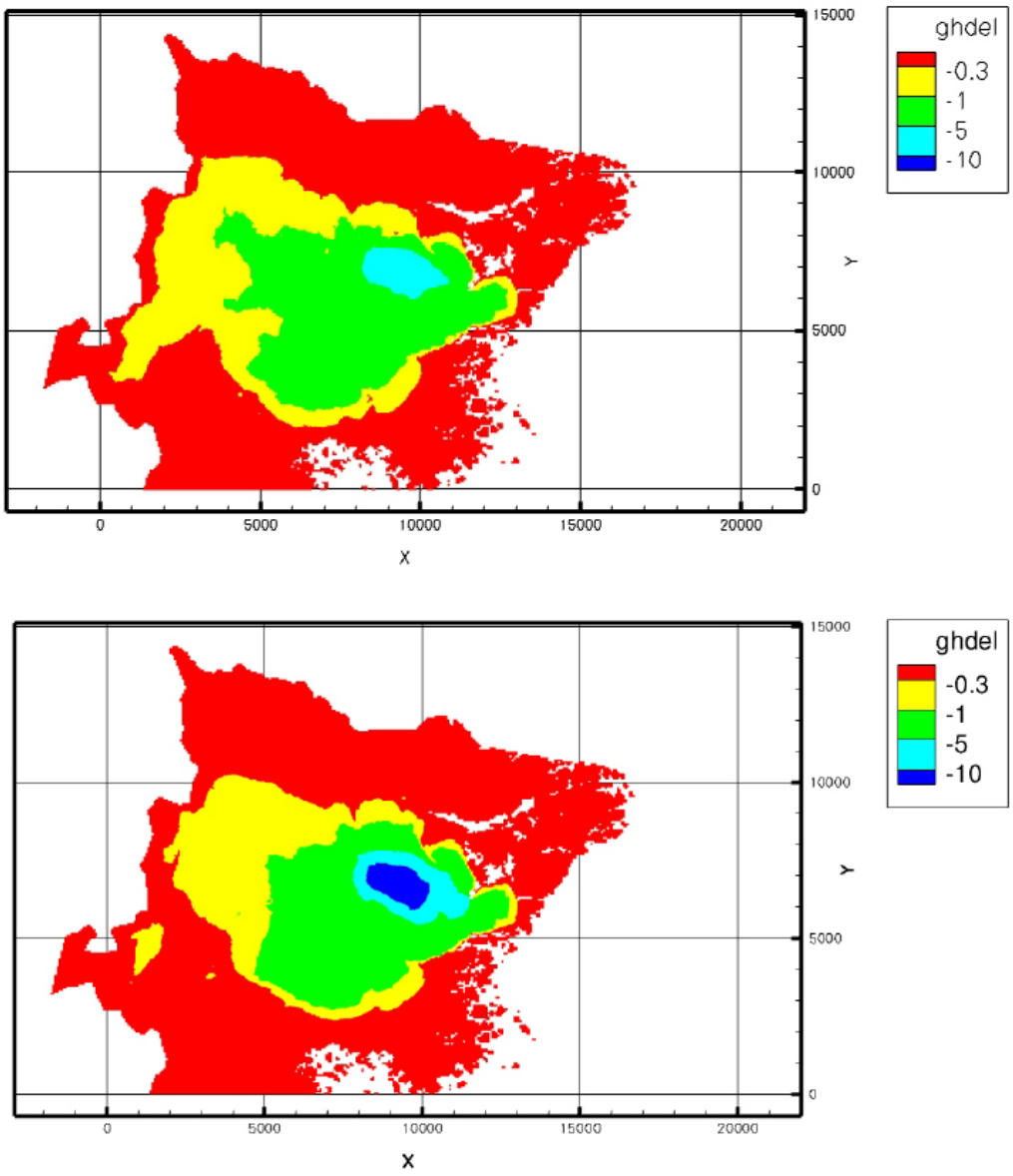

Figure E-2. *Simulated drawdown of the groundwater table at the end of operation stage E for grouting efficiency VI. Elaborated Hydro-DFN model (top) and Hydrogeological base case model (bottom).*

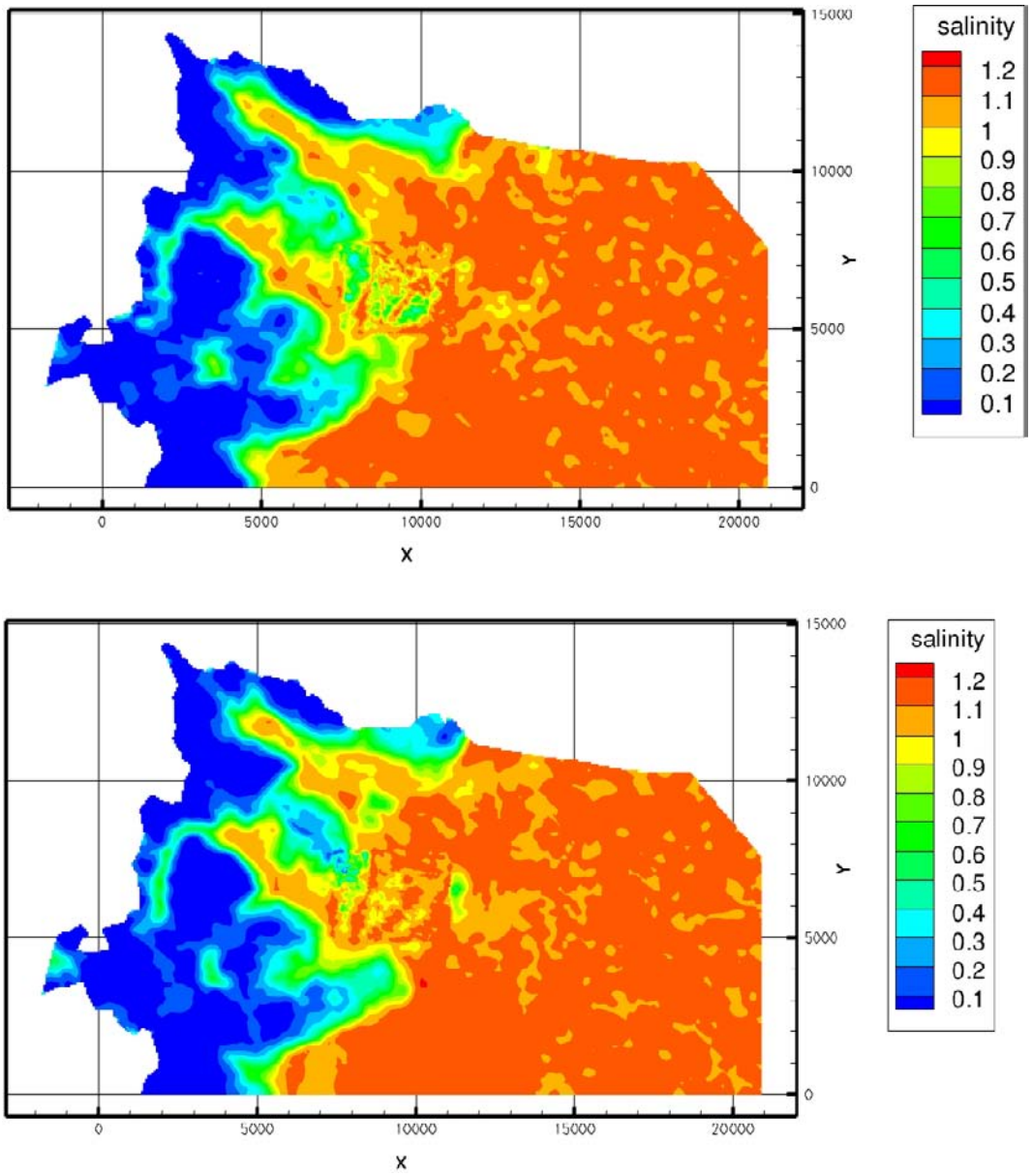

Figure E-3. *Simulated salinities 2000 AD in per cent by weight at –505 m elevation. A salinity of 0.1% by weight corresponds to approximately 1 g/L of TDS. Elaborated Hydro-DFN model (top) and Hydrogeological base case model (bottom).*

Appendix F

Compilation of input files

Name of file in DarcyTools	Date	Name of file at delivery
HCD		
HCDr1.dat	2010-03-03	100222_ls_2.3_Reg_Loc_Disks_Do1_100_Cond_25_dt.zip
HRD		
ls_r1_hrd_fractures_ascii.asc	2010-03-03	100222_ls_r1_hrd_fractures_ascii.zip
ls_altdfn_r1_hrd_fractures_ascii.asc	2010-08-27	100826_ls_altdfn_r1_hrd_fractures_ascii.zip
DEM		
top.dat	2009-04-02	adeadm_umeu_sm_hoj_4530.zip
DTStreams_05km2_from_umeu_sm_hoj_4530.dat	2009-05-06	DTStreams_05km2_from_umeu_sm_hoj_4530.zip
REPOSITORY LAYOUT		
17stl files for layout geometry	2009-03-19	LX_191BD*.stl
4 stl files for backfill saturation	2009-05-11	LX_191BD_00_853*.stl
OTHER GEOMETRIES		
WD.dat (Water Divide)	2009-03-18	Outer_boundary_trim5.stl
REJECTION CRITERIA		
KoordinatesFPCandEFPC.dat	2011-01-18	ls.altdfn.nocalib_Q1_2000_pline_merged.ptb

A list of all input files above, including storage location, is for traceability documented in the SKB data base SKBdoc under id nr 1271536.